

Dynamics of Continuous Attractor Neural Networks with Dynamical Synapses

by

FUNG, Chi Chung

A Thesis Submitted to
The Hong Kong University of Science and Technology
in Partial Fulfillment of the Requirements for
the Degree of Doctor of Philosophy
in Physics

August 2013, Hong Kong

Authorization

I hereby declare that I am the sole author of the thesis.

I authorize the Hong Kong University of Science and Technology to lend this thesis to other institutions or individuals for the purpose of scholarly research.

I further authorize the Hong Kong University of Science and Technology to reproduce the thesis by photocopying or by other means, in total or in part, at the request of other institutions or individuals for the purpose of scholarly research.

FUNG, Chi Chung

23 August 2013

Dynamics of Continuous Attractor Neural Networks with Dynamical Synapses

by

FUNG, Chi Chung

This is to certify that I have examined the above PhD thesis
and have found that it is complete and satisfactory in all respects,
and that any and all revisions required by
the thesis examination committee have been made.

Prof. K. Y. Michael Wong, Thesis Supervisor

Prof. Michael S. Altman, Head of Department

Department of Physics

23 August 2013

Acknowledgments

I would like to express my deep gratitude to my supervisor, Prof. K. Y. Michael Wong, who has given me a lot of advice and kind support in my research during three years of my PhD study. I would like to thank the Department of Physics for providing me with postgraduate studentship award so that I have the valuable opportunity to study here. I would like to thank the postgraduate students in the Department of Physics who have given me a lot of help and valuable opinions in different ways. Also, I would like to thank Prof. Si Wu (Beijing Normal University, China) and Prof. S. Amari (RIKEN, Japan), for supporting the research direction of my postgraduate study. In addition, I would like to thank Prof. H. Benjamin Peng (Division of Life Science, The Hong Kong University of Science and Technology), Prof. Xiangrong Wang (Department of Physics, The Hong Kong University of Science and Technology), Prof. Bradley A. Foreman (Department of Physics, The Hong Kong University of Science and Technology), Prof. Changsong Zhou (Hong Kong Baptist University) and Prof. Chi Keung Chan (Academia Sinica, Taiwan) for taking time to be examiners of my thesis examination and Prof. Wa-Hung Leung (Department of Chemistry, The Hong Kong University of Science and Technology) for chairing the examination. Lastly, I would like to appreciate the support of my family.

Contents

Title Page	i
Authorization Page	ii
Signature Page	iii
Acknowledgments	iv
Table of Contents	v
List of Figures	viii
Abstract	xv
Chapter 1 Introduction	1
1.1 Background	1
1.2 Neural Network and Attractors	2
1.3 Population Code and Continuous Attractor	3
1.4 Motivation	5
1.5 Outline of the Thesis	6
Chapter 2 Review: Continuous Attractor Neural Networks	7
2.1 Introduction	7
2.2 The Model	7
2.3 Reaction to a Change of a Stimulus - Tracking	9
2.4 The Perturbative Analysis	11
2.5 Summary	14
Chapter 3 Review: Continuous Attractor Neural Networks with Synaptic Depression	16
3.1 Introduction	16
3.2 The Model	17

3.3	Intrinsic Dynamics of Continuous Attractor Neural Networks with Short-term Synaptic Depression	18
3.4	Perturbation on Continuous Attractor Neural Networks with Short-term Synaptic Depression	19
3.5	Summary	22
Chapter 4	Continuous Attractor Neural Networks with Synaptic Plasticity	23
4.1	Introduction	23
4.2	The Model	24
4.3	General Perturbative Expansions on Dynamical Variables	25
4.4	Intrinsic Dynamics of Continuous Attractor Neural Networks with Short-term Synaptic Facilitation	29
4.5	CANNs with STF as a Noise Filter	30
4.6	Summary	34
Chapter 5	Tracking with Synaptic Depression	35
5.1	Introduction	35
5.2	Modulation of Tracking Dynamics due to Short-term Synaptic Depression	37
5.3	Perfect Tracking & Anticipatory Tracking	40
5.4	Tracking with Natural Speed of the Continuous Attractor Neural Network	45
5.5	CANNs with Mexican-hat Coupling	48
5.6	Summary	48
Chapter 6	A Model That Enhances Perception Resolution	51
6.1	Introduction	51
6.2	Input with Fluctuations	55
6.3	Population Spikes	56
6.4	Temporal Modulation as a Strategy to Represent Overlapped Information	60
6.5	Conditions of the Theory	64
6.6	Robustness and Biological Relevance	65
6.7	Summary	66
Chapter 7	Two-dimensional Continuous Attractor Neural Networks with Synaptic Depression and Local Subtractive Inhibition	69
7.1	Introduction	69
7.2	Two-dimensional Continuous Attractor Neural Networks with Synaptic Depression and Global Inhibition	70

7.3 Two-dimensional Continuous Attractor Neural Network with Local Subtractive Inhibition	78
7.4 Discussion	85
Chapter 8 Conclusion	90
Appendix A Consistency with the Model of Tsodyks, Pawelzik, and Markram	95
A.1 The Model of Tsodyks, Pawelzik, and Markram	95
Appendix B Recursions of C_{nm}^k, D_{nml}^k, E_{nm}^k and F_{nml}^k	96
B.1 Recursions	96
Appendix C Derivation of $\tilde{\beta}_{\text{perfect}}$	98
C.1 First Order Perturbation Equations	98
C.2 Derivation of The Perfect Tracking Solution	100
C.3 Deviations from Perfect Tracking	102
Appendix D Tracking Weak Moving Stimuli at the Natural Velocity	105
List of Publications	109
Bibliography	111

List of Figures

- Figure 1.1 Illustration of attractors of neural networks with discrete attractors. The plane represents the state space of the neural network. For networks with discrete attractors, there are discrete point attractors on the space of the neural network. Between those point attractors, there are basins of attraction (dashed lines). They partitions the state space into different partitions corresponding to different point attractors. For initial states within a certain partition, the network state evolves to the point attractor corresponding to the partition. 4
- Figure 1.2 Left: Neurons A, B and C with difference preferred orientation. Middle: Tuning curves correspond to neurons A, B and C. The tuning curve peaks at the preferred orientation of the corresponding neuron. Right: The firing rate profile as a function of preferred orientation of neurons. 4
- Figure 1.3 Energy landscape of the system. Horizontal plane corresponds to state space of the system. Vertical axis is the energy of a network state. The bottom of the canyon is the attractor space labeled by a thick solid curve. Each point of the solid attractor space represents an attractor profile of firing rates. If the network firing rate profile is not bump-shaped, its energy is higher. The network state will relax to its closest attractor profile. r : firing rate. x : preferred stimuli of neurons. 6
- Figure 2.1 Stationary states of CANNs with $k/k_c = 0.5$ centered at various points. $\tilde{u}(x, t) \equiv \rho J_0 u(x, t)$. Parameters: $a = 0.5$, $J_0 = \sqrt{2\pi}a$ and $\rho = 256/(2\pi)$ 10
- Figure 2.2 Effective energy landscape of CANNs. States minimizing the energy are attractors of the neural network, labeled by the thick dashed line. In a CANN, attractor states are bump-shaped functions of x . Dotted lines: neuronal activity profiles. 10
- Figure 2.3 Tracking of the network state when the external input changes from 0 to 1.5. Raster plot: $\tilde{u}(x, t)$. Here, $\tilde{u}(x, t) \equiv \rho J_0 u(x, t)$. Dashed line: the center of mass of $\tilde{u}(x, t)$. Parameters: $k/k_c = 0.5$, $a = 0.5$, $J_0 = \sqrt{2\pi}a$, $\rho = 256/(2\pi)$ and $\rho J_0 A = 0.5$ 11
- Figure 2.4 Snapshots of the neuronal inputs in the center-of-mass frame of the bump. Final position of the abrupt-change stimulus is 2.0. Symbols: simulations. Solid lines: predicted synaptic input with the $n = 10$ perturbation (expand $u(x, t)$ up to $n = 10$). Dashed lines: synaptic input at $t = 0$. Parameters: $A/\bar{u}_0 = 0.15$, $a = 0.5$, $k = 0.5$, $\rho = 200/(2\pi)$ and $J_0 = \sqrt{2\pi}a$ 15

Figure 3.1	Action potentials, or spikes, on the presynaptic side cause releases of neurotransmitters, represented by triangles. Neurotransmitters diffuse to the terminal of the postsynaptic neuron. Neurotransmitters cause openings of ion channels of the postsynaptic neuron. Openings of ion channels can change the membrane potential of the postsynaptic neuron. However, since the recovery time of neurotransmitters is longer than the dynamics of the membrane potential and synaptic current, the synaptic efficacy would be reduced. The reduction of synaptic efficacy is called short-term synaptic depression.	18
Figure 3.2	Raster plots of $\tilde{u}(x, t)$ for two sets of parameters and without an external input ($\tilde{I}^{\text{ext}} = 0$). Parameters are labeled at the top of each plot. (a) $\tilde{\beta}$ is too small to support spontaneously moving profile of $\tilde{u}(x, t)$. (b) $\tilde{\beta}$ is large enough to support spontaneous motions.	20
Figure 3.3	Snapshots of profiles of $\tilde{u}(x, t)$ and $p(x, t)$ for various sets of parameters and without an external input ($\tilde{I}^{\text{ext}} = 0$) as functions of preferred stimulus relative to the center of mass of $\tilde{u}(x, t)$. Parameters are labeled at the top of each plot. (a) $\tilde{u}(x, t)$ and $p(x, t)$ are symmetric. $\tilde{u}(x, t)$ will not move spontaneously. (b) $p(x, t)$ is slightly asymmetric. $\tilde{u}(x, t)$ moves slowly due to the asymmetry of $p(x, t)$. (c) $p(x, t)$ is highly asymmetric due to the fast motion of $\tilde{u}(x, t)$, while $\tilde{u}(x, t)$ moves quickly due to the asymmetric synaptic efficacy.	20
Figure 3.4	Illustration of how the asymmetric $p(x, t)$ sustains the motion of bump-shaped profile of $u(x, t)$. The motion of $u(x, t)$, labeled by the arrow, can make the profile of $p(x, t)$ asymmetric about the center of mass of $u(x, t)$. However, since $p(x, t)$ is asymmetric, the suppression effect on $u(x, t)$ due to $p(x, t)$ is asymmetric. In addition to the local excitation of the CANN, the $u(x, t)$ profile travels to the area with larger $p(x, t)$. As a result, the motion can sustain.	20
Figure 3.5	The phase diagram for a CANN with STD. Parameter: $\tau_d/\tau_s = 50$	21
Figure 4.1	An illustration of short-term synaptic facilitation. Release of neurotransmitters increase the calcium level of the presynaptic neuron. The rise of calcium level increases the possibility of neurotransmitters for the next action potential. As a result, the synaptic efficacy get strengthened.	23
Figure 4.2	Plateau states of the network with different initial condition (A and B). (a) $\tilde{u}(x, t)$ and (b) $1 - p(x, t)$ are presented. Squares: simulation with initial condition A. Circles: simulation with initial condition B. Dashed lines: prediction by second order p -perturbation. Solid lines: prediction by second order full perturbation. Parameters: $\tilde{k} = 0.95$, $\tilde{\beta} = 0.0085$ and $\tau_d/\tau_s = 50$	28
Figure 4.3	Phase diagram of CANNs with STF for $\tau_f/\tau_s = 50$ and $f_{\max} = 1$	29

Figure 4.4	A plot of centers of mass of $\tilde{u}(x, t)$ as functions of t under various levels of STF. Other parameters: $\tilde{A} = 7.9788$, $\tau_f/\tau_s = 50$	31
Figure 4.5	A comparison between CANNs with and without STF under the influence of a noisy external input. Dotted line: case without STF. Solid line: case with STF. Other parameters: $a = 0.5$, $x \in [-\pi, \pi]$, $\tilde{k} = 0.25$, $\rho = 80/(2\pi)$, $\tilde{A} = 1.596$ and $T = 0.02$	32
Figure 4.6	The decoding errors of the network versus different levels of noise. Parameters other than T are the same as those in Figure 4.5. Symbols: simulations. Dashed line: predictions for $\tilde{\alpha} = 0$. Dotted line: predictions for $\tilde{\alpha} = 0.1$	33
Figure 5.1	(a) Phase diagram of CANNs with STD over the parameter space spanned by $(\tilde{k}, \tilde{\beta})$. Here, \tilde{k} is the rescaled inhibition and $\tilde{\beta}$ is the rescaled level of STD. (b) Speed of spontaneously moving network state profile (v). Other parameter: $\tau_d/\tau_s = 50$	36
Figure 5.2	The network reaction to a moving stimulus. Raster plot: $\tilde{u}(x, t)$. Dashed line: moving stimulus, $z_0(t)$. Solid line: the center of mass of $\tilde{u}(x, t)$, $z(t)$. Parameters: $\tilde{k} = 0.5$, $\tilde{\beta} = 0$, $\tilde{A} = 1.0$ and $\tau_s v/a = 0.04$	39
Figure 5.3	Centers of mass of $\tilde{u}(x, t)$ for various $\tilde{\beta}$'s. Symbols: simulations. Dashed line: the moving stimulus, $z_0(t)$. Solid line: prediction by $k = 5$ perturbation. Other parameters: $\tilde{k} = 0.4$, $\tilde{A} = 1.8$, $\tau_s v/a = 0.0002$ and $\tau_d/\tau_s = 50$	39
Figure 5.4	(a) The terminal displacements s as functions of velocities of external stimuli in three particular sets of parameters. Parameters: $\tilde{k} = 0.4$, $\tilde{A} = 1.8$ and $\tau_d/\tau_s = 50$. (b) The terminal displacements s as a function of $\tilde{\beta}$ and v . Grid: the surface plot of s against $\tilde{\beta}$ and v . Bottom: a contour plot. ‘++’: in the region, $s/a > 0.2$. ‘+’: $0 < s/a < 0.2$. ‘-’: $-0.2 < s/a < 0$. ‘-’: $s/a < -0.2$	41
Figure 5.5	$\tilde{\beta}$ for perfect tracking against \tilde{k} for $\tilde{A} = 1.8$. Dotted line: phase boundary for the static phase in Figure 5.1(a). Parameter: $\tau_d/\tau_s = 50$	44
Figure 5.6	Plot of $\tilde{\beta}_{\text{perfect}}$ against \tilde{A} for various \tilde{k} 's. Symbols: simulations. Curves: predictions for corresponding \tilde{k} . Parameter: $\tau_d/\tau_s = 50$	44
Figure 5.7	Anticipatory time as a function of the speed of the moving stimulus. Curves: predictions given by the model with different parameters. Symbols with error bars: experimental results quoted in [32]. Primary horizontal axis: controlled parameter in the model. Primary vertical axis: predicted anticipatory time by the model. Secondary horizontal axis: angular velocity of rodents quoted in [32]. Secondary vertical axis: measured anticipatory time quoted in [32]. Parameter: $\tau_d/\tau_s = 50$	46

Figure 5.8	Anticipatory time over the phase diagram. Dotted line: phase boundaries in Figure 5.1(a). Parameters: $\tilde{A} = 0.5$ and $\tau_d/\tau_s = 50$	46
Figure 5.9	The dependence of the displacement s on the stimulus speed v . The confluence points of the two families of curves are marked by the arrows. Symbols: simulations. Solid lines: 11 th order perturbation. L_1 : natural speed at $\tilde{\beta} = 0.005$. L_2 : natural speed at $\tilde{\beta} = 0.01$. L_3 : the line of natural tracking points in the strong \tilde{A} limit. Parameter: $\tilde{k} = 0.3$	47
Figure 5.10	(a) The dependence of anticipatory time on the stimulus speed in the Mexican-hat model. Parameter: $\beta = 0.003$. (b) Natural speed of the network as a function of β . (c) Plot of s against v . There is a confluence point at the natural speed of the system. L_1 : the natural speed of the system at $\beta = 0.0011$. Common parameters: $\rho = 128/(2\pi)$, $J_0 = 0.5$ and $a = 0.5$	49
Figure 6.1	(a) - (c) The profile of two superposed Gaussian functions with the same height. $f(x) \equiv \{\exp[(x - \Delta z/2)^2/(2a^2)] + \exp[(x + \Delta z/2)^2/(2a^2)]\}/2$. Red solid line: $y = f(x)$ with different Δz . Dashed line: $y = f(x)$ with $\Delta z = 0$ as a reference. (a) $\Delta z = 0$. (b) $\Delta z =$ tuning width $= 2a$. (c) $\Delta z = 110\%$ tuning width $= 2.2a$. (d) The profile of two superposed Gaussian functions with different heights to illustrate how the amplitude fluctuations provide a cue to distinguish the components. $g(x) \equiv \{A_0 \exp[(x - \Delta z/2)^2/(2a^2)] + A_1 \exp[(x + \Delta z/2)^2/(2a^2)]\}$. Dashed line: $y = f(x)$ with $\Delta z = 0$ as a reference. Red solid line: $y = g(x)$ with $\Delta z =$ tuning width, $A_0 = 0.4$ and $A_1 = 0.6$. Blue solid line: $y = g(x)$ with $\Delta z =$ tuning width, $A_0 = 0.6$ and $A_1 = 0.4$	54
Figure 6.2	The shaded region is the parameter region for $\tilde{k} = 0.5$ and $n = 1$ in Eq. (6.6) to achieve population spike. Cross: particular cases to be discussed in this chapter. $\tau_d/\tau_s = 50$. The boundary is provided by Wang [45]. Points B to H correspond to cases in Figure 6.8. Point A is the case I used to illustrate the theory in Figures 6.3 - 6.7.	55
Figure 6.3	Firing rates $\tilde{r}(x, t)$ ((a), (d) and (g)), available fraction of neurotransmitters $p(x, t)$ ((b), (e) and (h)) and corresponding input ((c), (f) and (i)) for various magnitudes of single-peaked external inputs. (a)-(c) $\tilde{A} = 0.4$, (d)-(f) $\tilde{A} = 0.8$ and (g)-(i) $\tilde{A} = 2.0$. Other parameters: $\tilde{k} = 0.5$, $\tilde{\beta} = 0.24$, $a = 48\pi/180$ and $\tau_d = 50\tau_s$	57
Figure 6.4	(a) $\max_x \tilde{r}(x, t)$ as a function of t corresponding to Figures 6.3(a), (d) and (g). (b) $\min_x p(x, t)$ as a function of t corresponding to Figure 6.3(b), (e) and (h). Parameters: the same as Figure 6.3.	58
Figure 6.5	Raster plot of firing rates \tilde{r} for (a) $\Delta z = 0.5$, (b) $\Delta z = 1.0$ and (c) $\Delta z = 2.0$. Black dashed lines: positions of stimuli. Parameters: $\tilde{k} = 0.5$, $\tilde{\beta} = 0.24$, $a = 48\pi/180$, $\tilde{A} = 0.8$, $\sigma = 0.3$ and $\tau_d = 50\tau_s$	58

Figure 6.6	(a) Time average of firing rates \tilde{r} as a function of the preferred stimuli of neurons, x , and the separation between the two stimuli, Δz . Contour lines: $\langle \tilde{r} \rangle_t = 1$ (dotted-dashed line), $\langle \tilde{r} \rangle_t = 2$ (dashed line), $\langle \tilde{r} \rangle_t = 3$ (solid line), $\langle \tilde{r} \rangle_t = 4$ (dotted line). Parameters: same as Figure 6.5. (b) The average neural activity recorded by Treue <i>et al.</i> in [37] (with license number 3178600066018 for the reuse purpose). (c) Contours of the distribution of peak positions higher than 6.2 as a function of preferred stimuli, x , and the separation between the two stimuli, Δz . White dashed line: positions of the two stimuli. L_1 : one-third of the tuning width. L_2 : tuning width. Parameters: same as Figure 6.5.	59
Figure 6.7	The mean separation of peak positions of $\tilde{r}(x, t)$ shown in Figure 6.6(c). Symbols: simulation. Dashed line: diagonal line representing perfect distinguishability.	60
Figure 6.8	(a) The phase diagram of population spikes over the parameter space spanned by $(\tilde{A}, \tilde{\beta})$ with the parameter $\tilde{k} = 0.5$ and $\tau_d/\tau_s = 50$. (b) - (h) are distributions of the occurrence of peak positions as function of Δz . The numbers at the top of (b) - (h) are thresholds used to sample peak positions. Parameters: (b) $\tilde{A} = 0.4$ and $\tilde{\beta} = 0.35$. (c) $\tilde{A} = 0.65$ and $\tilde{\beta} = 0.35$. (d) $\tilde{A} = 0.9$ and $\tilde{\beta} = 0.35$. (e) $\tilde{A} = 0.4$ and $\tilde{\beta} = 0.2$. (f) $\tilde{A} = 0.6$ and $\tilde{\beta} = 0.2$. (g) $\tilde{A} = 0.7$ and $\tilde{\beta} = 0.1$. (h) $\tilde{A} = 0.9$ and $\tilde{\beta} = 0.2$	61
Figure 6.9	Contours of the distribution of peak positions higher than 6.2 as a function of preferred stimuli, x , and the separation between the two outermost stimuli, Δz , in the case of three equally strong stimuli. White dashed line: positions of three stimuli. Horizontal dotted line: the case comparable to the three-stimulus experiment reported by Treue <i>et al.</i> [37]. Vertical dashed lines: perception ($\pm 40^\circ$) reported by subjects in the experiment in units of the tuning width (96°). Parameters: same as Figure 6.3.	63
Figure 6.10	(a) Raster plot of firing rate \tilde{r} of the network with two stimuli and without STD. Parameters: $\tilde{k} = 0.5$, $\tilde{\beta} = 0$, $\tilde{A} = 0.8$, $a = 48\pi/180$, $\sigma = 0.3$ and $\Delta z = 3.1$. (b) Raster plot of firing rate \tilde{r} of the network with two stimuli with weak net input profile. Parameters: $\tilde{k} = 0.5$, $\tilde{\beta} = 0.24$, $\tilde{A} = 0.4$, $a = 48\pi/180$, $\sigma = 0.3$ and $\Delta z = 2.5$. (c) Raster plot of firing rate \tilde{r} of the network with two stimuli without height fluctuations in the external input profile. Parameters: $\tilde{k} = 0.5$, $\tilde{\beta} = 0.24$, $\tilde{A} = 0.8$, $a = 48\pi/180$, $\sigma = 0$ and $\Delta z = 1.67$. (d) Contours of the distribution of peak positions for all peak heights. White dashed line: positions of the two stimulus components. Parameters: $\tilde{k} = 0.5$, $\tilde{\beta} = 0.24$, $\tilde{A} = 0.8$, $a = 48\pi/180$, $\sigma = 0.3$ and $\Delta z = 1.0$	68
Figure 6.11	The time-averaged dynamical variable $p(x, t)$. Symbols and red line: measurement from the simulation. Blue lines: positions of two stimuli. Parameters: $\tilde{k} = 0.5$, $\tilde{\beta} = 0.24$, $a = 48\pi/180$, $\tau_d/\tau_s = 50$, $\tilde{A} = 0.8$, $\sigma = 0.3$ and Δz = tuning width of attractor states.	68

Figure 7.1	Solution of $\rho J_0 u_{00}$ as a function of k/k_c . For each k/k_c less than 1, the larger solution of $\rho J_0 u_{00}$ is stable, while the smaller solution is unstable.	72
Figure 7.2	(a) Parabolas given by Eq. (7.12). (b) Grey curves are stable branches of parabolas in (a). Solid line is the phase boundary of static bumps.	73
Figure 7.3	Phase diagram of different phases under this theoretical framework. Circles: boundary of the translational stability through simulations. Squares: boundary of the amplitude stability through simulations. Triangles: boundary of the stability of moving bumps through simulations. Curves: corresponding theoretical predictions. Parameter: $\tau_d/\tau_s = 50$	76
Figure 7.4	Measurements and predictions of \tilde{u}_{00}/B . Symbols: measurements from various \tilde{k} . Curves: Different levels of predictions of $0 \leq \tilde{k} \leq 1$. Parameter: $\tau_d/\tau_s = 50$	76
Figure 7.5	Measurements and predictions of $(\tilde{u}_{20} + \tilde{u}_{02})/B$. Symbols: measurements from various \tilde{k} . Curves: Different levels of predictions for $0 \leq \tilde{k} \leq 1$. Parameter: $\tau_d/\tau_s = 50$	79
Figure 7.6	Measurements and predictions of $\sqrt{(\tilde{u}_{20} - \tilde{u}_{02})^2 + \tilde{u}_{11}^2}/B$. Symbols: measurements from various \tilde{k} . Curves: Different levels of predictions for $0 \leq \tilde{k} \leq 1$. Parameter: $\tau_d/\tau_s = 50$	79
Figure 7.7	Measurements and predictions of the intrinsic moving speed. Symbols: measurements from various \tilde{k} . Curves: Different levels of predictions for $0 \leq \tilde{k} \leq 1$. Parameter: $\tau_d/\tau_s = 50$	80
Figure 7.8	Maximum τ_B/τ_s able to stabilize the amplitude of stationary solutions as a function of γ , given that $\tilde{k} = 0.3$. L_1 : maximum γ of the existence of stationary solutions. L_2 : maximum γ of the existence of stationary solution with stable amplitude at the limit $\tau_i/\tau_s \rightarrow +\infty$	82
Figure 7.9	Speed of spontaneous motions as a function of γ	86
Figure 7.10	Phase diagram over the parameter space spanned by (\tilde{k}, γ) . Dotted line: predicted boundary for moving solutions by $k_0 + k_1 = 2$ perturbation. Solid line: predicted boundary for moving solutions by $k_0 + k_1 = 10$ perturbation. Dotted line: predicted boundary for static solutions with stable amplitudes by $k_0 + k_1 = 0$ perturbation. Dot-dashed line: predicted boundary for static solutions with stable amplitudes and translational stability by $k_0 + k_1 = 0$ perturbation. Parameters: $a = 0.5$, $\tau_i/\tau_s = 10$ and $\tau_B/\tau_s = 0.1$. Symbols: corresponding simulations.	87
Figure 7.11	Projection of $\tilde{u}(x, t)$ on $\phi_0(\xi_0)\phi_0(\xi_1)$ at $\tilde{k} = 0.5$. Other parameters: same as Figure 7.10.	87
Figure 7.12	Projection of $\tilde{u}(x, t)$ on rotational symmetric basis function with $k_0 + k_1 = 2$. Parameters: same as Figure 7.10.	88

Figure 7.13 Projection of $\tilde{u}(x, t)$ on anisotropic basis function with $k_0 + k_1 = 2$.
Parameters: same as Figure 7.10. 88

Figure C.1 Comparison of the contours of constant anticipatory time $10\tau_s$ between numerical solutions and the 1st order perturbation at $\tilde{A} = 1$ 104

Figure D.1 (a) The natural tracking curves for various values of \tilde{k} . (b) The dependence of the displacement on the stimulus speed at $\tilde{k} = 0.3$ and $\tilde{\beta} = 0.005$. Solid line: natural speed of the system. Dot-dashed line: prediction by Eq. (D.8). (c) The dependence of the anticipatory time on the stimulus speed at $\tilde{k} = 0.3$ and $\tilde{\beta} = 0.005$. Solid line: natural speed of the system. Dot-dashed line: prediction by Eq. (D.8). 107

Dynamics of Continuous Attractor Neural Networks with Dynamical Synapses

by

FUNG, Chi Chung

Department of Physics
The Hong Kong University of Science and Technology

Abstract

Continuous attractor neural networks (CANNs) are models that describe neuronal systems having localized activities to represent continuous information. Head-direction (HD) cells, place cells and orientation selective cells in the primary visual cortex are examples. In a CANN, due to the localized excitatory couplings, tuning curves of neurons are bump-shaped functions of external stimuli. The particular stimulus that the activity of a neuron is maximized is the preferred stimulus of that neuron. As a result, the neuronal activities in a CANN are also bump-shaped functions of the preferred stimulus of the neurons. If the synapses (the couplings between neurons) in a CANN are static, the neuronal activity profile will also be stable. However, if the synapses are dynamical, the neuronal activity profile may be unstable. There are two possibilities that make synapses dynamical. Short-term synaptic depression (STD) is an effect that can temporally degrade the synaptic efficacy due to the recent firing history of the presynaptic neuron. This is due to the fact that the recovery time of neurotransmitters (~ 100 ms) is longer than the time scale of synaptic current (~ 1 ms). STD can destabilize the bump-shaped states in CANNs. Several contributions are reported in this thesis. First, I report that STD enables the CANN to support plateau states, which can be a mechanism of sensory memory. Also, STD can translationally destabilize states in CANNs. This translational instability enables the CANN to implement anticipation as a mechanism of delay compensation in the nervous system, which was also observed in rodent experiments. The novelty of the proposed mechanism is based on the inherent and ubiquitous nature of STD of neurons, and does not require dedicated neuronal mechanisms and network structures as was the case in previous models. Second, under

the influence of external inputs and STD, there are periodic excitements of the neuronal activity. We found that the resolution of CANNs can be improved significantly due to the periodic excitements. Also, the simulation results are comparable to psychology experiments and neuroscience experiments. This suggests a novel way to encode multiple almost-overlapped stimuli. Third, I studied Short-term synaptic facilitation (STF) an effect that can temporally enhance the synaptic efficacy. This effect is due to the rise of calcium level in the presynaptic neuron after a spike. STF can stabilize the network states. It can be used to reduce the effect of noisy stimuli. Fourth, apart from the study of one-dimensional (1D) CANN, in the thesis, I also present the study on the intrinsic dynamics of two-dimensional (2D) CANN with STD and local subtractive inhibition.

Chapter 1

Introduction

1.1 Background

Brains are mystical. They are believed to achieve various functions, e.g. memory, decision making and perceptions, while our knowledge about brains is still not sufficient to understand the working principles of brains. Not only is the brain complicated, but also brain cells, namely neurons, are complicated.

A simplified model of neurons is the integrate-and-fire (IF) model [1]. In this model, neurons are modeled as a capacitor. One side of the capacitor models the electric potential outside the cell membrane, while the other side of the capacitor models the electric potential inside the cell membrane. The electric potential outside the cell is usually set to 0. Due to natural chemical conditions, the equilibrium potential inside the cell is about -70 mV. Receptions of spikes from other neurons cause changes of the potential difference across the membrane. If the potential reaches the threshold (about -50 mV), the neuron will generate an action potential (*spike*), which is about +10 mV. After a spike, the potential returns back to -70 mV. The neuronal refractory period is of the order of the magnitude of 1 ms. This is usually neglected, if a pool of neurons are considered. The generated action potential will raise or lower the potentials of coupled neurons.

Taking a closer look, action potentials are generated on soma (cell body) or dendrites. The action potential can propagate along the axon. When the action potential arrives at a terminal of the *presynaptic neuron*, neurotransmitters will be released from the presynaptic neuron and diffuse to the dendrite of the *postsynaptic neuron*. Neurotransmitters can open ion channels of the postsynaptic neuron. Because of the ion influxes, the potential of the postsynaptic neuron changes accordingly. Neurons releasing neurotransmitters that are able to raise other neurons' potential are called excitatory neurons, while neurons releasing neurotransmitters to reduce other neurons' potential are called inhibitory neurons.

However, the concentration of neurotransmitters depends on the past spiking history of the presynaptic neuron on a long time scale, because the recovery time for neurotransmitters is significantly longer than the inter-spike time. If the neuron spikes frequently recently, the synaptic efficacy will be degraded. However, the calcium ion concentration will be increased after spikes. The rise of the calcium level can increase the release probability of neurotransmitters. So, this effect can enhance the synaptic efficacy. Tsodyks *et al.* proposed a model to explain this phenomenon [2]. The short-term degradation of the synaptic efficacy due to lowered concentration of neurotransmitter is called short-term synaptic depression (STD), while the short-term enhancement of the efficacy due to the increase of calcium level is called short-term synaptic facilitation (STF). These effects are together called short-term synaptic plasticity (STP).

Since the short-term synaptic plasticity (STP) have a time scale relatively longer than that of the membrane potential, the dynamics due to STP is very rich. In this thesis, I will present a model of a population of neurons with STP. Neuronal systems with STP may exhibit non-trivial intrinsic internal dynamics. The intrinsic dynamics can affect the behavior of the neuronal system responding to the external stimulus.

1.2 Neural Network and Attractors

In the brain, neurons are believed to work together to achieve various brain functions. The key to achieving this purpose is the couplings between neurons. Memory formation is still an open question. However, there are long-term effects believed to be relevant to learning. Those long-term effects include long-term potentiation (LTP) and long-term depression (LTD). These effects are consequences of spike timing dependent plasticity [3]. Let us consider two neurons, A and B. A is the presynaptic neuron, while B is the postsynaptic neuron. If neuron A always spikes right before B, the coupling from A to B will be strengthened. However, if A always spikes right after B, the coupling from A to B will be weakened. This mechanism enables the network of neurons to learn particular patterns. This ability is believed to implement the memory formation task.

The spike rate of a neuron is believed to contain the information of the spike train. So, in some relatively simple models, the neuronal state is modeled by a quantity related to neuronal activity. For example, in the Hopfield model [4], the state of neuron i , σ_i , is modeled by 1 (corresponding to high spike rate) and -1 (corresponding to low spike

rate). The state of a neuron is determined by

$$\sigma_i = \text{sgn} \left(- \sum_j J_{ij} \sigma_i \sigma_j \right), \quad (1.1)$$

where sgn is the sign function. This binary model is very similar to the mean-field approximation of the Ising model. Attractors are defined by the coupling J_{ij} . Based on Hebb's postulate [5], to store p binary patterns, one could define

$$J_{ij} = \frac{1}{N} \sum_{\mu=1}^p \xi_i^\mu \xi_j^\mu, \quad (1.2)$$

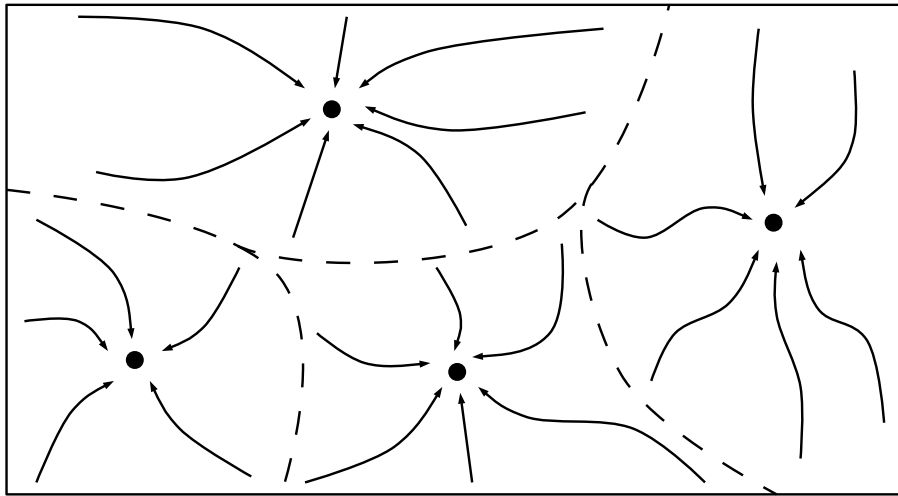
where N is the number of neurons, μ is the index of the pattern to be stored, ξ_i^μ is the prospected state of the neuron i and p is the number of patterns. This learning is not the same as the spike timing dependent plasticity, as the spike timing information is not included in the formalism. However, this rule suggests that if the firing rates of two neurons are positively correlated on average, the coupling between them should be strong, which still keep the spirit of the spike timing learning rule.

After the learning phase, obviously, the neuronal network would favor some particular spike rate patterns. These spike rate patterns are called attractors of the network. As illustrated in Figure 1.1, the internal dynamics of the neuronal network will drive the initial state of the network to the closest attractor.

1.3 Population Code and Continuous Attractor

Real neurons do not work as a device with binary states. Their spike rate should be a positive real number. In experiments, some neurons are found to have preferences on some continuous information. Here, the preference refers to the spike rate. If the information is preferred by the neuron, the spike rate will be higher than that with less preferred information. This preferred information can be used to label the neuron, known as *preferred stimulus*. Spatial location in the environment [6], orientation [7] and moving direction of the object [8] are examples of the continuous information. In the primary visual cortex (V1), some neurons will prefer particular texture of the visual input [9].

Let us consider an orientation of an object as an example, illustrated in Figure 1.2. For example, consider the neuron prefers 0° orientation. Its spike rate will be a bump-shaped function of the input orientation centered at 0° , as shown in Figure 1.2.



State Space of the Neural Network

Figure 1.1: Illustration of attractors of neural networks with discrete attractors. The plane represents the state space of the neural network. For networks with discrete attractors, there are discrete point attractors on the space of the neural network. Between those point attractors, there are basins of attraction (dashed lines). They partitions the state space into different partitions corresponding to different point attractors. For initial states within a certain partition, the network state evolves to the point attractor corresponding to the partition.

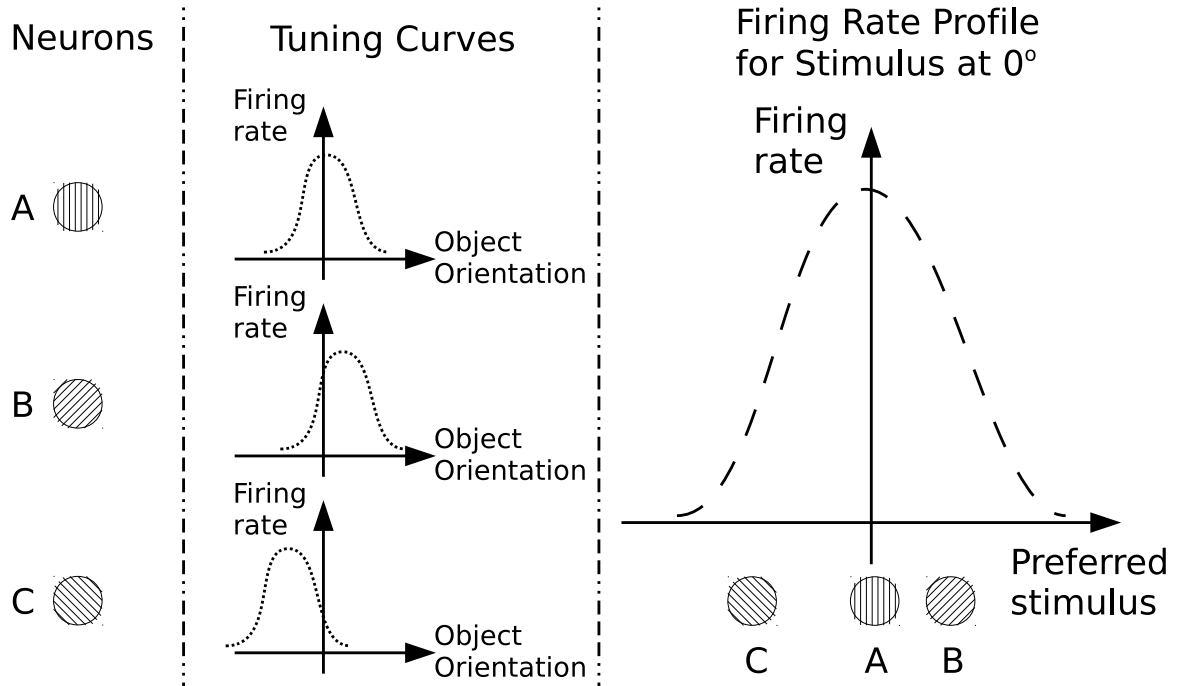


Figure 1.2: Left: Neurons A, B and C with difference preferred orientation. Middle: Tuning curves correspond to neurons A, B and C. The tuning curve peaks at the preferred orientation of the corresponding neuron. Right: The firing rate profile as a function of preferred orientation of neurons.

This bump-shaped curve is called the *tuning curve* of the neuron. Since different neurons may have different preferred orientations, there is a bump-shaped spike rate profile as a function of preferred orientations of neurons representing the orientation of the visual input. This bump-shaped spike rate profile can be used to represent the continuous information in the neural system. This coding strategy is called the population code, as the information is represented by a population of neurons.

The population code is costly. However, the code is very robust. Because the code is represented by a group of neurons, rather than a single neuron, the information will not be easily destroyed even though several neurons die. Also, it makes the neural system more robust against noise. Because the neuronal spike rate is contributed by its neighbors, the effect of the noise may get averaged out.

The models proposed to study the dynamics of these neuronal systems are called continuous attractor neural networks (CANNs). Attractors are neurons' states, or network states, favored by the system due to the coupling and internal dynamics. Continuous attractor means the attractors form a continuous space, which is able to represent continuous information. If we consider the energy landscape of the system analogous to the picture in Figure 1.3, there is a canyon such that, the bottom of the canyon representing the attractors of the system.

1.4 Motivation

Continuous attractor neural networks (CANNs) provides a relatively simple platform to study the collective behavior of neurons in systems like head direction (HD) cells in postsubiculum in freely moving rats [10], place cells in the hippocampus [11, 6] and moving direction cells in the middle temporal (MT) [8]. To understand the general behavior of the system, we need to have a general dynamics picture about how attractor state evolution is affected by dynamics of synapses. By analyzing the dynamics of the system, we can predict its intrinsic states. Also, based on the intrinsic dynamics we found, we proposed several implications of CANN with dynamical synapses. For example, CANN with STD can implement a neural system capable of anticipating the future position of a moving stimulus. Some predictions given by the model can be comparable to Psychology experiments and neuroscience experiments.

In the next chapter, I will review our previous work on analyses of CANNs using a method called the perturbative approach, which is very similar to the time-dependent perturbation used in mechanical systems.

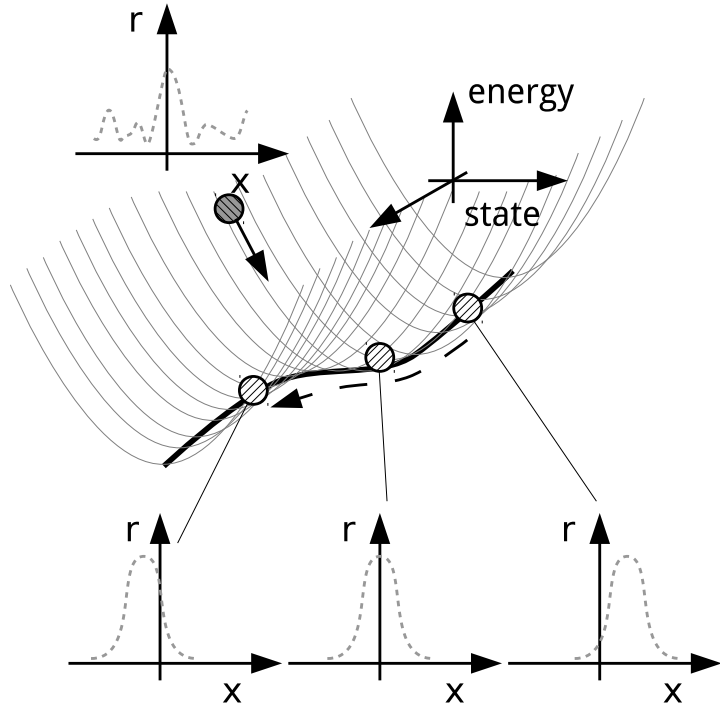


Figure 1.3: Energy landscape of the system. Horizontal plane corresponds to state space of the system. Vertical axis is the energy of a network state. The bottom of the canyon is the attractor space labeled by a thick solid curve. Each point of the solid attractor space represents an attractor profile of firing rates. If the network firing rate profile is not bump-shaped, its energy is higher. The network state will relax to its closest attractor profile. r : firing rate. x : preferred stimuli of neurons.

1.5 Outline of the Thesis

In this thesis, I begin with the background information of the work (this chapter). Then, I review my previous works: CANNs with static couplings (chapter 2) and CANNs with STD (chapter 3). After the introduction and reviews, I present my work during my current study: (1) CANNs with STP (chapter 4), (2) how network states change under the influences of external inputs and STD (chapter 5) (3) how the resolution of a CANN can be improved by the inclusion of STD (chapter 6) and (4) dynamics of two-dimensional (2D) CANNs with STD (chapter 7). The last chapter will be the conclusion of this thesis (chapter 8).

Chapter 2

Review: Continuous Attractor Neural Networks

2.1 Introduction

Continuous attractor neural network (CANN) models are population rate models aimed to study the collective behavior of neurons in a neural network. Networks of integrate-and-fire neurons can also achieve this purpose, but it will be too complicated for analytical purposes. The internal dynamics of CANN can support a local bump-shaped neural firing rate profile over the preferred stimulus space. In this chapter, I will review my theoretical work on a particular model of CANN [12, 13, 14, 15].

2.2 The Model

In the model to study the dynamics of CANNs, the firing rate of neurons with preferred stimulus x at time t is analogized by a quantity called *neuronal activity*, $r(x, t)$, where x is between $-L/2$ and $L/2$. The range of x is L . The neuronal activity is given by

$$r(x, t) = \Theta[u(x, t)] \frac{u(x, t)^2}{1 + \rho k \int dx' u(x', t)^2 \Theta[u(x, t)]}, \quad (2.1)$$

where $u(x, t)$ is the neuronal current of the neuron with preferred stimulus x at time t . In general, $r(x, t)$ is a smooth nonlinear, non-negative and bounded function of $u(x, t)$. Eq. (2.1) is a particular formula chosen by us to simplify the calculation. Θ is the step function. ρ is the density of neurons over the space of preferred stimulus. The denominator of Eq. (2.1) is the divisive global inhibition. This divisive global inhibition

models the shunting inhibition [16, 17]. The dynamics of $u(x, t)$ is given by

$$\tau_s \frac{du}{dt} (x, t) = -u(x, t) + \rho \int_{-L/2}^{L/2} dx' J(x, x') r(x', t) + I^{\text{ext}}(x, t), \quad (2.2)$$

where τ_s is the time scale of the neuronal current (roughly 1 ms). Although the time constant of membrane potentials of neurons of mammals are typically 10 ms, the time constant of synaptic input current can be much shorter than that. For example, for auditory neurons in the chicken, the synaptic input current has a time constant 200 μ s, while the membrane time constant is 2 ms [18]. Also, population of neurons may firing much faster than single neurons [19]. So, the choice of the time constant here is appropriate.

On the right hand side, the first term represents the relaxation of the neuronal current in a time scale of τ_s . The second term arises from the network interactions between neurons, with $J(x, x')$ being the excitatory coupling between neurons with preferred stimulus x and neurons with preferred stimulus x' and $I^{\text{ext}}(x, t)$ is the external input profile. $J(x, x')$ is translationally invariant and depends on only $|x - x'|$. The excitatory coupling is strongest for $x = x'$ and decreases with distance, $|x - x'|$. These local excitatory couplings enable the network to form bump-shaped neuronal activity profiles, while the translational invariance of $J(x, x')$ enables continuous attractors. The excitatory coupling is given by

$$J(x, x') = \frac{J_0}{\sqrt{2\pi}a} \exp\left(-\frac{|x - x'|^2}{2a^2}\right), \quad (2.3)$$

where J_0 is the average strength of the excitatory coupling and a is the range of the excitatory coupling. For $a \ll L$, $\int_{-L/2}^{L/2}$ is effectively $\int_{-\infty}^{\infty}$. In the rest of the thesis, the boundary will be omitted for analyses.

Like many other models of CANNs [20, 7, 3], there exists a family of localized attractor profiles centered at arbitrary points in the preferred stimulus space, when there is no stimulus. Let us consider

$$\bar{u}(x|z) = u_0 \exp\left(-\frac{|x - z|^2}{4a^2}\right) \text{ and} \quad (2.4)$$

$$\bar{r}(x|z) = r_0 \exp\left(-\frac{|x - z|^2}{2a^2}\right), \quad (2.5)$$

where $u_0 = 2\sqrt{2} \left(1 + \sqrt{1 - k/k_c}\right) / (\rho J_0 k / k_c)$ and $r_0 = \sqrt{2}u_0 / (\rho J_0)$. $k_c \equiv \rho J_0^2 / (8\sqrt{2\pi}a)$

is the critical value for k . If $k > k_c$, there will be no bump-shaped solution. The tuning width of the firing rate profile, $\bar{r}(x|z)$, is defined as two times of its variance. Hence the tuning width of the attractor states is $2a$. Note that the width of the neuronal current profile, $\bar{u}(x|z)$, is $\sqrt{2}$ times wider, due to the nonlinear dependence in Eq. (2.1). Because of the translational invariance of Eq. (2.3), this fixed point solution can be centered at any point of the preferred stimulus space, i.e. z is arbitrary, as shown in Figure 2.1. The family of these fixed point solutions forms a continuous attractor. These solutions are also called stationary states of the network.

One can also imagine that there is an effective energy landscape in the space of network states, e.g. Figure 2.2. The description of the effective energy function will be given in Section 2.4. For states not favorable to the neural networks, the effective energy will be higher. The effective energy will be minimized only when the network state is one of the attractors of the neural network. Also, due to the translational invariance of the coupling function $J(x, x')$, the network state can be displaced smoothly along the line continuous attractor.

Numerical simulations are used to verify analytic predictions and explore new phenomena. In each simulation, there are N neurons evenly distributed over the space $[-L/2, L/2]$. The boundary condition is periodic, i.e.

$$x - x' = \begin{cases} x - x' & , \text{ if } -L/2 < x - x' \leq L/2 \\ x - x' + L & , \text{ if } x - x' \leq -L/2 \\ x - x' - L & , \text{ if } x - x' > L/2 \end{cases}. \quad (2.6)$$

The algorithm used to integrate the differential equations is the Runge-Kutta Prince-Dormand (8, 9) method [21]. Parameters will be specified for each simulation result in the thesis.

2.3 Reaction to a Change of a Stimulus - Tracking

Without an external input, the bump-shaped network state can be located at any point of the preferred stimulus space. If there is a non-uniform external input, the steady state of the neural network can only center at some points of the space. For simplicity, we choose

$$I^{\text{ext}}(x, t) = A \exp\left(-\frac{|x - z_0(t)|^2}{4a^2}\right), \quad (2.7)$$

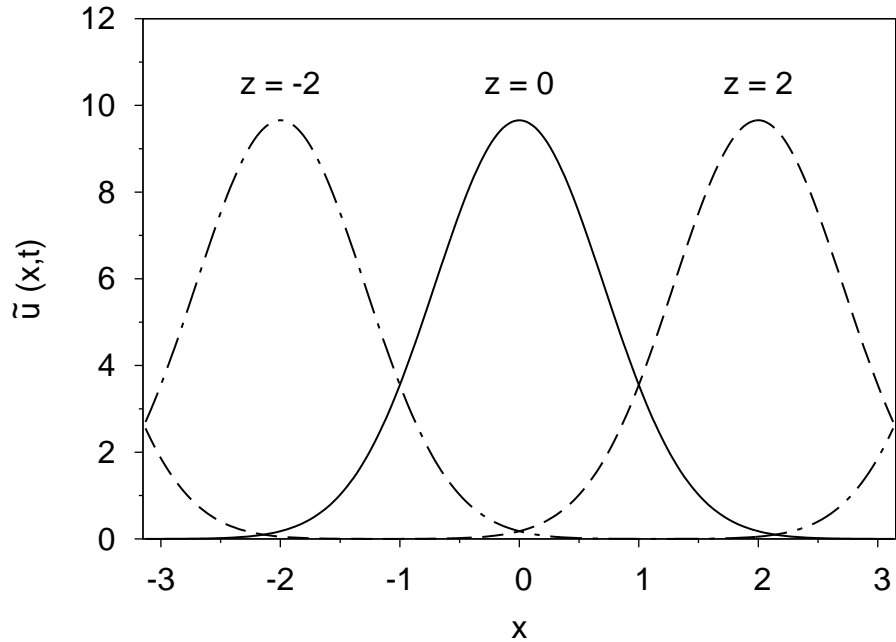


Figure 2.1: Stationary states of CANNs with $k/k_c = 0.5$ centered at various points. $\tilde{u}(x, t) \equiv \rho J_0 u(x, t)$. Parameters: $a = 0.5$, $J_0 = \sqrt{2\pi}a$ and $\rho = 256/(2\pi)$.

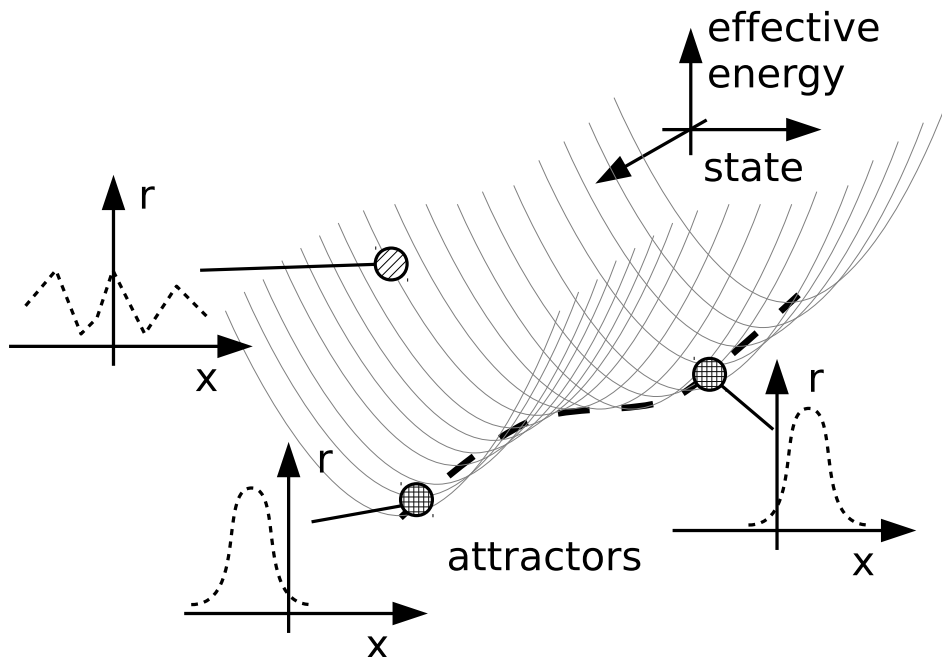


Figure 2.2: Effective energy landscape of CANNs. States minimizing the energy are attractors of the neural network, labeled by the thick dashed line. In a CANN, attractor states are bump-shaped functions of x . Dotted lines: neuronal activity profiles.

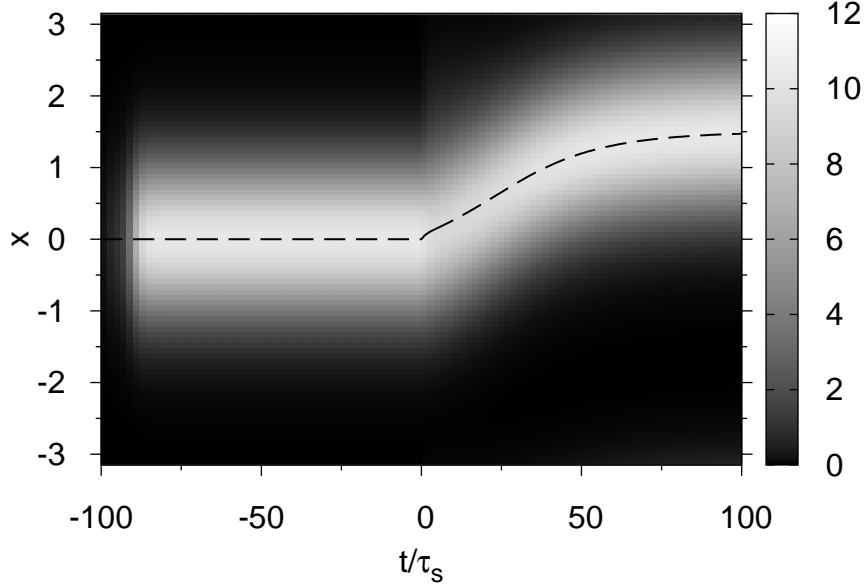


Figure 2.3: Tracking of the network state when the external input changes from 0 to 1.5. Raster plot: $\tilde{u}(x, t)$. Here, $\tilde{u}(x, t) \equiv \rho J_0 u(x, t)$. Dashed line: the center of mass of $\tilde{u}(x, t)$. Parameters: $k/k_c = 0.5$, $a = 0.5$, $J_0 = \sqrt{2\pi}a$, $\rho = 256/(2\pi)$ and $\rho J_0 A = 0.5$.

where A is the strength of the external input and $z_0(t)$ is the position of the stimulus. In Figure 2.3, there is an example of tracking of a bump-shaped network state tracking an external input. At $t = -100\tau_s$, the initial condition of the simulation is $u(x, t) = 0$. The stimulus is

$$z_0(t) = \begin{cases} 0 & , \text{ if } t < 0 \\ 1.5 & , \text{ if } t \geq 0 \end{cases} \quad (2.8)$$

In Figure 2.3, at $t < 0$, the network state coincides with the stimulus. After $t = 0$, the network state does not catch up the stimulus immediately. It tracks the stimulus and finally arrives at the final position of the stimulus. The tracking speed is large at the early stage. Once the network state gets too close to the stimulus, the tracking motion of the network state will slow down.

2.4 The Perturbative Analysis

Usually, equations of the form of Eq. (2.2) are difficult to analyze, because it involves a derivative and a integration. In 2008, we published a method to deal with these systems [12] (detailed calculations in [14]). The method is called the *perturbative method*, which is very similar to perturbation analyses in other physical systems. In this case, we perturb

the distortion of the dynamical variable $u(x, t)$ at z as a perturbation basis

$$\delta u(x, t) \equiv u(x, t) - \bar{u}(x|z(t)) = \sum_n u_n(t) \psi_n(x - z(t)), \quad (2.9)$$

where ψ_n are orthonormal basis functions and $u_n(t)$'s are the corresponding perturbative coefficients. Eq. (2.9) is the distortion (or deform) of $u(x, t)$ from its stationary state centered at $z(t)$.

By substituting $u(x, t) = \bar{u}(x|z(t)) + \delta u(x, t)$ into Eq. (2.2), we have

$$\begin{aligned} \tau_s \frac{\partial u}{\partial t}(x, t) &= -\delta u(x, t) + \rho \int_{-\infty}^{\infty} dx' J(x, x') \int_{-\infty}^{\infty} dx'' \frac{\partial r(x')}{\partial u(x'')} \delta u(x'') + I^{\text{ext}}(x, t) \\ &= -\delta u(x, t) + \int_{-\infty}^{\infty} dx' \left[\int_{-\infty}^{\infty} dx'' \rho J(x, x'') \frac{\partial r(x'')}{\partial u(x')} \right] \delta u(x') + I^{\text{ext}}(x, t) \\ &= -\delta u(x, t) + \int_{-\infty}^{\infty} dx' F(x, x') \delta u(x') + I^{\text{ext}}(x, t), \end{aligned} \quad (2.10)$$

where $F(x, x')$ has the close form

$$\begin{aligned} F(x, x') &= \frac{2}{a\sqrt{\pi}} \exp\left[-\frac{(x-x')^2}{2a^2}\right] \exp\left[-\frac{(x'-z)^2}{a^2}\right] \\ &\quad - \frac{1 + \sqrt{1 - k/k_c}}{\sqrt{2\pi}a} \exp\left[-\frac{(x-z)^2}{4a^2}\right] \exp\left[-\frac{(x'-z)^2}{4a^2}\right]. \end{aligned} \quad (2.11)$$

In general, any families of orthonormal basis functions are applicable to be used to expand the dynamical variable $\delta u(x, t)$. Since the stationary state of the network is a Gaussian, we choose Hermite functions as basis functions. The n^{th} Hermite function is given by

$$\psi_n(x) = \frac{1}{\sqrt{\sqrt{2\pi}a2^n n!}} H_n\left(\frac{x}{\sqrt{2}a}\right) \exp\left(-\frac{x^2}{4a^2}\right), \quad (2.12)$$

where H_n is the n^{th} Hermite polynomial.

By using the orthogonality of basis functions and substituting Eq. (2.9) into Eq. (2.2), we can obtain differential equations of perturbative coefficients.

$$\begin{aligned} \left(\frac{d}{dt} + \frac{1 - \lambda_n}{\tau_s} \right) u_n(t) &= \frac{I_n(t)}{\tau_s} - \left(\bar{u}_0 \sqrt{\sqrt{2\pi}a} \delta_{n1} + \sqrt{n} u_n(t) - \sqrt{n+1} u_{n+1}(t) \right) \frac{1}{2a} \frac{dz}{dt} \\ &\quad + \frac{1}{\tau_s} \sum_{r=1}^{\infty} \sqrt{\frac{(n+2r)!}{n!}} \frac{(-1)^r}{2^{n+3r-1} r!} u_{n+2r}(t), \end{aligned} \quad (2.13)$$

where $I_n(t) \equiv \int dx I^{\text{ext}}(x, t)\psi_n(x|z(t))$. λ_n is the n^{th} eigenvalue of Eq. (2.11) given by

$$\lambda_n = \begin{cases} 1 - \sqrt{1 - k/k_c} & , n = 0 \\ 2^{1-n} & , n > 0 \end{cases} \quad (2.14)$$

Since $\lambda_n \leq 1$, stationary states of the neural network are stable for $dz/dt \approx 0$. In particular, eigenvalue for $n = 1$ is zero, which corresponds to eigenmode

$$\langle x | n = 1 \rangle = \frac{1}{\sqrt{2\sqrt{2\pi}a}} \frac{x}{\sqrt{2a}} \exp\left(-\frac{|x - z|^2}{4a^2}\right). \quad (2.15)$$

This eigenmode is the mode of translation. This is consistent with the fact that translationally invariant $J(x, x')$ enables translations of attractor states.

Based on the expansion of $\delta u(x, t)$, one can define an effective energy function and consider the dynamics in the energy landscape in Figure 2.2. Let us consider

$$E = \frac{1}{2} \sum_n (1 - \lambda_n) \langle n | \delta u \rangle^2, \quad (2.16)$$

where $\langle n |$ is the left eigenmode of F with eigenvalue λ_n . By using gradient descent, we have

$$\Delta \langle n | \delta u \rangle (t) = -\frac{\partial E}{\partial \langle n | \delta u \rangle} = -(1 - \lambda_n) \langle n | \delta u \rangle. \quad (2.17)$$

If we assume the time interval for each iteration to update $\langle n | \delta u \rangle$ is τ_s , we have

$$\tau_s \frac{d \langle n | \delta u \rangle}{dt} \approx -(1 - \lambda_n) \langle n | \delta u \rangle, \quad (2.18)$$

which is consistent with Eq. (2.13). Of course, here, the basis is $|n\rangle$, the right eigenmode of F with eigenvalue λ_n , not ψ_n . We remark that the effective energy in Eq. (2.16) is only introduced to describe the local dynamics of the system and for easier visualization; in practice the dynamics does not have a Lyapunov function [14].

The tracking speed can also be predicted by this perturbative method. Together with the self-consistent condition for the center of mass of the bump,

$$z = \frac{\int dx u(x, t) x}{\int dx u(x, t)}, \quad (2.19)$$

we have

$$\frac{dz}{dt} = \frac{2a}{\tau_s} \frac{I_1 + \sum_{n=3, \text{odd}}^{\infty} \sqrt{\frac{n!!}{(n-1)!!}} I_n + u_1}{\bar{u}_0 \sqrt{\sqrt{2\pi}a} + \sum_{n=0, \text{even}}^{\infty} \sqrt{\frac{(n-1)!!}{n!!}} u_n}. \quad (2.20)$$

Not only is the tracking speed predictable, but the temporal deformation of $u(x, t)$ can also be predicted. Figure 2.4 is the snapshot of $u(x, t)$ at different moments during the tracking process. In Figure 2.4, the stimulus changed from 0 to 2 at $t = 0$. During the first few τ_s , the network state is wider and shorter. However, once it becomes closer to the stimulus, the network state restores its original shape (dashed line), but at a different location. This whole behavior can be predicted by the perturbative analysis (solid line).

The number of terms to be included in a perturbative expansion should be the more the better. However, considering computational efficiency, less terms would be more favorable. The least number of terms to achieve good prediction depends on the asymmetry of the system about the center of mass of $u(x, t)$. For example, to analyze the motion of a bump tracking a stimulus jumped from 0 to $0.5a$, several small order terms already give good predictions. However, if the bump tracks a stimulus jumping from 0 to $5a$, higher order terms should be considered to include the higher order modes activated during the tracking process.

2.5 Summary

In this chapter, I have briefly reviewed the work on CANNs. The model we used can support a family of bump-shaped attractor network states. The internal dynamics of the network makes the attractors stable. However, due to the translational invariance of the coupling function, the network state can track along the attractor space smoothly. The network state can change under the influence of the external input.

To analyze this system, we use the perturbative method to decompose the distortion of $u(x, t)$. By using the perturbative method, the tracking speed of the network state can be derived. Also, the evolution of $u(x, t)$ can be predicted. The perturbative method also enable us to analyze two-dimensional (2D) CANN [22]. In the next chapter, I will review our work on CANNs with short-term synaptic depression (STD). We will also use perturbative method to analyze the dynamics of $u(x, t)$.

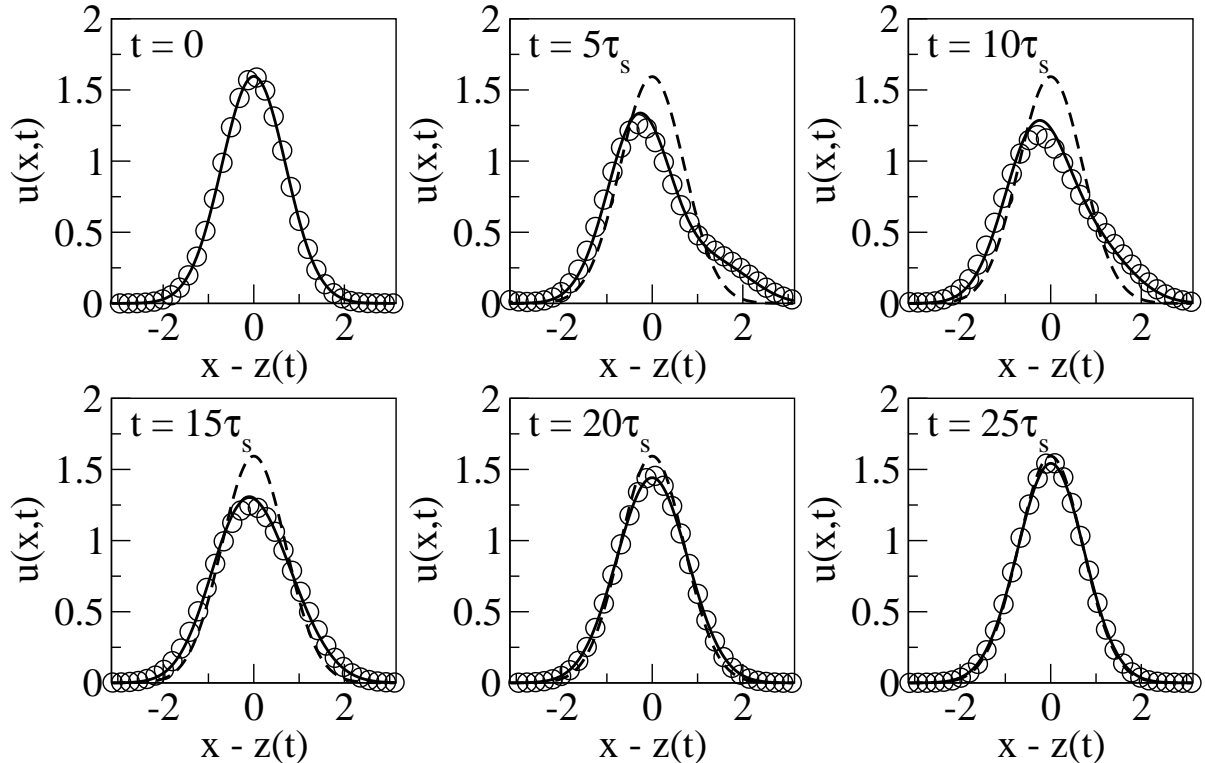


Figure 2.4: Snapshots of the neuronal inputs in the center-of-mass frame of the bump. Final position of the abrupt-change stimulus is 2.0. Symbols: simulations. Solid lines: predicted synaptic input with the $n = 10$ perturbation (expand $u(x,t)$ up to $n = 10$). Dashed lines: synaptic input at $t = 0$. Parameters: $A/\bar{u}_0 = 0.15$, $a = 0.5$, $k = 0.5$, $\rho = 200/(2\pi)$ and $J_0 = \sqrt{2\pi}a$.

Chapter 3

Review: Continuous Attractor Neural Networks with Synaptic Depression

3.1 Introduction

In the previous chapter, I have reviewed our work on continuous attractor neural networks (CANNs). In a CANN, there is a family of bump-shaped attractor states. The internal dynamics of the network can support bump-shaped attractor states. In this chapter, I will review our work on CANNs with short-term synaptic depression [23, 24].

In an experiment on neurons taken from the somatosensory cortical area of Wistar rats, the excitatory postsynaptic current after a spike of a presynaptic neuron depends on the firing history of the presynaptic neuron [25]. The synaptic efficacy decreases significantly if the presynaptic neuron was active for a long time. In the model proposed by Tsodyks *et al.* in 2008, the decrease in synaptic efficacy is due to the consumption of neurotransmitters. This reduction of synaptic efficacy is called short-term synaptic depression (STD). However, spikes of neurons may cause the opening of more calcium channels. The more calcium channels, the easier neurotransmitters can be released. The increase in the probability of releasing neurotransmitters is called short-term synaptic facilitation (STF). These two effects are components of short-term synaptic plasticity (STP). Strengths of these effects are determined by the physical condition of the neuron. Although the depletion of extracellular calcium ion level may also cause STD [26], results obtained from our simplified model should still apply, at least qualitatively, because the differential equations we used in our model is not for a particular biological process at the qualitative level.

3.2 The Model

The dynamics of $u(x, t)$ is similar to Eq. (2.2).

$$\tau_s \frac{du}{dt} (x, t) = -u (x, t) + \rho \int dx' J (x, x') p (x', t) r (x', t) + I^{\text{ext}} (x, t) \quad (3.1)$$

Here, τ_s is the time scale of $u(x, t)$. ρ is the density of neurons on the space. $I^{\text{ext}}(x, t)$ is an external input of the neural network. $r(x, t)$ and $J(x, x')$ are defined in Eqs. (2.1) and (2.3). We interpret $p(x, t)$ as the available fraction of the presynaptic neurotransmitters. It depends on the activity history of the presynaptic neuron [2, 24].

$$\tau_d \frac{dp}{dt} (x, t) = 1 - p (x, t) - \tau_d \beta p (x, t) r (x, t) \quad (3.2)$$

τ_d is the time constant of the recovery of neurotransmitters. β is the parameter corresponding to the strength of STD. The first two terms correspond to the dynamics of recovery of neurotransmitters. The last term is the rate of consumption of neurotransmitters. The effect of short-term synaptic depression is illustrated in Figure 3.1.

If we set $dp/dt = 0$ at the steady state,

$$p (x, t) = \frac{1}{1 + \tau_d \beta r (x, t)}. \quad (3.3)$$

If $r(x, t)$ is large, $p(x, t)$ will be smaller. $p(x, t)$ should be within $(0, 1]$. For $\tau_d \beta / (\rho^2 J_0^2)$ is small,

$$p (x, t) \approx 1 - \tau_d \beta r (x, t). \quad (3.4)$$

3.2.1 Rescaling of Parameters and Variables

From Eq. (3.1), we can see that $u(x, t)$ has a dimension $1/(\rho J_0)$. In order to gain the advantage of handling dimensionless variables, we study $\tilde{u}(x, t) \equiv \rho J_0 u(x, t)$ instead of $u(x, t)$. Similarly, $r(x, t)$ scales as $\rho^2 J_0^2$. We define $\tilde{r}(x, t) \equiv \rho^2 J_0^2 r(x, t)$. Parameters k and β can be rescaled by $\tilde{k} \equiv k/k_c$ and $\tilde{\beta} \equiv \tau_d \beta / (\rho^2 J_0^2)$. The rescaled version of Eqs. (3.1) and (3.2) are

$$\tau_s \frac{d\tilde{u}}{dt} (x, t) = -\tilde{u} (x, t) + \int dx' \tilde{J} (x, x') p (x', t) \tilde{r} (x', t) + \tilde{I}^{\text{ext}} (x, t) \quad (3.5)$$

$$\tau_d \frac{dp}{dt} (x, t) = 1 - p (x, t) - \tilde{\beta} p (x, t) \tilde{r} (x, t), \quad (3.6)$$

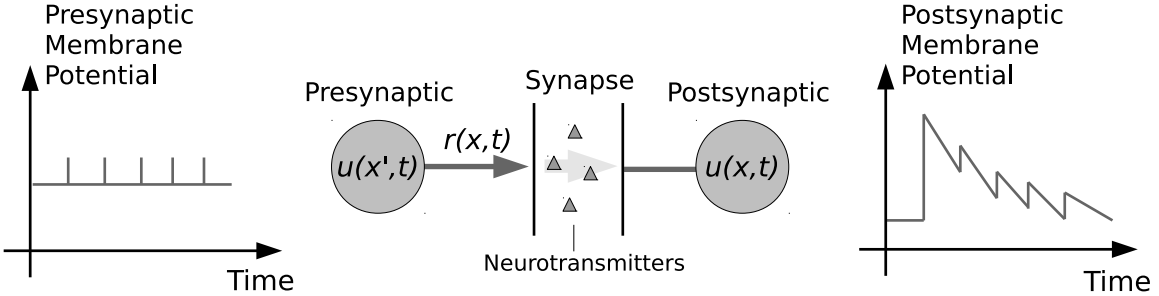


Figure 3.1: Action potentials, or spikes, on the presynaptic side cause releases of neurotransmitters, represented by triangles. Neurotransmitters diffuse to the terminal of the postsynaptic neuron. Neurotransmitters cause openings of ion channels of the postsynaptic neuron. Openings of ion channels can change the membrane potential of the postsynaptic neuron. However, since the recovery time of neurotransmitters is longer than the dynamics of the membrane potential and synaptic current, the synaptic efficacy would be reduced. The reduction of synaptic efficacy is called short-term synaptic depression.

where $\tilde{J}(x, x') \equiv \exp[-|x - x'|^2/(2a^2)]/\sqrt{2\pi a^2}$ and $\tilde{I}^{\text{ext}}(x, t) \equiv \rho J_0 I^{\text{ext}}(x, t)$.

3.3 Intrinsic Dynamics of Continuous Attractor Neural Networks with Short-term Synaptic Depression

In 2010, we reported the intrinsic dynamics of network states of CANNs with short-term synaptic depression [23] (more analysis in [24]). The intrinsic dynamics of the network refers to the natural behavior of the network state without any sustained external input.

For $\tilde{\beta}$ is small, the behavior of network states is very similar to that with $\tilde{\beta} = 0$. As shown in Figure 3.2(a), the steady state of the dynamical variable $\tilde{u}(x, t)$ will be stationary. However, if $\tilde{\beta}$ is larger, the network state will be a spontaneously moving profile, as shown in Figure 3.2(b). In the figure, the Gaussian-like $\tilde{u}(x, t)$ profile moves in the positive- x direction. Similar behavior can be found in other recurrent neural models [27].

Figure 3.3 shows how $\tilde{u}(x, t)$ and $p(x, t)$ generate the spontaneous motion. In Figure 3.3(a), $\tilde{\beta}$ is small such that the steady state of $\tilde{u}(x, t)$ is stationary and symmetric. If $\tilde{\beta}$ is larger, spontaneous motion begins to happen. In Figure 3.3(b), the profile $u(x, t)$ moves along the x direction slowly. The profile of $u(x, t)$ is almost symmetric. However, because the $u(x, t)$ moves to the right, the slowly evolving $p(x, t)$ profile lags behind. Since the net synaptic efficacy $J(x, x')p(x', t)$ is asymmetric, the $u(x, t)$ moves forward due to the

recurrent connection. If $\tilde{\beta}$ is even larger, the speed of a spontaneously moving profile of $\tilde{u}(x, t)$ will be faster. As shown in Figure 3.3(c), even though $\tilde{u}(x, t)$ is still almost symmetric, the slow dynamics of $p(x, t)$ makes $p(x, t)$ asymmetric about the center of mass of $\tilde{u}(x, t)$. An illustration of the moving profile is shown in Figure 3.4. The motion of $\tilde{u}(x, t)$ makes $p(x, t)$ asymmetric. As a result, the suppression effect on $\tilde{u}(x, t)$ due to STD is asymmetric about the center of mass of $\tilde{u}(x, t)$. The side of $\tilde{u}(x, t)$ trailing the motion experiences a stronger suppressional effect. On the other hand, the abundance of neurotransmitters on the leading side of the bump increases the likelihood of the neurons there to fire. Since the amplitude stability maintains the shape of $\tilde{u}(x, t)$, the profile of $\tilde{u}(x, t)$ shifts to a region with larger $p(x, t)$. So, the motion of $\tilde{u}(x, t)$ can sustain, i.e. the bump can move spontaneously. Experimental evidence of the existence of spontaneous moving bumps can be found in the primary visual cortex [28]. STD should provide at least part of the contribution of the spontaneous motion, because STD should be commonly found in chemical synapses.

There are parameter regions for different phases. There are four phases: static, moving, metastatic and silent. In Figure 3.5, there are boundaries figuring out parameter regions for different phases. At the bottom of the plot, there is a parameter region called ‘static’. In this region, the network cannot support spontaneous motion of $u(x, t)$ e.g. Figure 3.2(a). In the middle-top region of Figure 3.5, there is a region, called ‘moving’, that the network supports only spontaneously moving $u(x, t)$ profile. Between static phase and moving phase, there is a region named ‘metastatic or moving’. In this region, the network can support either stationary or moving $u(x, t)$. However, within this parameter region, stationary $u(x, t)$ ’s are translationally unstable. It means that, if there is an asymmetric distortion on the stationary $u(x, t)$, the stationary $u(x, t)$ will move and become a spontaneously moving profile. When $\tilde{\beta}$ and \tilde{k} are large, only the trivial solution is stable. The region with only trivial solution is the ‘silent’ phase.

3.4 Perturbation on Continuous Attractor Neural Networks with Short-term Synaptic Depression

To analyze behaviors of bump-shaped network states, we proposed a perturbative method to decompose the distortions of $\tilde{u}(x, t)$ and $p(x, t)$. The perturbative method is similar to that mentioned in Chapter 2. Here is the small parameter is $\tilde{\beta}$. Since the fixed point

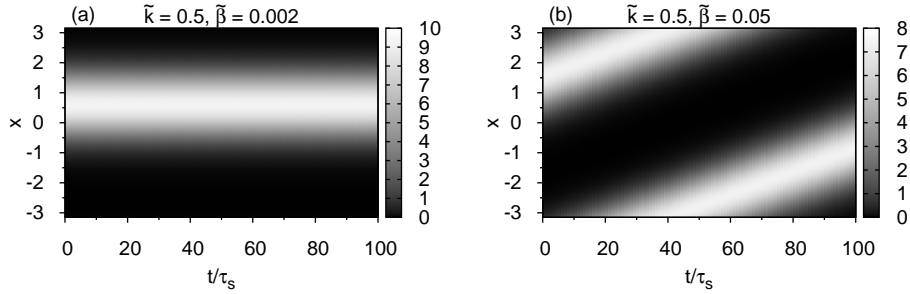


Figure 3.2: Raster plots of $\tilde{u}(x, t)$ for two sets of parameters and without an external input ($\tilde{I}^{\text{ext}} = 0$). Parameters are labeled at the top of each plot. (a) $\tilde{\beta}$ is too small to support spontaneously moving profile of $\tilde{u}(x, t)$. (b) $\tilde{\beta}$ is large enough to support spontaneous motions.

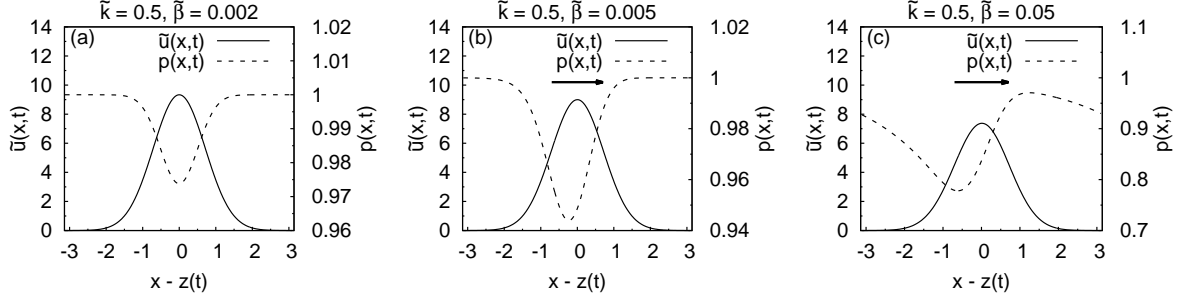


Figure 3.3: Snapshots of profiles of $\tilde{u}(x, t)$ and $p(x, t)$ for various sets of parameters and without an external input ($\tilde{I}^{\text{ext}} = 0$) as functions of preferred stimulus relative to the center of mass of $\tilde{u}(x, t)$. Parameters are labeled at the top of each plot. (a) $\tilde{u}(x, t)$ and $p(x, t)$ are symmetric. $\tilde{u}(x, t)$ will not move spontaneously. (b) $p(x, t)$ is slightly asymmetric. $\tilde{u}(x, t)$ moves slowly due to the asymmetry of $p(x, t)$. (c) $p(x, t)$ is highly asymmetric due to the fast motion of $\tilde{u}(x, t)$, while $\tilde{u}(x, t)$ moves quickly due to the asymmetric synaptic efficacy.

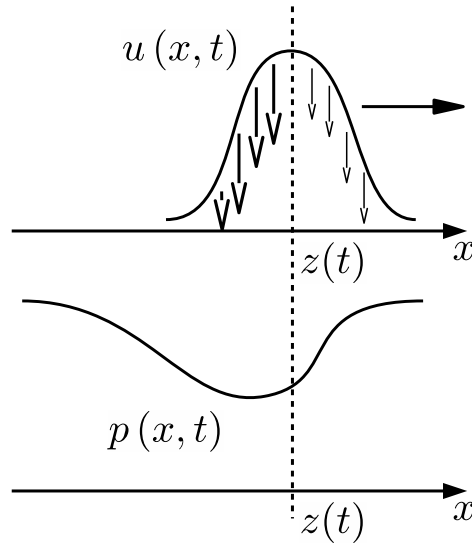


Figure 3.4: Illustration of how the asymmetric $p(x, t)$ sustains the motion of bump-shaped profile of $u(x, t)$. The motion of $u(x, t)$, labeled by the arrow, can make the profile of $p(x, t)$ asymmetric about the center of mass of $u(x, t)$. However, since $p(x, t)$ is asymmetric, the suppression effect on $u(x, t)$ due to $p(x, t)$ is asymmetric. In addition to the local excitation of the CANN, the $u(x, t)$ profile travels to the area with larger $p(x, t)$. As a result, the motion can sustain.

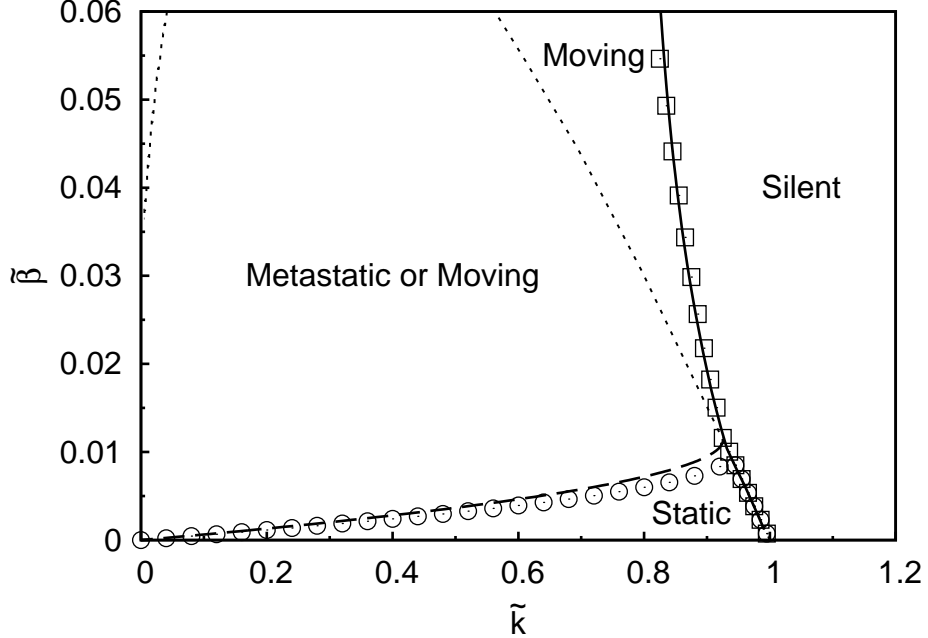


Figure 3.5: The phase diagram for a CANN with STD. Parameter: $\tau_d/\tau_s = 50$.

solution of Eq. (3.1) is close to a Gaussian bump with width $\sqrt{8}a$, we let

$$\tilde{u}(x, t) = \tilde{u}_0 \exp\left(-\frac{x^2}{4a^2}\right). \quad (3.7)$$

The variable $p(x, t)$ is expanded as

$$p(x, t) = 1 - \sum_n p_n(t) \varphi_n(x - z(t)), \quad (3.8)$$

where $\varphi_n(x)$'s are different n^{th} order Hermite functions defined by

$$\varphi_n = \frac{1}{\sqrt{\sqrt{\pi}a^{2n}n!}} H_n\left(\frac{x}{a}\right) \exp\left(-\frac{x^2}{2a^2}\right), \quad (3.9)$$

and $H_n(x)$ is the n^{th} order physicist's Hermite polynomial. Here, we choose the basis with φ_0 having a width $2a$ to make the convergence of the expansion faster, because $p(x, t)$ is driven by $r(x, t)$, see Eq. (3.3). For n up to 0 and $I^{\text{ext}} = 0$, by substituting Eqs. (3.7) and (3.8) into Eqs. (3.5) and (3.6) and projecting both sides of two differential

equations on appropriate Hermite functions, we have

$$\tau_s \frac{d\tilde{u}_0}{dt} = \frac{1}{\sqrt{2}} \frac{\tilde{u}_0^2}{1 + \tilde{k}\tilde{u}_0^2/8} \left(1 - \sqrt{\frac{4}{7}} \frac{p_0}{\sqrt{\sqrt{\pi}a}} \right) - \tilde{u}_0 \quad (3.10)$$

$$\tau_d \frac{dp_0}{dt} = \frac{\tilde{\beta}\tilde{u}_0^2}{1 + \tilde{k}\tilde{u}_0^2/8} \left(\sqrt{\sqrt{\pi}a} - \sqrt{\frac{2}{3}}p_0 \right) - p_0 \quad (3.11)$$

By studying the fixed point solution and its stability, we can obtain the dotted line in Figure 3.5, which is the boundary for the static network state to have stable amplitudes.

To test the translational stability, we need to consider \tilde{u}_n and p_n up to at least $n = 1$. For static network states, p_1 is zero. By studying the stability of solutions with p_1 and nonzero \tilde{u}_0 and p_0 (\tilde{u}_1 can be set to zero by a shift of the origin.), we can map the region stable static network states (dashed line in Figure 3.5) out of the region for only amplitude stability.

For stable solutions of spontaneously moving $u(x, t)$, we need to consider higher order p_n . As we can see in Figure 3.3(c), if $\tilde{\beta}$ is large, $p(x, t)$ will be highly asymmetric about the center of mass of $u(x, t)$. In these cases, higher order expansion of $p(x, t)$ is required to obtain accurate boundary for spontaneously moving $u(x, t)$. For example, in Figure 3.5, the predicted phase boundary separating silent phase and moving phase was done by $n = 11$ perturbation, i.e. expanding $u(x, t)$ and $p(x, t)$ up to $n = 11$.

3.5 Summary

In this chapter, I have briefly reviewed our work on CANN with STD. Under the influence of STD, the network may behave differently, depending on degrees of STD and divisive global inhibition. Spontaneous motions can also be found in other models with STD, e.g. [27]. CANN with feedback modulations can also achieve similar spontaneous behavior [29].

During the study of CANN with STD, we attempted to analyze the model using perturbative method. Although the approximation of $u(x, t)$ is not precise, the prediction on the phase diagram is fairly good. In this next chapter, I will present the work with perturbative expansions on $u(x, t)$. Also, we analyzed CANN with short-term synaptic facilitation. The intrinsic dynamics of CANN with STD can also modulate the tracking behavior.

Chapter 4

Continuous Attractor Neural Networks with Synaptic Plasticity

4.1 Introduction

Our work on continuous attractor neural networks (CANNs) with short-term synaptic depression (STD) is briefly reviewed in the previous chapter. However, based on the theory by Tsodyks *et al.*, action potentials of presynaptic neurons may also induce short-term synaptic facilitation (STF), which can enhance the synaptic efficacy between presynaptic and postsynaptic neurons.

Here, I present a CANN model with both STF and STD. In the previous chapter, in CANN with STD, I have shown that the expansion of $p(x, t)$ (available portion of neurotransmitters of presynaptic neurons at preferred stimuli x and time t) can predict the phase diagram and occurrence of intrinsic motions. In this chapter, I will present further analytic work on CANN with STD using expansions of $u(x, t)$ (synaptic current of neurons at preferred stimuli x and time t) and $p(x, t)$.

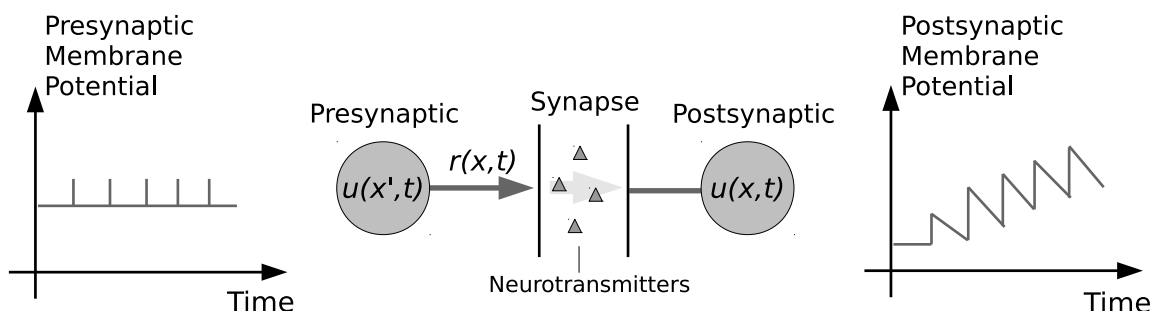


Figure 4.1: An illustration of short-term synaptic facilitation. Release of neurotransmitters increase the calcium level of the presynaptic neuron. The rise of calcium level increases the possibility of neurotransmitters for the next action potential. As a result, the synaptic efficacy get strengthened.

For CANNs with STF, the perturbative approach is also applicable. After some analyses and some simulations, we found that STF can stabilize network states, which is qualitatively opposite to the effect of STD. Due to the extra stability provided by STF, CANNs with STF can reduce the noise mixed with the external input significantly. We have also found that the phase diagram for a model of CANNs with STF.

4.2 The Model

Similar to Eqs. (2.2) and (3.1), we model the dynamics of the network through the synaptic current of neurons, $u(x, t)$:

$$\tau_s \frac{du}{dt}(x, t) = -u(x, t) + \rho \int dx' J(x, x') [1 + f(x', t)] p(x', t) r(x', t) + I^{\text{ext}}(x, t). \quad (4.1)$$

τ_s is the time constant of $u(x, t)$ of the order of magnitude of 1 ms. ρ is the density of neurons over the space $\{x\}$. $r(x, t)$ is the neuronal activity of neurons at x and time t , given by Eq. (2.1). $J(x, x')$ is the excitatory coupling between neurons at x and x' , given by Eq. (2.3). $I^{\text{ext}}(x, t)$ is the external input to neurons at x and time t . $p(x, t)$ models the available fraction of neurotransmitters, which is between 0 and 1. Its dynamics is governed by

$$\tau_d \frac{dp}{dt} = 1 - p(x, t) - \tau_d \beta [1 + f(x, t)] p(x, t) r(x, t). \quad (4.2)$$

τ_d is the time constant of $p(x, t)$ of the order of magnitude of 100 ms. β is the strength of STD. The illustration of STD is shown in Figure 3.1. $f(x, t)$ models the enhancement of synaptic efficacy due to neuronal activities. Its dynamics is given by

$$\tau_f \frac{df}{dt}(x, t) = -f(x, t) + \tau_f \alpha [f_{\max} - f(x, t)] r(x, t). \quad (4.3)$$

τ_f is the time constant of $f(x, t)$ ranging from 100 ms to several seconds. α is the strength of STF. The illustration of STF is shown in Figure 4.1. Like Figure 3.1, action potentials trigger release of neurotransmitters. During the process, the calcium level of the presynaptic neuron increases. The higher calcium level it is, the higher release probability of neurotransmitters it would be. So, the synaptic efficacy is strengthened due to the rise of calcium level. It can be shown that this model is consistent with the model of dynamical synapses proposed by Tsodyks *et al.* [2].

4.3 General Perturbative Expansions on Dynamical Variables

Similar to the rescaling rule in subsection 3.2.1, since $u(x, t)$ has a unit ρJ_0 and $r(x, t)$ has a unit $\rho^2 J_0^2$, we introduce the rescaled variables for $u(x, t)$ and $r(x, t)$ according to

$$\tilde{u}(x, t) \equiv \rho J_0 u(x, t), \quad \tilde{r}(x, t) \equiv \rho^2 J_0^2 r(x, t) \quad (4.4)$$

Accordingly, we rescale parameters by

$$\tilde{k} \equiv \frac{\rho J_0^2}{8\sqrt{2\pi}a} k, \quad \tilde{\beta} \equiv \frac{\tau_d \beta}{\rho^2 J_0^2}, \quad \tilde{\alpha} \equiv \frac{\tau_f \alpha}{\rho^2 J_0^2}. \quad (4.5)$$

Therefore, the rescaled differential equations are

$$\tau_s \frac{d\tilde{u}}{dt}(x, t) = -\tilde{u}(x, t) + \int dx' \tilde{J}(x, x') [1 + f(x', t)] p(x', t) \tilde{r}(x', t) + \tilde{I}^{\text{ext}}(x, t) \quad (4.6)$$

$$\tau_d \frac{dp}{dt}(x, t) = 1 - p(x, t) - \tilde{\beta} [1 + f(x, t)] p(x, t) \tilde{r}(x, t) \quad (4.7)$$

$$\tau_f \frac{df}{dt}(x, t) = -f(x, t) + \tilde{\alpha} [f_{\max} - f(x, t)] \tilde{r}(x, t), \quad (4.8)$$

where $\tilde{J}(x, x')$ is the rescaled excitatory coupling given by

$$\tilde{J}(x, x') \equiv \frac{1}{\sqrt{2\pi}a} \exp\left(-\frac{|x - x'|^2}{2a^2}\right), \quad (4.9)$$

and $\tilde{I}^{\text{ext}}(x, t)$ is the rescaled external input given by

$$\tilde{I}^{\text{ext}}(x, t) = \tilde{A} \exp\left(-\frac{|x - z_0(t)|^2}{4a^2}\right). \quad (4.10)$$

Consider expansions of $u(x, t)$, $p(x, t)$ and $f(x, t)$.

$$\tilde{u}(x, t) = \sum_k \tilde{u}_k(t) \psi_k(x - z(t)) \quad (4.11)$$

$$p(x, t) = 1 - \sum_k p_k(t) \varphi_k(x - z(t)) \quad (4.12)$$

$$f(x, t) = \sum_k f_k(t) \varphi_k(x - z(t)), \quad (4.13)$$

where

$$\psi_n(x) = \frac{1}{\sqrt{\sqrt{2\pi}a2^n n!}} H_n\left(\frac{x}{\sqrt{2}a}\right) \exp\left(-\frac{x^2}{4a^2}\right) \quad (4.14)$$

$$\varphi_n(x) = \frac{1}{\sqrt{\sqrt{\pi}a2^n n!}} H_n\left(\frac{x}{a}\right) \exp\left(-\frac{x^2}{2a^2}\right) \quad (4.15)$$

$$z(t) = \frac{\int dx x \tilde{u}(x, t)}{\int dx \tilde{u}(x, t)}, \quad (4.16)$$

H_n is the n^{th} order physicist's Hermite polynomial and \tilde{u}_k , p_k and f_k are perturbative variables. $z(t)$ is chosen to be the center of mass of $\tilde{u}(x, t)$. Note that, expansions of $\tilde{u}(x, t)$, $p(x, t)$ and $f(x, t)$ are different, because $p(x, t)$ and $f(x, t)$ are driven by $r(x, t)$. So, basis to expand $p(x, t)$ and $f(x, t)$ is chosen to have φ_0 having width $2a$ to make the convergence faster.

Continuous attractor neural networks with STD and STF is too complicated. Here, we study STD and STF separately. For $\tilde{\alpha} = 0$, since ψ_n and φ_n are orthogonal to their family members, Eqs. (4.6) and (4.7) become

$$\begin{aligned} & \tau_s \left[\frac{d\tilde{u}_k}{dt} - \frac{\dot{z}}{2a} (\sqrt{k+1}\tilde{u}_{k+1} - \sqrt{k}\tilde{u}_{k-1}) \right] \\ &= -\tilde{u}_k + \frac{1}{B} \left(\sum_{nm} C_{nm}^k \tilde{u}_n \tilde{u}_m - \sum_{nml} D_{nml}^k \tilde{u}_n \tilde{u}_m p_l \right) + \tilde{I}_k \end{aligned} \quad (4.17)$$

$$\begin{aligned} & \tau_d \left[\frac{dp_k}{dt} - \frac{\dot{z}}{\sqrt{2}a} (\sqrt{k+1}p_{k+1} - \sqrt{k}p_{k-1}) \right] \\ &= -p_k + \frac{\tilde{\beta}}{B} \left(\sum_{nm} E_{nm}^k \tilde{u}_n \tilde{u}_m - \sum_{nml} F_{nml}^k \tilde{u}_n \tilde{u}_m p_l \right) \end{aligned} \quad (4.18)$$

C_{nm}^k , D_{nml}^k , E_{nm}^k and F_{nml}^k are defined by

$$C_{nm}^k = \int dx \psi_k(x) \int dx' \tilde{J}(x, x') \psi_n(x') \psi_m(x') \quad (4.19)$$

$$D_{nml}^k = \int dx \psi_k(x) \int dx' \tilde{J}(x, x') \psi_n(x') \psi_m(x') \varphi_l(x') \quad (4.20)$$

$$E_{nm}^k = \int dx \varphi_k(x) \psi_n(x) \psi_m(x) \quad (4.21)$$

$$F_{nml}^k = \int dx \psi_k(x) \psi_n(x) \psi_m(x) \varphi_l(x) \quad (4.22)$$

C_{00}^0 , D_{000}^0 , E_{00}^0 and F_{000}^0 can be calculated explicitly, while C_{nm}^k , D_{nml}^k , E_{nm}^k and F_{nml}^k

can be determined by iterative rules in Appendix B. For the choice of the external input defined in Eq. (4.10),

$$\tilde{I}_k = \int dx \psi(x - z(t)) \tilde{I}^{\text{ext}}(x, t) \quad (4.23)$$

$$= \tilde{A} \sqrt{\frac{\sqrt{2\pi}a}{k!}} \left(\frac{z_0 - z}{2a} \right)^k \exp \left(-\frac{|z(t) - z_0(t)|^2}{8a^2} \right) \quad (4.24)$$

For $\tilde{\beta} = 0$,

$$\begin{aligned} & \tau_s \left[\frac{d\tilde{u}_k}{dt} - \frac{\dot{z}}{2a} \left(\sqrt{k+1}\tilde{u}_{k+1} - \sqrt{k}\tilde{u}_{k-1} \right) \right] \\ &= -\tilde{u}_k + \frac{1}{B} \left(\sum_{nm} C_{nm}^k \tilde{u}_n \tilde{u}_m + \sum_{nml} D_{nml}^k \tilde{u}_n \tilde{u}_m f_l \right) + \tilde{I}_k \end{aligned} \quad (4.25)$$

$$\begin{aligned} & \tau_d \left[\frac{df_k}{dt} - \frac{\dot{z}}{\sqrt{2}a} \left(\sqrt{k+1}f_{k+1} - \sqrt{k}f_{k-1} \right) \right] \\ &= -f_k + \frac{\tilde{\alpha}}{B} \left(f_{\max} \sum_{nm} E_{nm}^k \tilde{u}_n \tilde{u}_m - \sum_{nml} F_{nml}^k \tilde{u}_n \tilde{u}_m f_l \right) \end{aligned} \quad (4.26)$$

Including more perturbative variables should improve the prediction. In Figure 4.2, there is a comparison between simulations and predictions. In (a) and (b), circles and squares correspond to different initial conditions (A and B). For initial condition A, $\tilde{u}(x, t)$ and $p(x, t)$ are set to be a fixed point solution of Eqs. (4.6) and (4.7) with $\tilde{\beta} = 0$. This initial condition corresponds to the scenario that the stimulus appears for a very short period such that $p(x, t)$ is effectively 1 right after the withdraw of the stimulus. Initial condition B corresponds to scenario that the stimulus has appeared for a long period until $t = 0$ such that the network state was steady before $t = 0$. Dashed lines are predictions by the second order p -perturbation, i.e. keeping only \tilde{u}_0 and p_n 's up to $n = 2$. Solid lines are predictions by full perturbation, i.e. considering \tilde{u}_n 's and p_n 's up to $n = 2$. In Figure 4.2, both p -perturbation and full perturbation work well with the simulation result for initial condition B. However, for initial condition A, p -perturbation works well for only first about $120\tau_s$, full perturbation still work well for the whole decay process. It suggests that, in some cases, p -perturbation is good for prediction, but full-perturbation should be applicable for more cases. Full perturbation improves the transient phenomenon of dynamical variables, but p -perturbation can predict the occurrence of terminal states well. So, p -perturbation can predict the phase diagram of

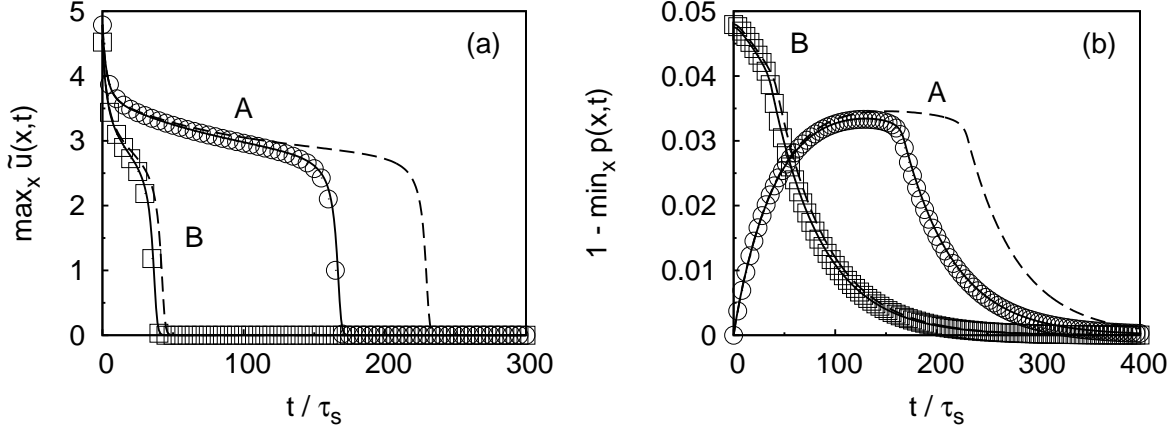


Figure 4.2: Plateau states of the network with different initial condition (A and B). (a) $\tilde{u}(x,t)$ and (b) $1 - p(x,t)$ are presented. Squares: simulation with initial condition A. Circles: simulation with initial condition B. Dashed lines: prediction by second order p -perturbation. Solid lines: prediction by second order full perturbation. Parameters: $\tilde{k} = 0.95$, $\tilde{\beta} = 0.0085$ and $\tau_d/\tau_s = 50$.

CANNs with STD (Figure 3.5) well.

In Figure 4.2, the inclusion of \tilde{u}_2 is important, because the intrinsic dynamics of static bump in the certain parameter region is marginally unstable. Approximation of $\tilde{u}(x,t)$ including only \tilde{u}_0 has a small but significant difference such that the prediction of the transient of $\tilde{u}(x,t)$ would be inaccurate. One effect on $\tilde{u}(x,t)$ by STD is that the bump gets widened due to the modulation of synaptic efficacies around the bump. So, including \tilde{u}_2 can help the prediction. This is an example showing that the perturbative analysis can help to understand how different modes of distortions affect the dynamics of the system. Here, one can see that a change in width is an important effect during the decay process.

For a CANN without STD, once the bump is formed, the bump can sustain forever due to the local excitation. This behavior is unnatural, because the network activity should decay after a withdraw of a stimulus so that the network can accept a new stimulus. With STD, there is a parameter region such that the network can support the network state for a while after a withdraw of a stimulus. It makes the behavior of a CANN become more natural. The plateau state can also be account for sensory memory in the nervous system.

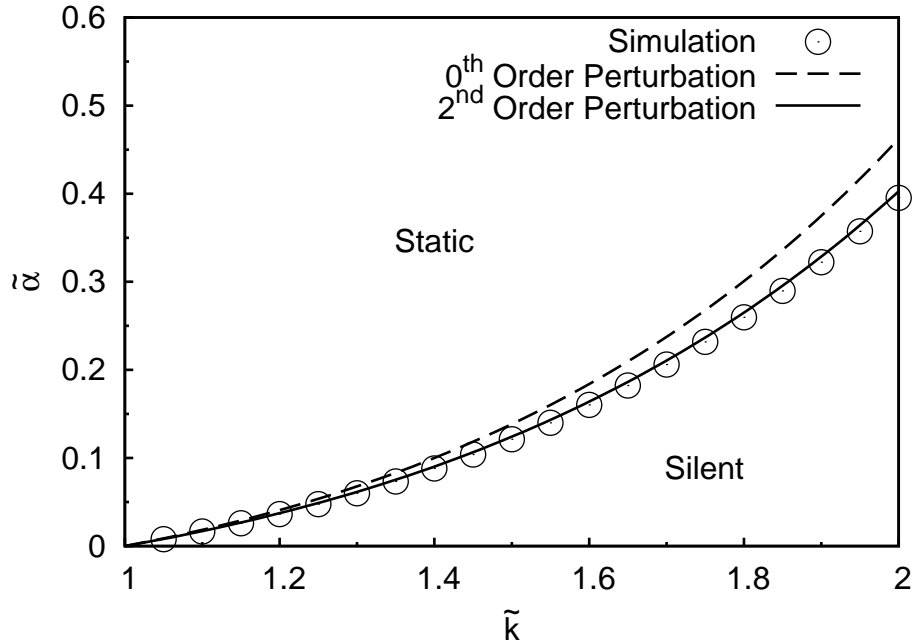


Figure 4.3: Phase diagram of CANNs with STF for $\tau_f/\tau_s = 50$ and $f_{\max} = 1$.

4.4 Intrinsic Dynamics of Continuous Attractor Neural Networks with Short-term Synaptic Facilitation

Comparing with short-term synaptic depression, short-term synaptic facilitation affects CANNs in a qualitatively opposite way. STD degrades the synaptic efficacy due to the firing history of presynaptic neurons, while STF can enhance the synaptic efficacy due to the past activities of the presynaptic neurons. It is expected that STF should stabilize static bump-shaped states of a CANN, because the localized network activity can enhance the effective coupling, $J(x, x')[1 + f(x, t)]$, locally. STF functions as a positive feedback. If there is a translational distortion, the positive feedback can pull the network activity profile back to its original position. So, there is no spontaneous motion on CANNs with STF.

Since there should be no spontaneous motion, we consider only amplitude stability of bump-shaped profile network states. The simplest way to analyze the amplitude

stability is to consider

$$\tilde{u}(x, t) \approx \tilde{u}_0(t) \exp\left(-\frac{x^2}{4a^2}\right) \quad (4.27)$$

$$f(x, t) \approx f_0(t) \exp\left(-\frac{x^2}{2a^2}\right) \quad (4.28)$$

Note that this simplest analysis is ‘0th order perturbation’. By projecting Eqs. (4.6) and (4.8) on $\exp[-x^2/(4a^2)]$ and $\exp[-x^2/(2a^2)]$, the fixed point solution to \tilde{u}_0 and f_0 can be solved by

$$\tilde{u}_0 = \frac{1}{\sqrt{2}} \frac{\tilde{u}_0^2}{B} \left(1 + \sqrt{\frac{4}{7}} f_0\right) \quad (4.29)$$

$$f_0 = \frac{\tilde{\alpha}}{B} \left(f_{\max} + \sqrt{\frac{2}{3}} f_0\right) \tilde{u}_0^2 \quad (4.30)$$

$$B \equiv 1 + \frac{1}{8} \tilde{k} \tilde{u}_0^2 \quad (4.31)$$

By studying the stability of the fixed point solution, we can obtain the parameter region for stable static profiles. In Figure 4.3, the dashed line is the boundary predicted by this simplest analysis. This is fairly fine. The discrepancy between this prediction and the simulation should be due to the distortion of $u(x, t)$ and $f(x, t)$. Since the synaptic efficacy is no longer homogeneous, the width of a $u(x, t)$ profile is narrower than $\sqrt{2}a$.

To improve the prediction, we consider

$$\tilde{u}(x, t) = \tilde{u}_0(t) \psi_0(x) + \tilde{u}_2(t) \psi_2(x) \quad (4.32)$$

$$f(x, t) = f_0(t) \varphi_0(x) + f_2(t) \varphi_2(x). \quad (4.33)$$

The fixed point solution can be determined numerically. By studying the stability of the fixed point solutions, we can determine the phase boundary between static phase and silent phase. In Figure 4.3, we can see that the prediction of the ‘2thorder perturbation’ can fit the measurement from simulations.

4.5 CANNs with STF as a Noise Filter

In the last chapter, I have argued that STF can make bump-shaped states on a CANN more stable in both amplitude and position. We can see its effect by looking at how STF broadens the parameter region for static network states as shown in Figure 4.3. The

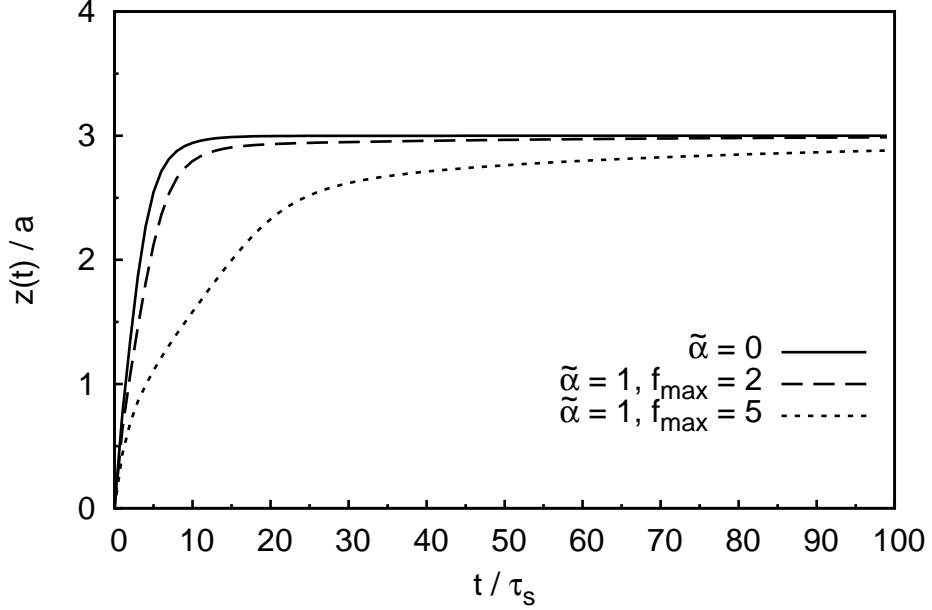


Figure 4.4: A plot of centers of mass of $\tilde{u}(x, t)$ as functions of t under various levels of STF. Other parameters: $\tilde{A} = 7.9788$, $\tau_f/\tau_s = 50$.

position stability enhanced by STF can also be seen in the tracking behavior. In Figure 4.4, the tracking dynamics can be slowed down by introducing STF.

Since STF tends to pin and resist the network state to move from its original position, it can be used as a noise filter. To study this property, we define

$$\tilde{I}^{\text{ext}}(x, t) = \tilde{A} \exp\left(-\frac{|x - z_0 - \eta(t)|^2}{4a^2}\right). \quad (4.34)$$

z_0 is the stimulus. $\eta(t)$ is a white noise satisfying

$$\langle \eta(t) \eta(t') \rangle = 2Ta^2\tau_s \delta(t - t'), \quad (4.35)$$

where T is the noise strength. Under the influence of this noisy external input, the center of mass of $\tilde{u}(x, t)$, $z(t)$, will fluctuate around z_0 . In Figure 4.5, $z_0 = 0$ and $T = 0.02$. Since the noises in both cases with different parameter sets are the same (by choosing the same random seed), we can easily compare how STF improve the performance against noise.

In Figure 4.5, the fluctuation of $z(t)$ without STF is significantly larger than that with STF. Because the synaptic efficacy near the region centered at z_0 is stronger than other regions. The internal dynamics of the network pull the network state back to the

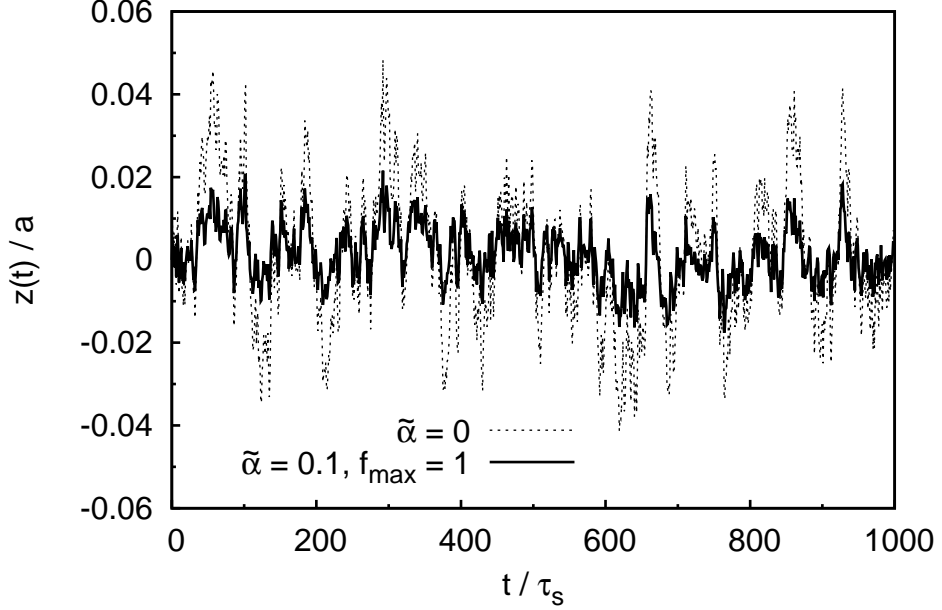


Figure 4.5: A comparison between CANNs with and without STF under the influence of a noisy external input. Dotted line: case without STF. Solid line: case with STF. Other parameters: $a = 0.5$, $x \in [-\pi, \pi]$, $\tilde{k} = 0.25$, $\rho = 80/(2\pi)$, $\tilde{A} = 1.596$ and $T = 0.02$.

center of the region with enhanced synaptic efficacy.

To analyze this behavior, let us consider

$$\tilde{u}(x, t) = \tilde{u}_0 \exp\left(-\frac{|x - z_0 - s(t)|^2}{4a^2}\right) \quad (4.36)$$

$$f(x, t) = f_0 \exp\left(-\frac{|x - z_0 - s(t)|^2}{2a^2}\right) + f_1\left(\frac{x - z_0 - s(t)}{a}\right) \exp\left(-\frac{|x - z_0 - s(t)|^2}{2a^2}\right) \quad (4.37)$$

Since the fluctuation is small compared with the tuning widths of the neurons, we assume that the changes in the height of the Gaussian functions are negligible. By substituting Eqs. (4.36) and (4.37) into Eqs. (4.6) and (4.8), we have

$$\tau_s \frac{d}{dt} \begin{pmatrix} \frac{s}{a} \\ \frac{f_1}{f_0} \end{pmatrix} = M \begin{pmatrix} \frac{s}{a} \\ \frac{f_1}{f_0} \end{pmatrix} + \frac{\tilde{A}}{\tilde{u}_0 a} \eta(t) \begin{pmatrix} 1 \\ -1 \end{pmatrix}, \quad (4.38)$$

where

$$M \equiv \begin{pmatrix} -\frac{\tilde{A}}{\tilde{u}_0} & \frac{2\tilde{u}_0 f_0}{B} \left(\frac{2}{7}\right)^{\frac{3}{2}} \\ \frac{\tilde{A}}{\tilde{u}_0} & -\left\{ \frac{2\tilde{u}_0 f_0}{B} \left(\frac{2}{7}\right)^{\frac{3}{2}} + \frac{\tau_s}{\tau_f} \left[1 + \frac{\tilde{\alpha} \tilde{u}_0^2}{B} \left(\frac{2}{3}\right)^{\frac{3}{2}} \right] \right\} \end{pmatrix}. \quad (4.39)$$

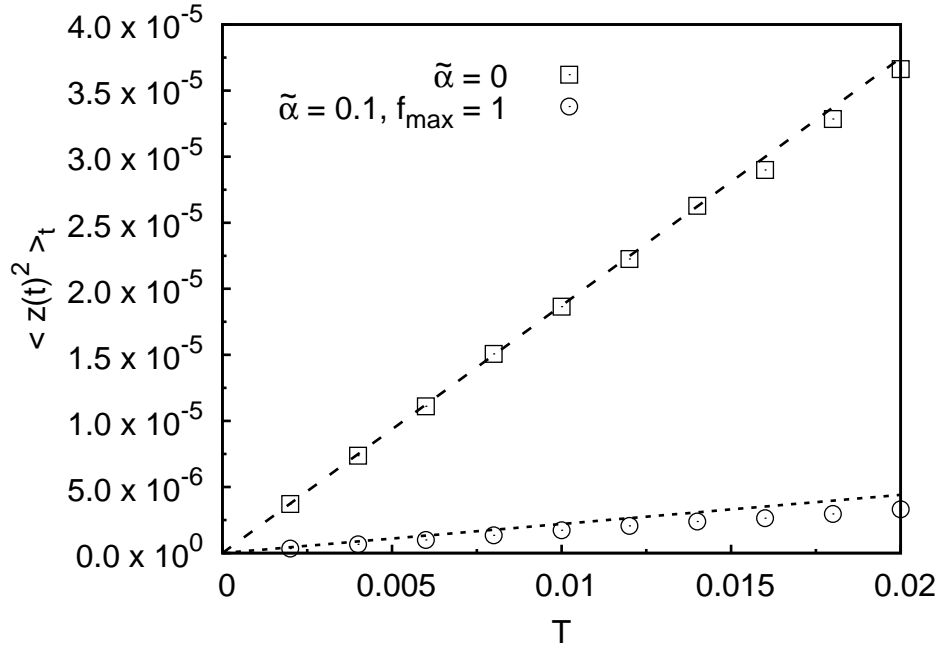


Figure 4.6: The decoding errors of the network versus different levels of noise. Parameters other than T are the same as those in Figure 4.5. Symbols: simulations. Dashed line: predictions for $\tilde{\alpha} = 0$. Dotted line: predictions for $\tilde{\alpha} = 0.1$.

This differential equation can be solved by first diagonalizing M . Let $-\lambda_{\pm}$ be the eigenvalues of M and $(U_{s\pm} U_{f\pm})^T$ be the corresponding eigenvectors. Then the solution becomes

$$\begin{pmatrix} \frac{s}{a} \\ \frac{f_1}{f_0} \end{pmatrix} = \frac{\tilde{A}}{\tilde{u}_0 a} \int_{-\infty}^t \frac{dt_1}{\tau_s} \eta(t_1) U \begin{pmatrix} E_+ & 0 \\ 0 & E_- \end{pmatrix} U^{-1} \begin{pmatrix} 1 \\ -1 \end{pmatrix}, \quad (4.40)$$

where $E_{\pm} = \exp[-\lambda_{\pm}(t - t_1)]$ and U is a transformation matrix. Squaring the expression of s/a , averaging over noise, and integrating, we obtain

$$\left\langle \left(\frac{s}{a} \right)^2 \right\rangle = 2T \left(\frac{\tilde{A}}{\tilde{u}_0} \right)^2 \sum_{a,b=\pm} [U_{sa} (U_{as}^{-1} - U_{af}^{-1})] \times \frac{1}{(\lambda_a + \lambda_b) \tau_s} [U_{sb} (U_{bs}^{-1} - U_{bf}^{-1})]. \quad (4.41)$$

The prediction can be determined numerically. The results for two sets of parameters (dashed line and dotted line) are shown in Figure 4.6 to compare with measurements from simulations. It shows that STF can reduce the effect from noise on the CANN. Also, this phenomenon can be explained by simple assumptions (Eqs. (4.36) and (4.37)).

4.6 Summary

In this chapter, I have shown the full perturbative expansion for $\tilde{u}(x, t)$, $p(x, t)$ and $f(x, t)$. Although the expansion on only $p(x, t)$ is good enough to predict the occurrence of different intrinsic behaviors in CANNs with STD (chapter 3), the transient dynamics can only be predicted satisfactorily by using perturbative expansion for all the dynamical variables, especially for cases with parameters near phase boundaries. For example, the duration of the plateau state can only be predicted by full perturbative analysis.

For short-term synaptic facilitation (STF), I have found that CANNs with STF can only track changes of external stimulus slowly. However, since STF enhances the translational stability, it can reduce the effect of noise. I have shown that, both analytically and experimentally, CANNs with STF can implement a noise filter.

In the next two chapters, I will present potential applications of CANNs with STD. In these two work, we found that some results are highly comparable to experimental results obtained from neuroscience and psychology experiments.

Chapter 5

Tracking with Synaptic Depression

5.1 Introduction

In the nervous system, delays are common due to physical constraints of the network. Accumulation of membrane potentials, transmission of action potentials and network internal dynamics are possible sources. In the visual pathway, the accumulated delay is serious. Martinez-Conde *et al.* reported that the latency of LGN after an onset of a stimulus is about 20 - 30 ms and the latency of the primary visual cortex (V1) is 40 - 50 ms [30]. Latencies of the order of magnitude of 100 ms would be critical, if the stimulus changes very fast. For example, for a moving object with speed 100 km/h (similar to the speed of a base ball pitch), the perceived position of the moving object will differ from the real position by roughly 1 m. If there is no delay compensation mechanism, baseball hitters should have no chance to hit a baseball. However, in reality, hitters can still hit home runs. So, there must be delay compensation mechanisms in the nervous system to satisfy our daily needs.

Neuronal responses of neurons in the rat's anterior thalamic nucleus (ATN) and postsubiculum (PoS) are found to represent head directions of rats on a horizontal plane. Taube *et al.* report that, for freely moving rats, ATN 'head direction' (HD) neurons anticipate the future head direction of the rat, i.e. neuronal response corresponds to the future head direction. The period ATN neurons anticipate is about +23 ms. Neuronal responses of PoS HD neurons are found to represent the past head direction (delayed by 7 ms) [31].

In this chapter, I will present our work based on continuous attractor neural networks (CANNs) with short-term synaptic depression (STD). In chapter 3, I have reviewed our work on CANNs with STP. CANNs with STD can support rich dynamics depending on parameters (rescaled levels of STD and inhibition). In Figure 5.1(a), I quote the phase diagram of CANNs with STD over the parameter space (comparison with simulation results can be found in Figure 3.5). York *et al.* reported a similar phase dia-

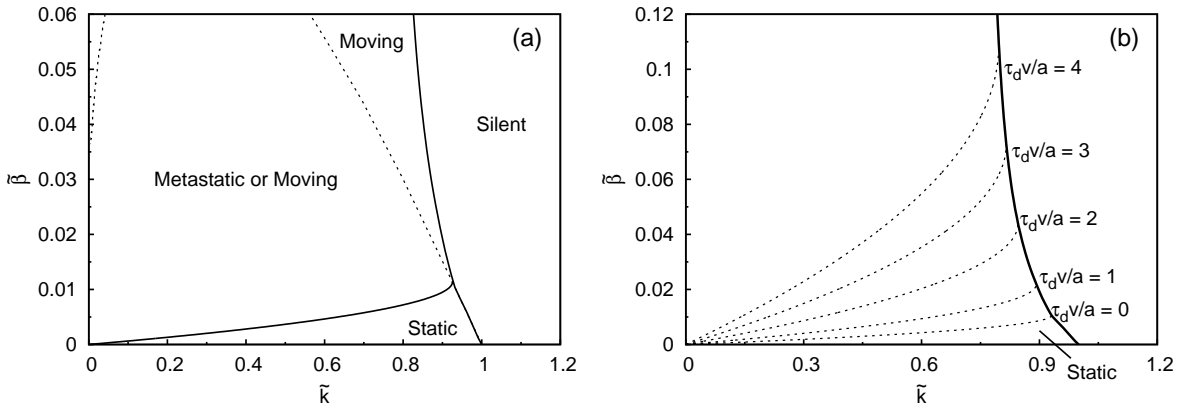


Figure 5.1: (a) Phase diagram of CANNs with STD over the parameter space spanned by $(\tilde{k}, \tilde{\beta})$. Here, \tilde{k} is the rescaled inhibition and $\tilde{\beta}$ is the rescaled level of STD. (b) Speed of spontaneously moving network state profile (v). Other parameter: $\tau_d/\tau_s = 50$.

gram in the literature [27]. In the regions named ‘Metastatic or Moving’ and ‘Moving’, the bump-shaped network state moves spontaneously due to the dynamics of STD. The speed of the spontaneously moving network state profile is shown in Figure 5.1(b). In the later part of this chapter, we can see how the spontaneous moving behavior reshapes the tracking dynamics. Figure 5.1 quoted here is for reference.

The CANN with STD model is the same as Eqs. (3.5) and (3.6). To simplify combinations of parameters, here we use the rescaled version of Eqs. (3.5) and (3.6). The rescaled versions of Eqs. (3.5) and (3.6) are

$$\tau_s \frac{d\tilde{u}}{dt}(x, t) = -\tilde{u}(x, t) + \rho \int dx' \tilde{J}(x, x') p(x', t) \tilde{r}(x', t) + \tilde{I}^{\text{ext}}(x, t) \quad (5.1)$$

$$\tau_d \frac{dp}{dt}(x, t) = 1 - p(x, t) - \tilde{\beta} p(x, t) \tilde{r}(x, t) \quad (5.2)$$

$\tilde{u}(x, t)$ is the rescaled neuronal current of neurons having preferred stimulus x at time t . $\tilde{r}(x, t)$ is the rescaled neuronal activity of neurons at preferred stimulus x and time t , given by

$$\tilde{r}(x, t) = \frac{\tilde{u}(x, t)^2 \Theta[\tilde{u}(x, t)]}{1 + \frac{\tilde{k}}{8\sqrt{2\pi a}} \int dx' \tilde{u}(x', t)^2 \Theta[\tilde{u}(x', t)]}, \quad (5.3)$$

where \tilde{k} is the rescaled level of inhibition. $\tilde{J}(x, x')$ is the rescaled excitatory coupling. $p(x, t)$ is the available fraction of neurotransmitters. So, $J(x, x')p(x', t)$ is the effective synaptic efficacy. $\tilde{\beta}$ is the rescaled level of STD. τ_s is the timescale of $\tilde{u}(x, t)$, τ_d is the timescale of STD with $\tau_d/\tau_s = 50$. To determine the stimulus encoded by the network activity profile, we define

$$z(t) = \frac{\int dx x u(x, t)}{\int dx u(x, t)}. \quad (5.4)$$

The external input $\tilde{I}^{\text{ext}}(x, t)$ is chosen to be

$$\tilde{I}^{\text{ext}}(x, t) = \tilde{A} \exp\left(-\frac{|x - z_0(t)|^2}{4a^2}\right), \quad (5.5)$$

where \tilde{A} is the rescaled strength of the external input and $z_0(t)$ is the true position of the stimulus. Although the form of an external input can be arbitrary, the perturbative expansion of $\tilde{u}(x, t)$ (Eq. (4.11)) shows that the projection of the external input onto $(x - z) \exp[-|x - z|^2/(4a^2)]$ is the most important term driving the tracking dynamics, which is similar to Eq. (5.5).

5.2 Modulation of Tracking Dynamics due to Short-term Synaptic Depression

Changes of the external input drive the motion of bump-shaped network state profile. In Figure 2.2, I have illustrated that CANNs can support bump-shaped network activity profiles centered at any preferred stimulus. Since all bump-shaped network activity profiles link together to form a line attractor, the network activity profile can change its position easily upon the change of the external input.

The network activity profile can track moving stimuli. For example, in Figure 5.2, the stimulus starts to move with a speed v in the positive direction at $t = 0$. The $\tilde{u}(x, t)$ profile moves in the positive direction and eventually catches up the speed of the moving stimulus.

In Figure 5.3(a), for the case without STD, the center of mass of $\tilde{u}(x, t)$, $z(t)$, (symbols) tracks the moving stimulus (dashed line) with a lag. At $t = 0$, the network activity profile was about to move. After an acceleration, the speed of the network activity profile matches the speed of the moving stimulus. As a result, the delay of the network response to the stimulus is steady.

Short-term synaptic depression can modify the tracking dynamics of network activity profiles. In Figure 5.3(b), at the beginning, the tracking behavior of the network activity profile is similar to that in Figure 5.3(a). However, the intrinsic dynamics due to STD drives the move further forward. For a particular value of $\tilde{\beta} \equiv \tilde{\beta}_{\text{perfect}} \approx 0.0035$, the terminal delay of the network response to the moving stimulus will be effectively zero. For $\tilde{\beta} > \tilde{\beta}_{\text{perfect}}$, the network responds to a future position of the moving stimulus, as shown in Figure 5.3(c). For trackings with a negligible terminal delay, we name the

phenomenon ‘perfect tracking’. For trackings that the network activity profile advances the true stimulus, we name the phenomenon ‘anticipatory tracking’.

To analyze the tracking dynamics, we use perturbative expansions of $\tilde{u}(x, t)$ and $p(x, t)$ introduced in section 4.3. Consider

$$\tilde{u}(x, t) = \sum_k \tilde{u}_k(t) \psi_k(x - z(t)), \quad (5.6)$$

$$p(x, t) = \sum_k p_k(t) \varphi_k(x - z(t)), \quad (5.7)$$

we have

$$\begin{aligned} & \tau_s \left[\frac{d\tilde{u}_k}{dt} - \frac{\dot{z}}{2a} (\sqrt{k+1}\tilde{u}_{k+1} - \sqrt{k}\tilde{u}_{k-1}) \right] \\ &= -\tilde{u}_k + \frac{1}{B} \left(\sum_{nm} C_{nm}^k \tilde{u}_n \tilde{u}_m - \sum_{nml} D_{nml}^k \tilde{u}_n \tilde{u}_m p_l \right) + \tilde{I}_k \end{aligned} \quad (5.8)$$

$$\begin{aligned} & \tau_d \left[\frac{dp_k}{dt} - \frac{\dot{z}}{\sqrt{2}a} (\sqrt{k+1}p_{k+1} - \sqrt{k}p_{k-1}) \right] \\ &= -p_k + \frac{\tilde{\beta}}{B} \left(\sum_{nm} E_{nm}^k \tilde{u}_n \tilde{u}_m - \sum_{nml} F_{nml}^k \tilde{u}_n \tilde{u}_m p_l \right), \end{aligned} \quad (5.9)$$

where C_{nm}^k , D_{nml}^k , E_{nm}^k and F_{nml}^k are defined in Eqs. (4.19) - (4.22). \tilde{I}_k is given by

$$\tilde{I}_k = \tilde{A} \sqrt{\frac{\sqrt{2\pi}a}{k!}} \left(\frac{z_0 - z}{2a} \right)^k \exp \left(-\frac{s(t)^2}{8a^2} \right) \quad (5.10)$$

where s is the displacement from the stimulus to the center of mass of $\tilde{u}(x, t)$ given by

$$s(t) \equiv z(t) - z_0(t) \text{ and} \quad (5.11)$$

$$\frac{ds}{dt}(t) = \dot{z}(t) - v. \quad (5.12)$$

By integrating Eqs. (5.8), (5.9) and (5.12), we can predict the motion of the center of mass of $\tilde{u}(x, t)$. Predictions with expansions up to $k = 5$ are shown in Figure 5.3. It suggests that the perturbative analysis is useful in the case of moving stimuli.

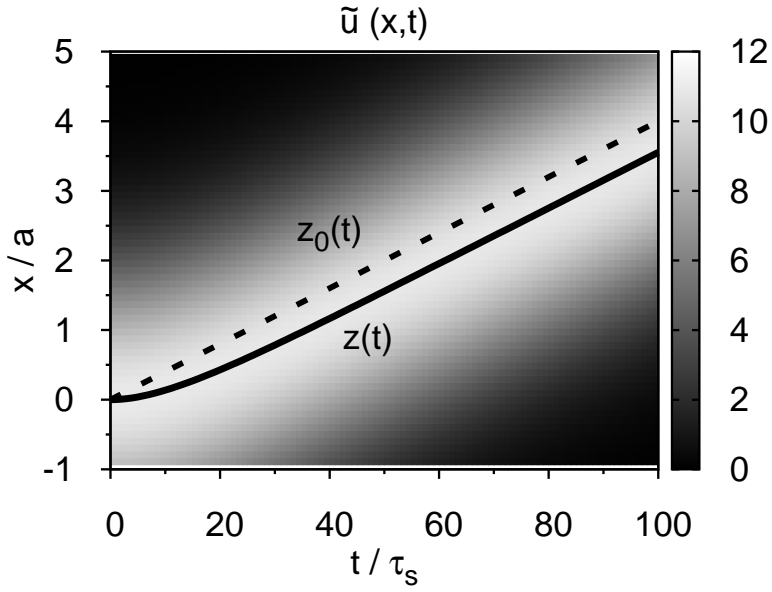


Figure 5.2: The network reaction to a moving stimulus. Raster plot: $\tilde{u}(x,t)$. Dashed line: moving stimulus, $z_0(t)$. Solid line: the center of mass of $\tilde{u}(x,t)$, $z(t)$. Parameters: $\tilde{k} = 0.5$, $\tilde{\beta} = 0$, $\tilde{A} = 1.0$ and $\tau_s v/a = 0.04$.

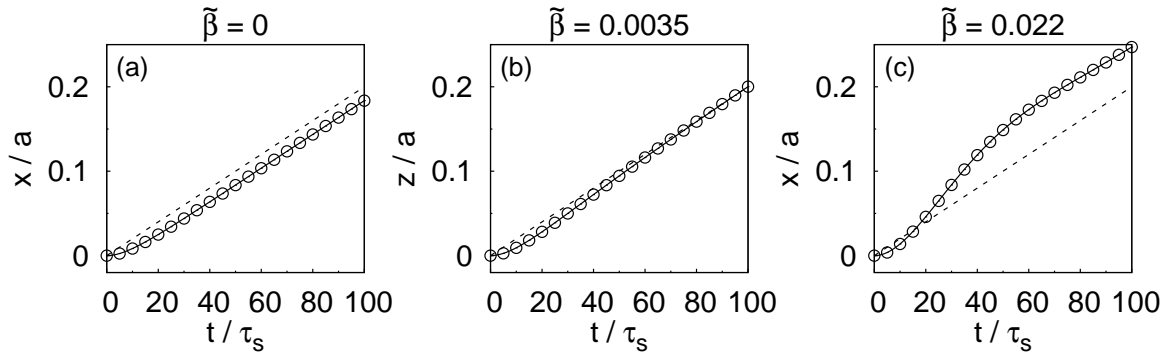


Figure 5.3: Centers of mass of $\tilde{u}(x,t)$ for various $\tilde{\beta}$'s. Symbols: simulations. Dashed line: the moving stimulus, $z_0(t)$. Solid line: prediction by $k = 5$ perturbation. Other parameters: $\tilde{k} = 0.4$, $\tilde{A} = 1.8$, $\tau_s v/a = 0.0002$ and $\tau_d/\tau_s = 50$.

5.3 Perfect Tracking & Anticipatory Tracking

In Figures 5.3(b) and (c), there are parameters for which the network response does not eventually lag behind the external moving stimulus. By solving the fixed point solution of Eqs. (5.8), (5.9) and (5.12), we can obtain the displacement s as a function of \tilde{k} , $\tilde{\beta}$, \tilde{A} and v .

In Figure 5.4(a), there are three cases of terminal delay s as functions of v . For $\tilde{\beta} = 0$, within the range of v presented in Figure 5.4(a), s is almost a linear function with a negative slope. We quantify how long the network response advances the true stimulus by a quantity τ_{ant} (named *anticipatory time*) defined by

$$\tau_{\text{ant}} \equiv \frac{s}{v}. \quad (5.13)$$

As we can see, in this case, $\tau_{\text{ant}} < 0$. It means that there is a delay of the network response to the moving stimulus.

For $\tilde{\beta} \approx 0.0035 \approx \tilde{\beta}_{\text{perfect}}$, there is a range of v such that s is almost zero. So, within this range, the anticipatory time is almost zero. However, if the speed of the stimulus is too high, τ_{ant} is significantly negative. So, there is a range of v for perfect tracking. For $\tilde{\beta} = 0.022 > \tilde{\beta}_{\text{perfect}}$, between $-1 \lesssim \tau_{\text{ant}}/v \lesssim 1$, s increases with v . There is a region that the slope is almost a constant. So, the anticipatory time is positive and almost a constant over this range.

In Figure 5.4(b), there is a three-dimensional plot for $\tilde{k} = 0.4$ and $\tilde{A} = 1.8$. It shows that, for $\tilde{\beta} = 0$, the slope of s against v is negative within the range of v , as mentioned above. If $\tilde{\beta}$ increases, the slope of s against v near $v = 0$ increases accordingly.

To analyze the perfect tracking behavior, let us consider approximations of dynamical variables

$$\tilde{u}(x, t) = \tilde{u}_0(t) \exp\left(-\frac{|x - z(t)|^2}{4a^2}\right) \quad (5.14)$$

$$p(x, t) = 1 - p_0(t) \exp\left(-\frac{|x - z(t)|^2}{2a^2}\right) + p_1(t) \left(\frac{x - z(t)}{a}\right) \exp\left(-\frac{|x - z(t)|^2}{2a^2}\right) \quad (5.15)$$

Substituting these two assumptions into Eqs. (5.1) and (5.2) and utilizing the

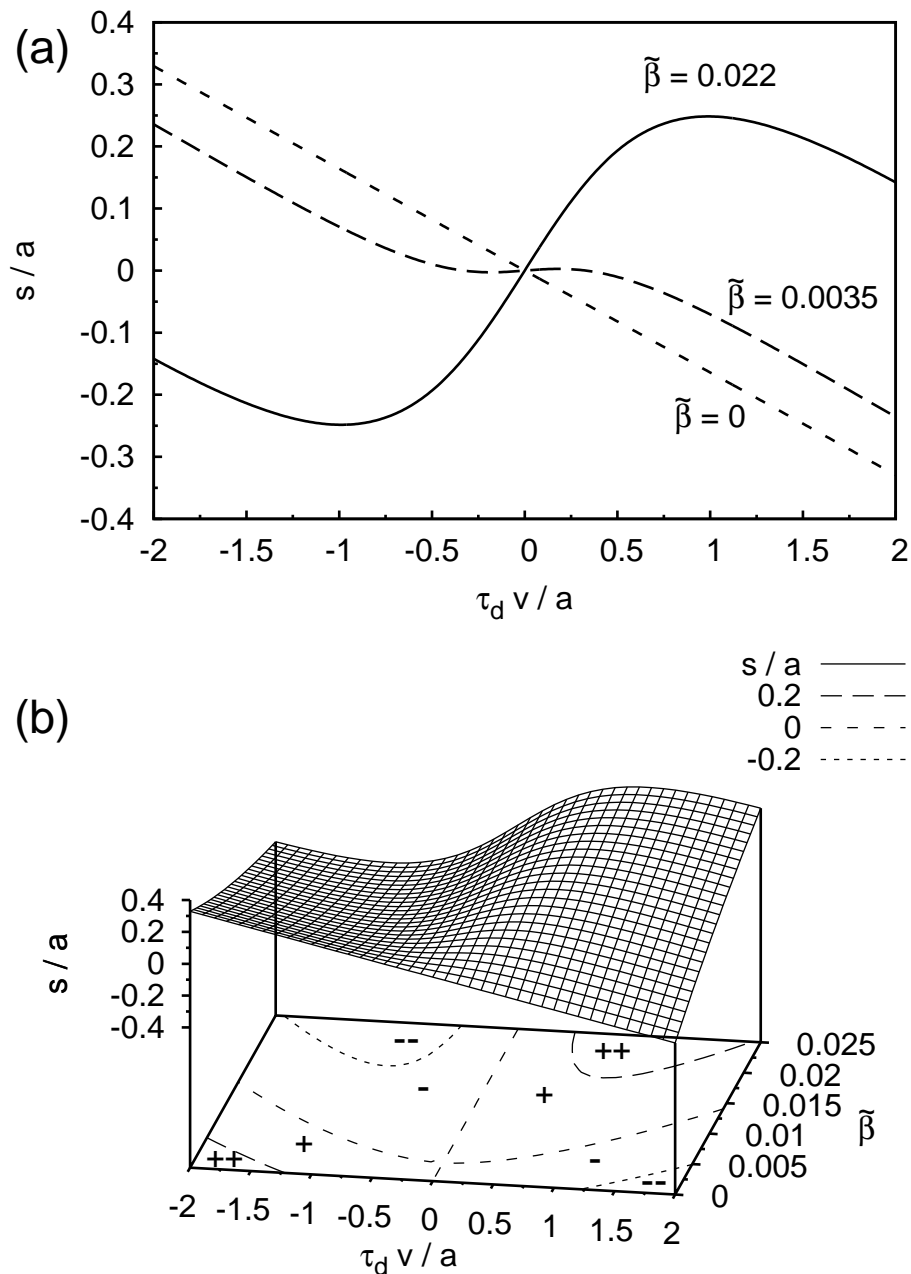


Figure 5.4: (a) The terminal displacements s as functions of velocities of external stimuli in three particular sets of parameters. Parameters: $\tilde{k} = 0.4$, $\tilde{A} = 1.8$ and $\tau_d/\tau_s = 50$. (b) The terminal displacements s as a function of $\tilde{\beta}$ and v . Grid: the surface plot of s against $\tilde{\beta}$ and v . Bottom: a contour plot. ‘++’: in the region, $s/a > 0.2$. ‘+’: $0 < s/a < 0.2$. ‘-’: $-0.2 < s/a < 0$. ‘-’: $s/a < -0.2$.

orthogonality of the basis functions, we should obtain (see Appendix C)

$$\tau_s \frac{d\tilde{u}_0}{dt} = \frac{\tilde{u}_0^2}{\sqrt{2}B} \left(1 - p_0 \sqrt{\frac{4}{7}} \right) - \tilde{u}_0 + \tilde{A} \exp \left[-\frac{(vt - z)^2}{8a^2} \right], \quad (5.16)$$

$$\frac{\tau_s}{2a} \frac{dz}{dt} = \frac{\tilde{u}_0}{B} \left(\frac{2}{7} \right)^{\frac{3}{2}} p_1 + \frac{\tilde{A}}{2\tilde{u}_0} \left(\frac{vt - z}{a} \right) \exp \left[-\frac{(vt - z)^2}{8a^2} \right] \quad (5.17)$$

$$\tau_s \frac{dp_0}{dt} = \frac{\tau_s}{\tau_d} \left[\frac{\tilde{\beta}\tilde{u}_0^2}{B} \left(1 - p_0 \sqrt{\frac{2}{3}} \right) - p_0 \right] - \frac{\tau_s p_1}{2a} \frac{dz}{dt} \quad (5.18)$$

$$\frac{\tau_s}{p_0} \frac{dp_1}{dt} = -\frac{\tau_s}{\tau_d} \left[1 + \frac{\tilde{\beta}\tilde{u}_0^2}{B} \left(\frac{2}{3} \right)^{\frac{3}{2}} \right] \frac{p_1}{p_0} + \frac{\tau_s}{a} \frac{dz}{dt} \quad (5.19)$$

This is the 1st order perturbation on the dynamical variables. At the steady state, $d\tilde{u}_0/dt = dp_0/dt = dp_1/dt = 0$, and $dz/dt = v$. Furthermore, for a sufficiently small displacements, i.e., $|s|/a \ll 1$, one can approximate $\tilde{A} \exp[-(vt - z)^2/(8a^2)] \approx \tilde{A}$ and $\tilde{A}[(vt - z)/a] \exp[-(vt - z)^2/(8a^2)] \approx -\tilde{A}s/a$. Solving the above equations, we find that s/a can be expressed in terms of the variables \tilde{u}_0/\tilde{A} , τ_s/τ_d and $v\tau_d/a$. When $v\tau_d/a \ll 1$, the rescaled displacement s/a can be approximated by a power series expansion of the rescaled velocity $v\tau_d/a$. Since the displacement reverses sign when the velocity reverses, s/a is an odd function of $v\tau_d/a$. This means that $s/a \approx c_1(v\tau_d/a) + c_3(v\tau_d/a)^3$. For perfect tracking in the low velocity limit, we have $c_1 = 0$ and find

$$\frac{s}{a} = -\frac{C}{2} \frac{\tilde{u}_0}{\tilde{A}} \frac{\tau_s}{\tau_d} \left(\frac{v\tau_d}{a} \right)^3, \quad (5.20)$$

where C is a parameter less than 1 (the detailed expression can be found in Appendix C). For the network tracking a moving stimulus, the input magnitude cannot be too small. This means that \tilde{u}_0/\tilde{A} is not a large number. Therefore, for tracking speeds up to $v\tau_d/a \sim 1$, the displacement s is very small and can be regarded as zero effectively (see Figure 5.4(a)). The velocity range in which the tracking is effectively perfect is rather broad, since it scales as $(\tau_d/\tau_s)^{1/3} \gg 1$. Because the anticipatory time is given by

$$\frac{\tau_{\text{ant}}}{\tau_d} = \frac{C}{2} \frac{\tilde{u}_0}{\tilde{A}} \frac{\tau_s}{\tau_d} \left(\frac{v\tau_d}{a} \right)^2. \quad (5.21)$$

The range of velocity that the anticipatory time is effectively zero scales as $(\tau_d/\tau_s)^{1/2} \gg 1$.

Equation (5.20) is valid when $\tilde{\beta}$ takes a particular value. This yields an estimate of $\tilde{\beta}_{\text{perfect}}$ in the 1st order perturbation. Its expression is derived in Appendix C and plotted in Figure 5.5. For reference, we also plot the boundary that separates the metastatic phase above it from the static phase below, as reported in the study of intrinsic properties

of CNNs with STD in [24]. In the static phase, the bump is stable at any position, whereas in the metastatic phase, the static bump starts to move spontaneously once it is pushed. Hence we say that the phase boundary is in a *ready-to-move* state. Figure 5.5 shows that $\tilde{\beta}_{\text{perfect}}$ is just above the phase boundary. Indeed, when \tilde{A} approaches 0, the expression of $\tilde{\beta}_{\text{perfect}}$ reduces to the value of $\tilde{\beta}$ along the phase boundary for the 1st order perturbation. Figure 5.6 confirms that $\tilde{\beta}_{\text{perfect}}$ does not change significantly with \tilde{A} for different values of \tilde{k} . This implies that the network with $\tilde{\beta} = \tilde{\beta}_{\text{perfect}}$ exhibits effectively perfect tracking performance because it is intrinsically in a ready-to-move state.

We can further theoretically explore the network dynamics when the STD strength is higher than that for achieving perfect tracking. By solving Eqs. (5.8), (5.9) and (5.12) up to $k = 11$, we obtain the relation between the displacement s and the stimulus speed v . The solid curve in Figure 5.4 shows that for strong STD, s increases linearly with v over a broad range of v . This implies that the network achieves a constant anticipatory time τ_{ant} over a broad range of the stimulus speed.

To gain insights into how the anticipation time depends on the stimulus speed, we consider the regime of small displacements. In this regime, the rescaled displacement s/a can be approximated by a power series expansion of the rescaled velocity $v\tau_d/a$, leading to $s/a = c_1(v\tau_d/a) + c_3(v\tau_d/a)^3$. The coefficients c_1 and c_3 are determined such that the anticipation time in the limit $v = 0$ should be $\tau_{\text{ant}}(0) = s/v$, and that s/a reaches a maximum when $v = v_{\text{max}}$. This yields the result

$$\frac{s}{a} = \frac{\tau_{\text{ant}}(0)}{\tau_d} \left[\frac{v\tau_d}{a} - \frac{1}{3} \left(\frac{a}{v_{\text{max}}\tau_d} \right)^2 \left(\frac{v\tau_d}{a} \right)^3 \right]. \quad (5.22)$$

Hence the anticipatory time is given by

$$\tau_{\text{ant}}(v) = \tau_{\text{ant}}(0) \left(1 - \frac{v^2}{3v_{\text{max}}^2} \right). \quad (5.23)$$

This shows that the anticipation time is effectively constant in a wide range of stimulus velocities, as shown in Figure 5.7. Even for $v = 0.5v_{\text{max}}$, the anticipation time is only reduced from its maximum by 9%.

The contours of anticipatory times for slowly moving stimuli are shown in Figure 5.8. Hence the region of anticipative behavior effectively coincides with the metastatic phase, as indicated by the region above the phase line (dotted line) in Figure 5.8. In summary, there is a direct correspondence between delayed, perfect, and anticipative tracking on one hand, and the static, ready-to-move, and spontaneously moving behaviors on the other. This demonstrates the strong correlation between the tracking

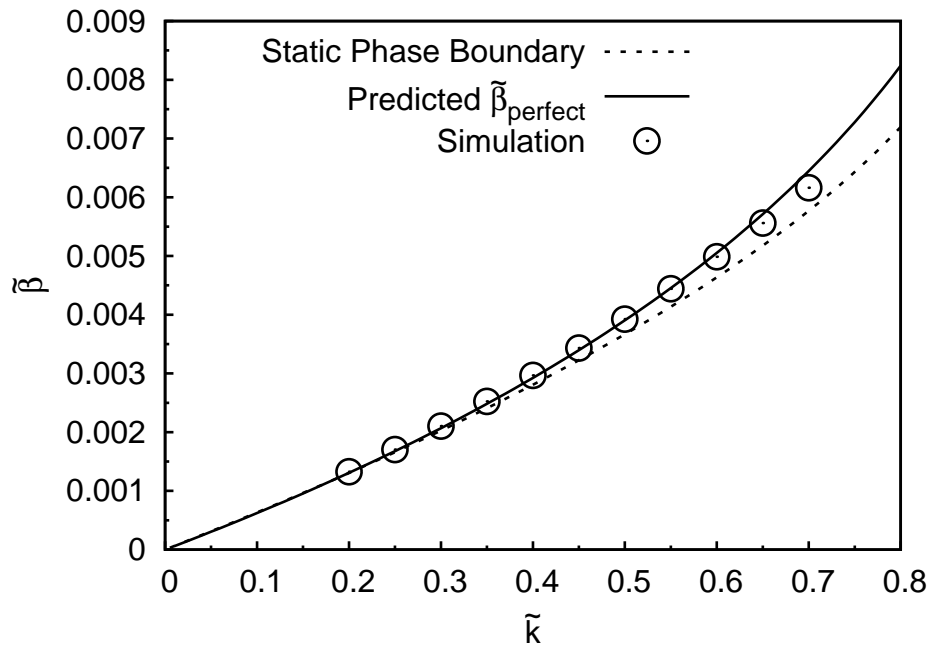


Figure 5.5: $\tilde{\beta}$ for perfect tracking against \tilde{k} for $\tilde{A} = 1.8$. Dotted line: phase boundary for the static phase in Figure 5.1(a). Parameter: $\tau_d/\tau_s = 50$.

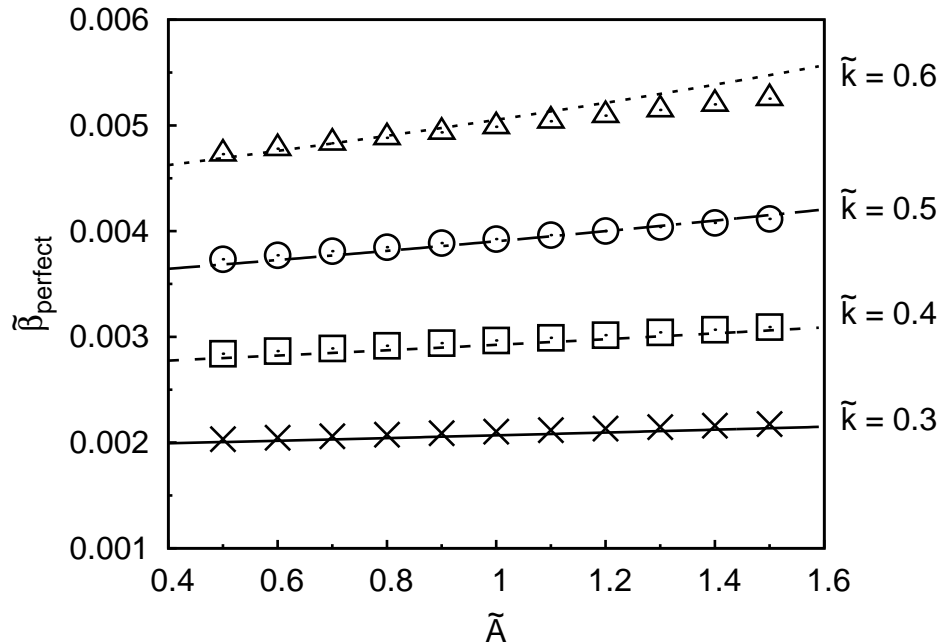


Figure 5.6: Plot of $\tilde{\beta}_{\text{perfect}}$ against \tilde{A} for various \tilde{k} 's. Symbols: simulations. Curves: predictions for corresponding \tilde{k} . Parameter: $\tau_d/\tau_s = 50$.

performance and the intrinsic behaviors of the CANN.

Figure 5.8 suggests the physical origin of anticipatory tracking over the space. It shows that anticipation happens only when the profile of $u(x, t)$ moves spontaneously in space. To understand it, one can also look at Figure 5.3(c). At the beginning, the center of mass of $u(x, t)$ lags the stimulus. Later, due to the symmetry broken by the moving stimulus, it moves to the same direction of the moving stimulus. Since the profile can move faster than the stimulus, the $u(x, t)$ profile can eventually overtake the stimulus. However, once the profile overtakes the stimulus, it was slowed down by the attraction from the stimulus. As a result, at the equilibrium state, the profile moves at the same speed as the stimulus, but leads the way.

We compare the prediction of the model with experimental data. In a typical HD experiment of rodents [32], $\tau_s = 1$ ms, $a = 28.5$ degree/ $\sqrt{2}$, and the anticipation time drops from 20 ms at $v = 0$ to 15 ms at $v = 360$ degree/s. Substituting into Eq. (5.22) and assuming $\tau_d = 50\tau_s$, these parameters yield a slope of 0.41 at the origin and the maximum lead at $v_{\max}\tau_d/a = 1.03$. This result can be compared favorably with the curve of $\tilde{\beta} = 0.022$ in Figure 5.7, where the slope at the origin is 0.45 and the maximum lead is located at $v_{\max}\tau_d/a = 1.01$. Based on these parameters, the lowest curve plotted in Figure 5.7 is consistent with the real data in Fig. 4 of [32].

5.4 Tracking with Natural Speed of the Continuous Attractor Neural Network

Apart from the anticipatory tracking, there is a new phenomenon due the short-term synaptic depression, which is not reported in the literature, to my knowledge. Without an external input ($\tilde{A} = 0$), for combinations of $(\tilde{k}, \tilde{\beta})$ within parameter regions in metastatic phase and moving phase (in Figure 5.1(a)), the bump-shaped network response can move spontaneously with a particular speed, namely the natural speed v_{natural} . Its value depends on parameters, as shown in Figure 5.1(b).

Two sets of curves corresponding to two values of $\tilde{\beta}$ are shown in Figure 5.9, when the stimulus amplitude \tilde{A} is sufficiently strong. The lines L_1 and L_2 indicate the corresponding natural speeds of the system for these values of $\tilde{\beta}$. Remarkably, we obtain a confluence point of these curves at the natural speed. This point is referred to as the *natural tracking point*. It has the important property that the lag is independent of the stimulus amplitude. This independence of s from \tilde{A} persists in the asymptotic

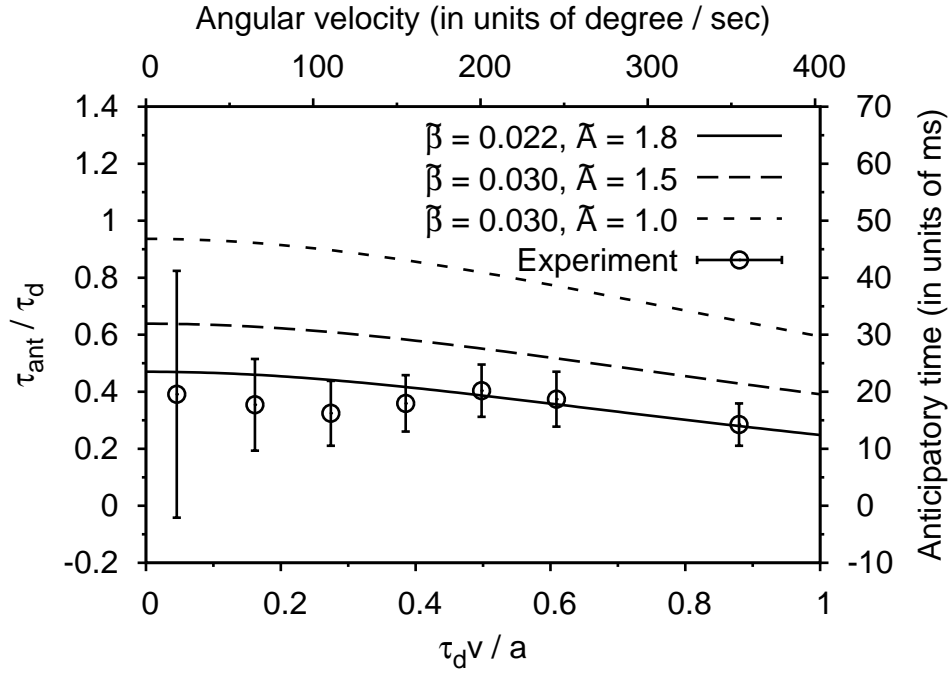


Figure 5.7: Anticipatory time as a function of the speed of the moving stimulus. Curves: predictions given by the model with different parameters. Symbols with error bars: experimental results quoted in [32]. Primary horizontal axis: controlled parameter in the model. Primary vertical axis: predicted anticipatory time by the model. Secondary horizontal axis: angular velocity of rodents quoted in [32]. Secondary vertical axis: measured anticipatory time quoted in [32]. Parameter: $\tau_d/\tau_s = 50$.

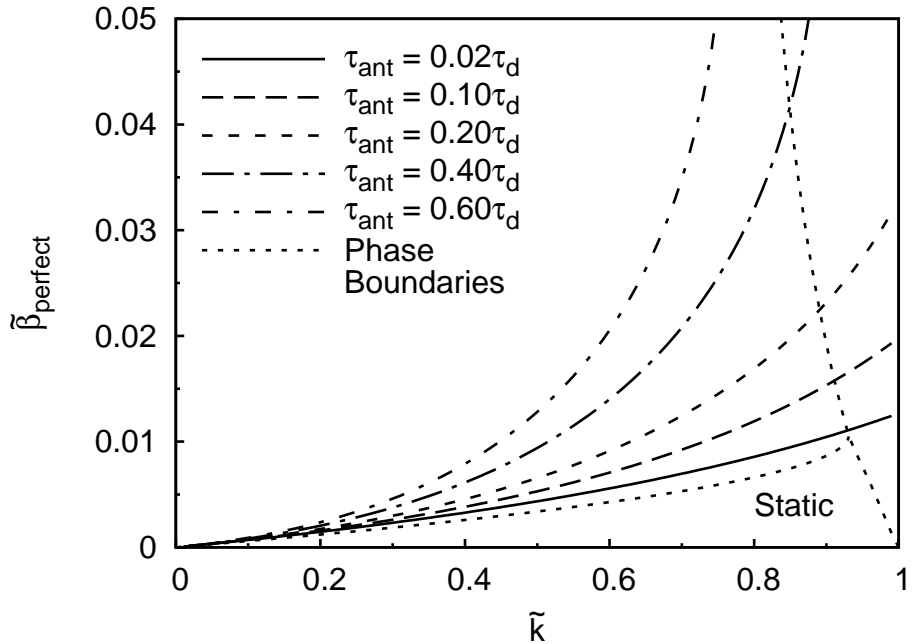


Figure 5.8: Anticipatory time over the phase diagram. Dotted line: phase boundaries in Figure 5.1(a). Parameters: $\bar{\alpha} = 0.5$ and $\tau_d/\tau_s = 50$.

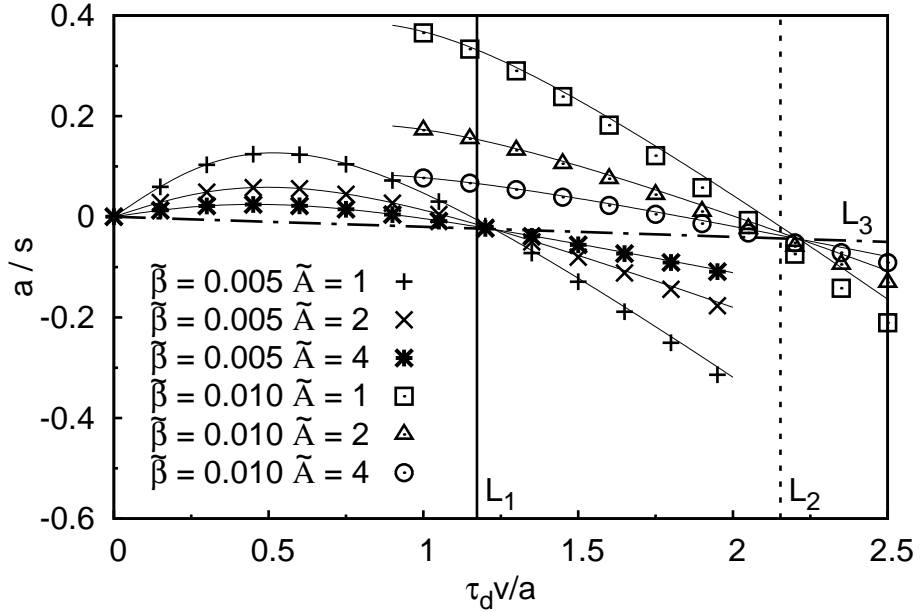


Figure 5.9: The dependence of the displacement s on the stimulus speed v . The confluence points of the two families of curves are marked by the arrows. Symbols: simulations. Solid lines: 11th order perturbation. L_1 : natural speed at $\tilde{\beta} = 0.005$. L_2 : natural speed at $\tilde{\beta} = 0.01$. L_3 : the line of natural tracking points in the strong \tilde{A} limit. Parameter: $\tilde{k} = 0.3$.

limit of large \tilde{A} . In this limit, s approaches $-v_{\text{natural}}\tau_s$, corresponding to a delay time of τ_s , showing that the response is limited by the synaptic time scale in this limit. This asymptotic limit is described by the line L_3 and is identical for all values of \tilde{k} and $\tilde{\beta}$. Hence the invariant point for natural tracking is given by $(v, s) = (v_{\text{natural}}, -v_{\text{natural}}\tau_s)$ for all values of \tilde{k} and $\tilde{\beta}$.

We also consider natural tracking in the weak \tilde{A} limit (detailed calculation can be found in Appendix D) [24]. Again we find a confluence point of the displacement curves at the natural speed, but the delay time (and in some cases the anticipation time) depends on the value of \tilde{k} . For example, at $\tilde{k} = 0.3$, the natural tracking point traces out an effectively linear curve in the space of v and s when $\tilde{\beta}$ increases, with a slope equal to $0.8\tau_s$. This shows that the delay time is $0.8\tau_s$, effectively independent of $\tilde{\beta}$ at $\tilde{k} = 0.3$. Since the delay time is different from the value of τ_s applicable in the strong \tilde{A} limit, the natural tracking point is slowly drifting from the weak to the strong \tilde{A} limit. However, the magnitude of the natural time delay remains of the order of τ_s . This is confirmed by the analysis of the dynamical equations when the stimulus speed is $v_{\text{natural}} + \delta v$ in the weak \tilde{A} limit.

5.5 CANNs with Mexican-hat Coupling

To investigate whether the delay compensation behavior and the prediction of the natural tracking point are general features of CANN models, we consider a network with Mexican-hat couplings. We replace $J(x, x')$ in Eq. (4.1) by

$$J^{\text{MH}}(x, x') = J_0 \left[\frac{1}{2} - \left(\frac{x - x'}{2a} \right)^2 \right] \exp \left[-\frac{(x - x')^2}{2a^2} \right], \quad (5.24)$$

and $r(x, t)$ in Eqs. (4.1) and (4.2) by

$$r(x, t) = \Theta[u(x, t)] \frac{u(x, t)^2}{1 + u(x, t)^2} \quad (5.25)$$

Figure 5.10 shows that the network exhibits the same behaviors as the model in Eqs. (4.1) and (4.2). As shown in Figure 5.10(a), the anticipatory times are effectively constant and similar in magnitude in the range of stimulus speed comparable to experimental settings. In Figure 5.10(b), the natural speed of the bump is zero for β less than a critical value. As β increases, the natural speed increases from zero. In Figure 5.10(c), the displacement s is plotted as a function of the stimulus speed v . The invariance of the displacement at the natural speed, independent of the stimulus amplitude, also appears in the Mexican-hat model. The confluence point of the family of curves is close to the natural speed. Furthermore, the displacement at the natural tracking point increases with the natural speed.

5.6 Summary

I have presented two behaviors in CANNs due to STD. The first phenomenon is the modification of tracking dynamics. For CANNs without STD, the network response always lags behind a moving stimulus. However, if spontaneous motions of a bump-shaped network activity profile is possible, the network response can eventually catch up or overtake the true moving stimulus. From our analysis, we found that there are particular combinations of parameters such that the network response can track the true moving stimulus with a negligible lag. These particular combinations of parameters almost coincides with the phase boundary separating the static phase and metastatic phase. It suggests that when STD is strong enough to drive spontaneous motions of the network activity profile, it can then make perfect tracking and anticipatory tracking

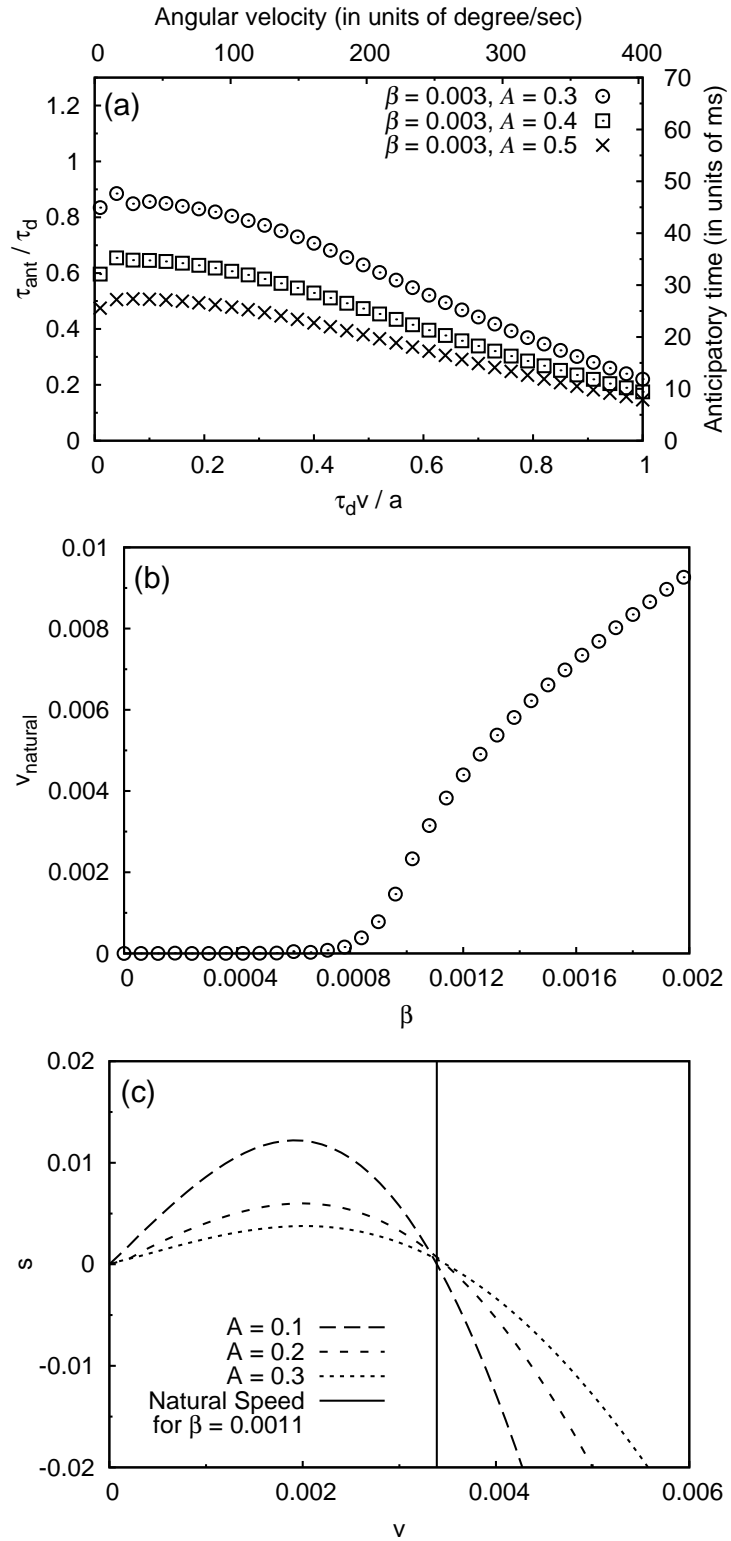


Figure 5.10: (a) The dependence of anticipatory time on the stimulus speed in the Mexican-hat model. Parameter: $\beta = 0.003$. (b) Natural speed of the network as a function of β . (c) Plot of s against v . There is a confluence point at the natural speed of the system. L_1 : the natural speed of the system at $\beta = 0.0011$. Common parameters: $\rho = 128 / (2\pi)$, $J_0 = 0.5$ and $a = 0.5$.

happen. It shows the relation between the intrinsic dynamics of CANNs with STD and the tracking dynamics. Also, the model is found to be able to fit experimental results in a rodent experiment.

I have also presented a new phenomenon in CANNs with STD: natural tracking. When the stimulus moves at the natural speed of the CANNs with STD, the displacement from the true stimulus and the stimulus encoded by the network response is insensitive to the change of the magnitude of the external input. This is not reported in the literature. It suggests a possible way to detect the speed of spontaneous motions of attractor states on CANNs.

Other mechanisms to implement delay compensation are also possible in the neural system. For example, there are starburst amacrine cells on the retina to detect motion of images [33]. Those cells can provide an asymmetric inhibition to implement delay compensation. However, this mechanism cannot be used if the animal is in the dark. Conjunctive cells are found to drive the network state according to the motion of animals [6]. It has a possibility to provide anticipatory effect. For the models proposed by Redish *et al.* and Goodridge *et al.*, separately, the anticipation is achieved by the interaction between two neural networks [19, 32]. Zhang has proposed that asymmetric couplings can drive the bump to move. However, he did not specify the mechanism to make couplings asymmetric [10]. Since STD is very common in the brain, the present mechanism due to STD is biologically feasible. The anticipatory effect proposed here can be implemented based on the internal dynamics of the neural network only. Of course, other neural models supporting spontaneous moving bumps (e.g. asymmetric couplings [10], neural field models with spike frequency adaptation [34] and two-layer CANNs [29]) may be used to implement anticipatory tracking in a similar manner. In the next chapter, I will present another theory to explain how CANNs encode acutely overlapped stimuli. This theory is also due to the dynamics driven by STD.

Chapter 6

A Model That Enhances Perception Resolution¹

6.1 Introduction

In nervous systems of most primates, there are regions of cortex responsible to visual information. From anatomical studies, visual information from the retina was first transmitted to lateral geniculate nucleus (LGN). LGN is a relay between eyes and the visual cortex [36]. In the visual cortex, there are subdivisions found to have various functions to perceive features of visual information. The most well-studied subdivision of the visual cortex is the primary visual cortex (V1). V1 can perform pattern recognition on static or moving objects. In 1985, Daugman found that, some V1 neurons can be modeled by Gabor filters [9].

For moving directions of objects, Albright found that in the middle temporal (MT or V5), neuronal activities of some neurons represent the moving direction of moving objects seen by the animal [8]. The averaged neuronal activity of a neuron is a bump-shaped function of moving directions, known as the *tuning curve* of the neuron. Each neuron has its own preferred moving direction. Their tuning curves have maxima at their preferred moving directions. Also, tuning curves have various widths, ranging from about 32° to about 186°.

However, since the widths of tuning curves are at least 32°, there is a puzzle on distinguishing superimposed moving directions having a difference less than tuning widths, if the nervous system uses peak positions or centers of mass of the neuronal activity profile to decode the information contained in the neuronal activity profile. Treue *et al.* found that the peak of time-averaged neuronal activity profile begins to split into two only if the difference between two moving directions is larger than the tuning widths of

¹This chapter is a report of my contribution published in [35].

neurons [37]. However, Mather *et al.* found that the ability to distinguish two moving directions when the angle between them is 10° or less [38].

There are theories to explain the observation of neuronal activities as well as the ability to perceive two acute moving directions (or stimuli). Treue *et al.* proposed that the curvature of the time-averaged neuronal activity profile also contains information about the multiplicity of the external stimulus [37]. If there are two moving directions perceived, the resulting neuronal activity profile will be different from that for single moving directions. For differences between two moving directions less than the widths of the tuning curves, the resulting neuronal activity profile will be single peaked and have a wider width, comparing to the profile for single directions, similar to Figure 6.1(b). By considering that the resulting neuronal activity profile was merged by two bump-shaped neuronal activity profiles corresponding to two individual moving directions, one can decode two moving directions from the neuronal activity profile.

The widening of neuronal activity profiles can be caused by multiple stimuli or uncertainty of a stimulus. Zemel *et al.* proposed distributional population codes (DPC) [39], in which neuronal activities encode the probability distribution of the stimulus. In comparison, our theory is simpler. Also, here, we provide a dynamical picture how the discrimination task is done. Sahani *et al.* proposed that the information is encoded by doubly distributional population codes (DDPC) [40]. In their theory, the population code encodes the distribution of the multiplicity of the stimulus. This theory made it possible to distinguish multiplicity and uncertainty. However, this theory requires uncertainty cells, which are yet to be discovered. On the other hand, Raudies *et al.* reported their study is based on a neural model consisting of three regions: V1, MT and medial superior temporal area (MST) [41]. In this model, the directions are distinguishable is due to feedback circuits between different regions. van Rossum *et al.* proposed a schematic mechanism to enable attractor networks to support two almost overlapped information [42]. In their theory, firing rates of neurons are the maximum of tuning curves corresponding to individual stimulus. In this chapter, I propose a theory that provides a dynamical mechanism to make tuning curves for individual stimulus available.

In this chapter, we propose an encoding scheme to represent multiple stimuli. To implement this encoding scheme, we use a continuous attractor neural network (CANN) model with short-term synaptic depression (STD) to generate the time-averaged neuronal activity comparing to the time-averaged neuronal activity measured by Treue *et al.* in a transparent motion experiment. Braddick *et al.* found that there is a range of differences between two moving directions such that human subjects reported the perceived differences between directions is larger than the true difference [43]. This phenomenon

is known as ‘motion repulsion’. Motion repulsion implies that STD may play a role in enhancing the resolution of the moving directions.

The model we used is given by Eqs. (4.6) and (4.7) on page 25. For my convenience, I restate these equations here:

$$\tau_s \frac{d\tilde{u}}{dt}(x, t) = -\tilde{u}(x, t) + \int dx' \tilde{J}(x, x') p(x', t) \tilde{r}(x', t) + \tilde{I}^{\text{ext}}(x, t) \quad (6.1)$$

$\tilde{u}(x, t)$ is the rescaled neuronal current of neurons at preferred stimulus x and time t . τ_s is the timescale of $\tilde{u}(x, t)$ having an order of magnitude of 1 ms. $\tilde{I}^{\text{ext}}(x, t)$ is the external input corresponding to stimuli. It will be defined in the next section. $\tilde{J}(x, x')$ is the rescaled excitatory between neurons with preferred stimulus x and x' , given by

$$\tilde{J}(x, x') \equiv \frac{1}{\sqrt{2\pi}a} \exp\left(-\frac{|x - x'|^2}{2a^2}\right). \quad (6.2)$$

a is the range of excitatory couplings. $p(x, t)$ is the available fraction of neurotransmitters of presynaptic neurons at preferred stimulus x and time t , governed by

$$\tau_d \frac{dp}{dt}(x, t) = 1 - p(x, t) - \tilde{\beta} p(x, t) r(x, t). \quad (6.3)$$

$\tilde{\beta}$ is the rescaled degree of STD. τ_d is the timescale of $p(x, t)$ having an order of magnitude of 100 ms. Throughout the simulations, we choose $\tau_d/\tau_s = 50$. $\tilde{r}(x, t)$ is the rescaled neuronal activity of neurons at preferred stimulus x and time t , given by

$$\tilde{r}(x, t) = \frac{\tilde{u}(x, t)^2 \Theta[\tilde{u}(x, t)]}{1 + \frac{1}{8\sqrt{2\pi}a} \tilde{k} \int dx' \tilde{u}(x', t)^2 \Theta[\tilde{u}(x', t)]}. \quad (6.4)$$

\tilde{k} is the rescaled divisive inhibition. Θ is the step function. For $\tilde{I}^{\text{ext}} = 0$, $\tilde{k} \in (0, 1]$ and $\tilde{\beta} = 0$, the fixed point solution of $\tilde{r}(x, t)$ is given by

$$\tilde{r}(x) = \tilde{r}_0 \exp\left(-\frac{|x - z|^2}{2a^2}\right), \quad (6.5)$$

where $\tilde{r}_0 = 4 \left(1 + \sqrt{1 - \tilde{k}}\right) / \tilde{k}$. Here, $2a$ is the width of tuning curves of neurons in this model. Since the average tuning width of neurons in MT is found to be 96° [37], I let $2a = 96\pi/180$.

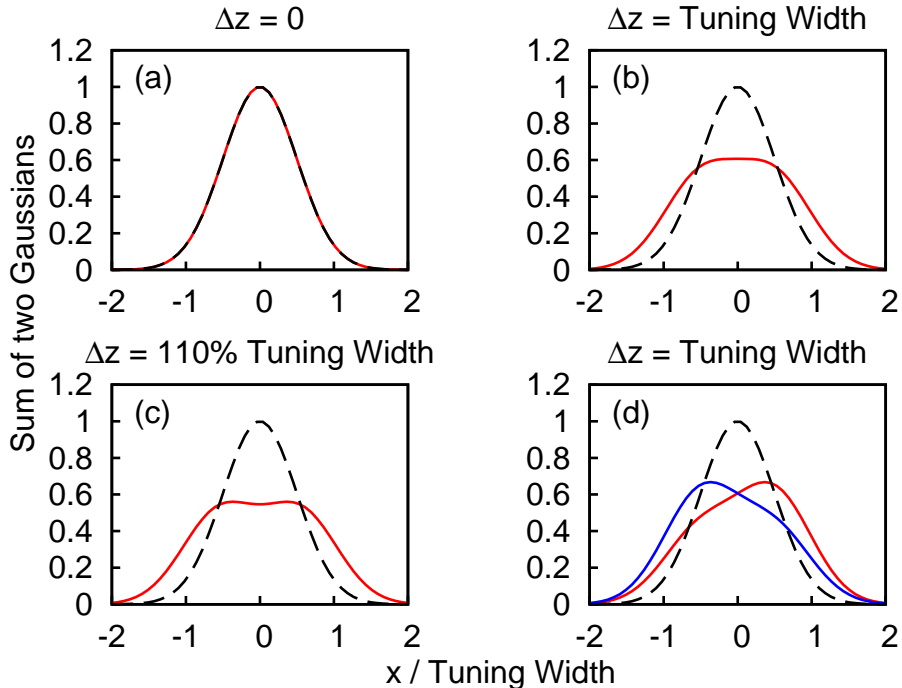


Figure 6.1: (a) - (c) The profile of two superposed Gaussian functions with the same height. $f(x) \equiv \{\exp[(x - \Delta z/2)^2/(2a^2)] + \exp[(x + \Delta z/2)^2/(2a^2)]\}/2$. Red solid line: $y = f(x)$ with different Δz . Dashed line: $y = f(x)$ with $\Delta z = 0$ as a reference. (a) $\Delta z = 0$. (b) $\Delta z = \text{tuning width} = 2a$. (c) $\Delta z = 110\% \text{ tuning width} = 2.2a$. (d) The profile of two superposed Gaussian functions with different heights to illustrate how the amplitude fluctuations provide a cue to distinguish the components. $g(x) \equiv \{A_0 \exp[(x - \Delta z/2)^2/(2a^2)] + A_1 \exp[(x + \Delta z/2)^2/(2a^2)]\}$. Dashed line: $y = f(x)$ with $\Delta z = 0$ as a reference. Red solid line: $y = g(x)$ with $\Delta z = \text{tuning width}$, $A_0 = 0.4$ and $A_1 = 0.6$. Blue solid line: $y = g(x)$ with $\Delta z = \text{tuning width}$, $A_0 = 0.6$ and $A_1 = 0.4$.

6.2 Input with Fluctuations

Consider an external input \tilde{I}^{ext} corresponding to multiple stimuli (or moving directions).

Let

$$\tilde{I}_0^{\text{ext}}(x, t) = \sum_{i=1}^n \left[\tilde{A}_0 + \delta\tilde{A}_i(t) \right] \exp\left(-\frac{|x - z_i|^2}{2a_I^2}\right). \quad (6.6)$$

\tilde{A}_0 is the relative magnitude of each component corresponding to each stimulus z_i . $\delta\tilde{A}_i$ is the fluctuation of each component. $2a_I$ is the width of each Gaussian. These fluctuations are independent of each other. $\langle \delta\tilde{A}_i \delta\tilde{A}_j \rangle = \sigma^2 \tilde{A}_0^2 \delta_{ij}$. In our simulations, we updated $\delta\tilde{A}_i$ every $50\tau_s$. For $n = 2$ and $\delta\tilde{A}_i = 0$, the net profile of $\tilde{I}_0^{\text{ext}}(x, t)$ will be single-peaked if their separation is less than the tuning width. As illustrated in Figures 6.1(a) - (c), if there is no fluctuation, the profile of $\tilde{I}_0^{\text{ext}}(x, t)$ will be single-peaked for $0 \leq |z_0 - z_1| \leq$ tuning width. Based on Eq. (2.13), a single-peaked symmetric $\tilde{I}_0^{\text{ext}}(x, t)$ is effectively the same as the case with $n = 1$. Figure 6.1(d) shows that if there is a fluctuation, the symmetry of the profile will be broken. As a result, it will be different from that without fluctuations. This is consistent with the psychophysical experiment which showed that spatial and temporal randomness is important for perception of motion transparency [44].

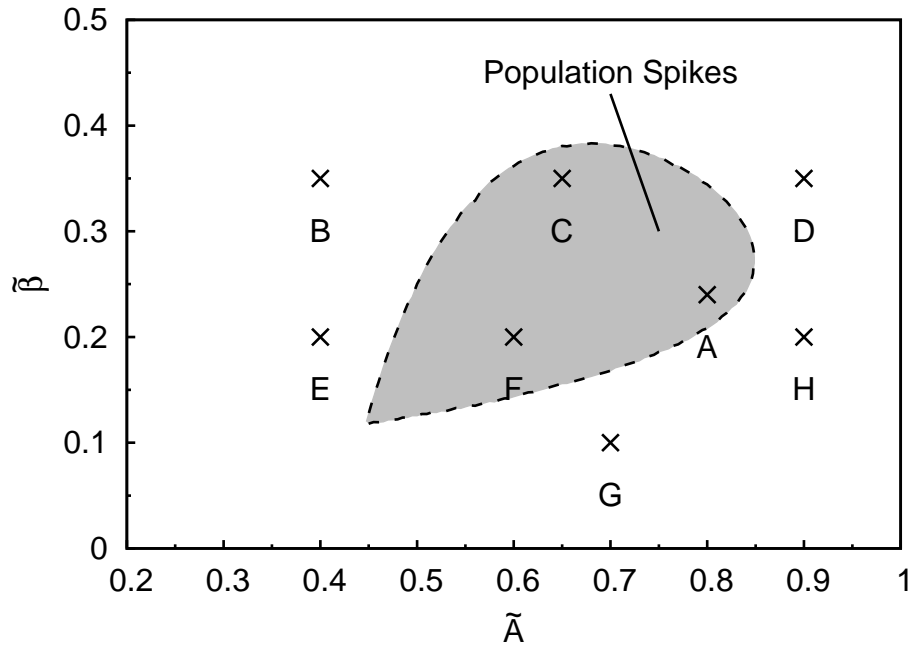


Figure 6.2: The shaded region is the parameter region for $\tilde{k} = 0.5$ and $n = 1$ in Eq. (6.6) to achieve population spike. Cross: particular cases to be discussed in this chapter. $\tau_d/\tau_s = 50$. The boundary is provided by Wang [45]. Points B to H correspond to cases in Figure 6.8. Point A is the case I used to illustrate the theory in Figures 6.3 - 6.7.

The external input used in Eq. (6.1) is given by

$$\tilde{I}^{\text{ext}}(x, t) = \frac{\tilde{A}}{\max_x [\tilde{I}_0^{\text{ext}}(x, t)]} \tilde{I}_0^{\text{ext}}(x, t). \quad (6.7)$$

\tilde{A} is the absolute strength of the external input. By using this definition of the external input, the magnitude of \tilde{I}^{ext} will be independent of the differences between stimuli and the number of stimuli.

6.3 Population Spikes

For the case with a single stimulus, i.e. $n = 1$ in Eq. (6.6), there is a parameter region over the parameter space spanned by \tilde{k} , $\tilde{\beta}$ and \tilde{A} such that the CANN with STD can support a series of periodic excitement of neuronal activities. The periodic excitement of neuronal activities is due to the fact that the dynamics of a CANN with STD is influenced by dynamical variables with two time scales.

In Figure 6.2, there is a shaded region corresponding to the occurrence of the periodic excitement of neuronal activities. Here, we name the periodic excitement the *population spikes*. To have a better illustration, I have chosen three cases with same \tilde{k} and $\tilde{\beta}$, but different \tilde{A} 's, as shown in Figure 6.3. In the figure, for $\tilde{A} = 0.4$, since the magnitude of the external input is relatively small, the network is not excited to a state with high firing rate. Neurotransmitters in the region that neurons are relatively active are not significantly consumed. In this case, there is no population spike. For $\tilde{A} = 2.0$, the external input is strong enough to excite the network to a relatively high firing rate. Neurotransmitters of active presynaptic neurons are significantly consumed. Since the external input is strong enough, the network state cannot drop to relatively a low level. If the strength of the external input is moderate, $\tilde{A} = 0.8$, the network can be excited to a relatively high state, while the external input cannot solely support the network state. So, population spikes can happen. Maxima of $\tilde{r}(x, t)$ and minima of $p(x, t)$ for all z are plotted as functions of t in Figure 6.4. Here we can see that the period of population spikes is of the order of the magnitude of τ_d . Also, we can see how $p(x, t)$ correlate to $\tilde{r}(x, t)$. For example, the valley of $\min_x p(x, t)$ is always occurring at a time after the peak of $\max_x \tilde{r}(x, t)$.

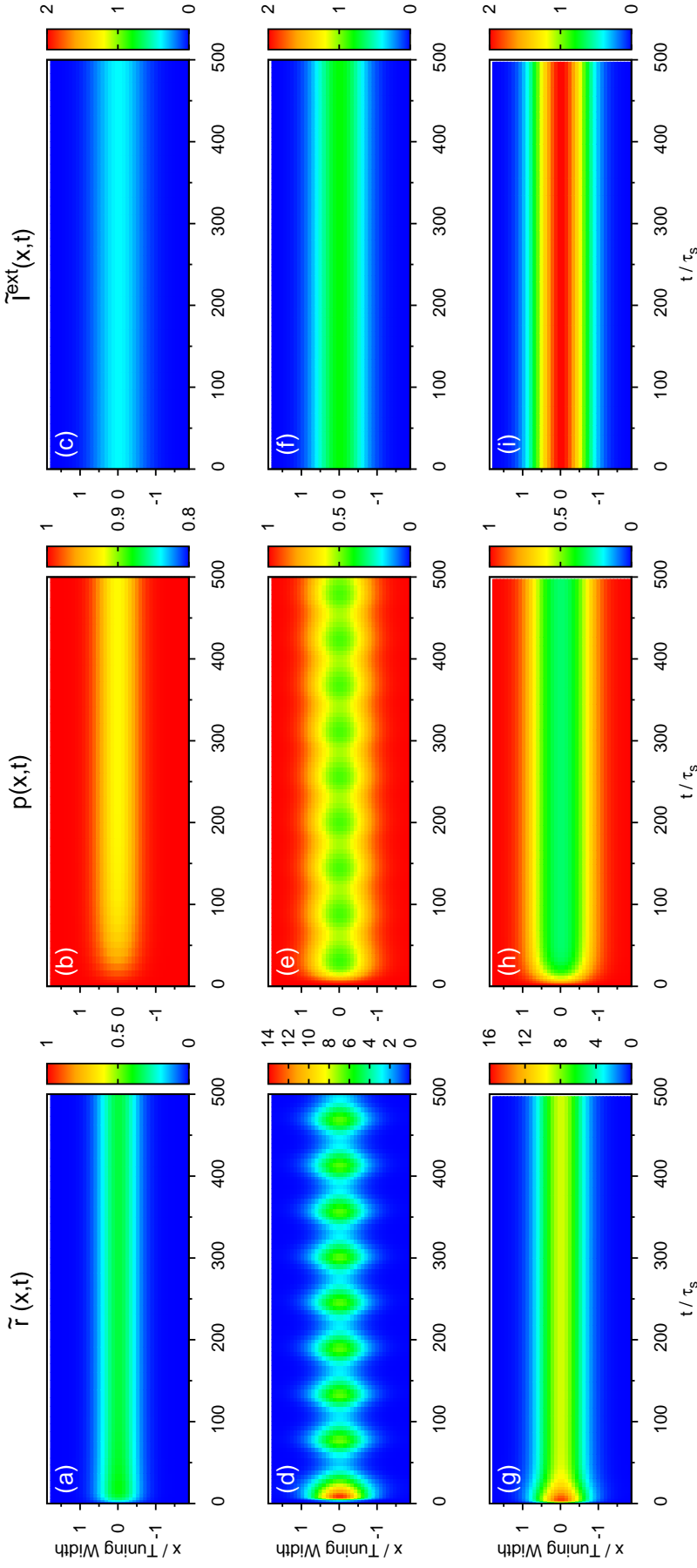


Figure 6.3: Firing rates $\tilde{r}(x, t)$ ((a), (d) and (g)), available fraction of neurotransmitters $p(x, t)$ ((b), (e) and (h)) and corresponding input ((c), (f) and (i)) for various magnitudes of single-peaked external inputs. (a)-(c) $\tilde{A} = 0.4$, (d)-(f) $\tilde{A} = 0.8$ and (g)-(i) $\tilde{A} = 2.0$. Other parameters: $k = 0.5$, $\tilde{\beta} = 0.24$, $a = 48\pi/180$ and $\tau_d = 50\tau_s$.

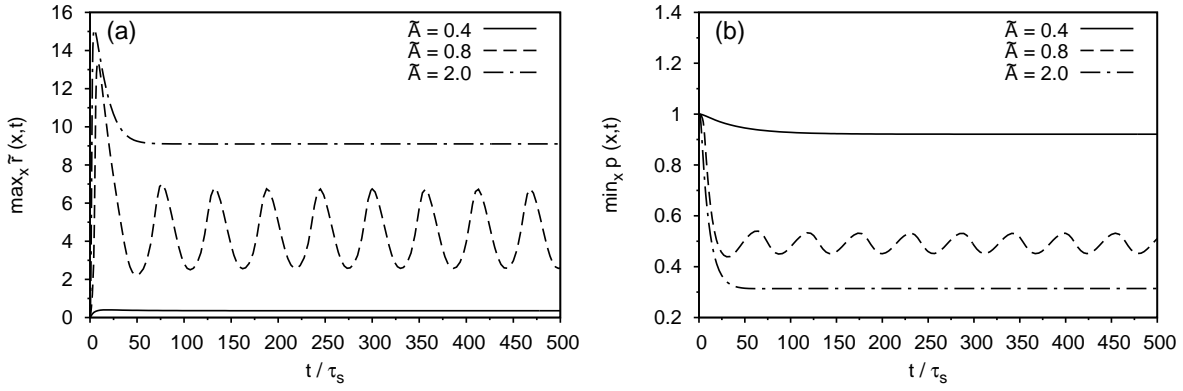


Figure 6.4: (a) $\max_x \tilde{r}(x,t)$ as a function of t corresponding to Figures 6.3(a), (d) and (g). (b) $\min_x p(x,t)$ as a function of t corresponding to Figure 6.3(b), (e) and (h). Parameters: the same as Figure 6.3.

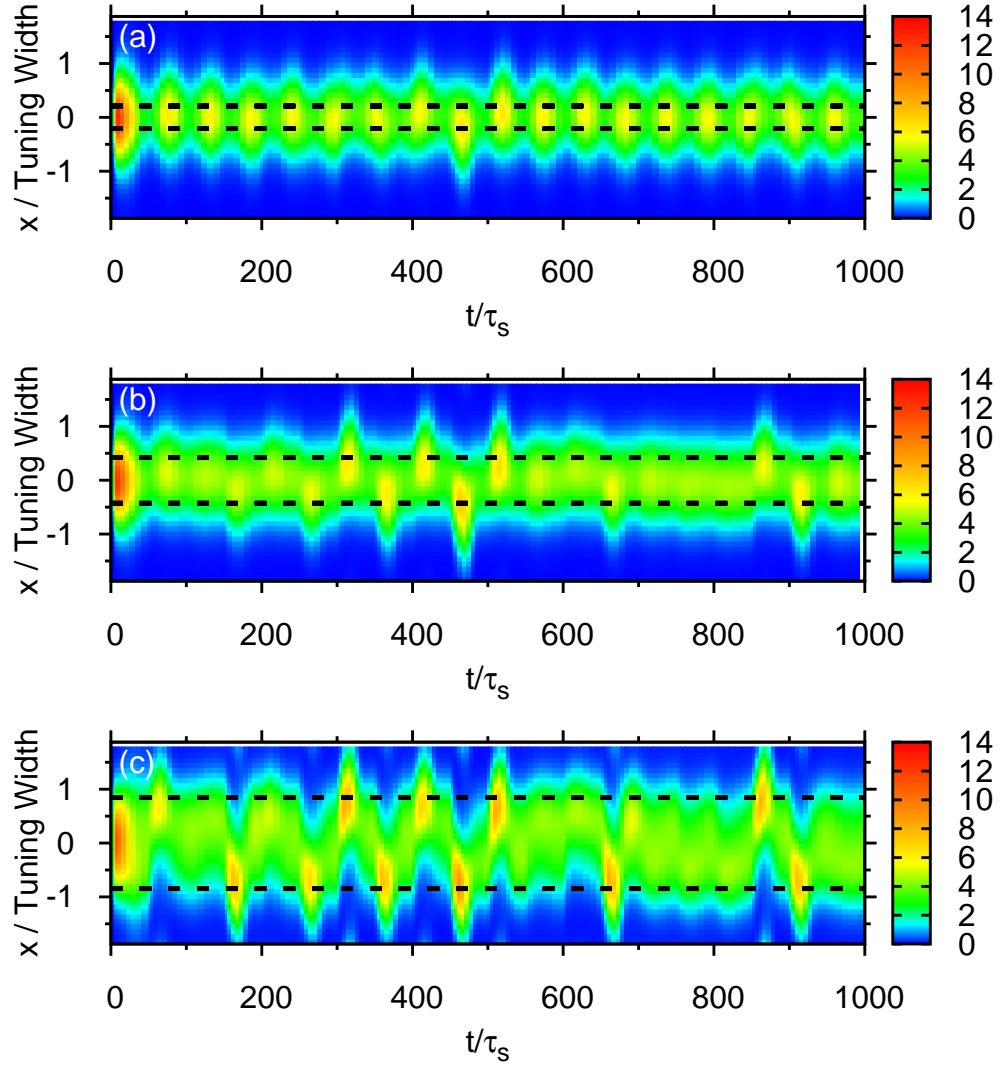


Figure 6.5: Raster plot of firing rates \tilde{r} for (a) $\Delta z = 0.5$, (b) $\Delta z = 1.0$ and (c) $\Delta z = 2.0$. Black dashed lines: positions of stimuli. Parameters: $\tilde{k} = 0.5$, $\tilde{\beta} = 0.24$, $a = 48\pi/180$, $\tilde{A} = 0.8$, $\sigma = 0.3$ and $\tau_d = 50\tau_s$.

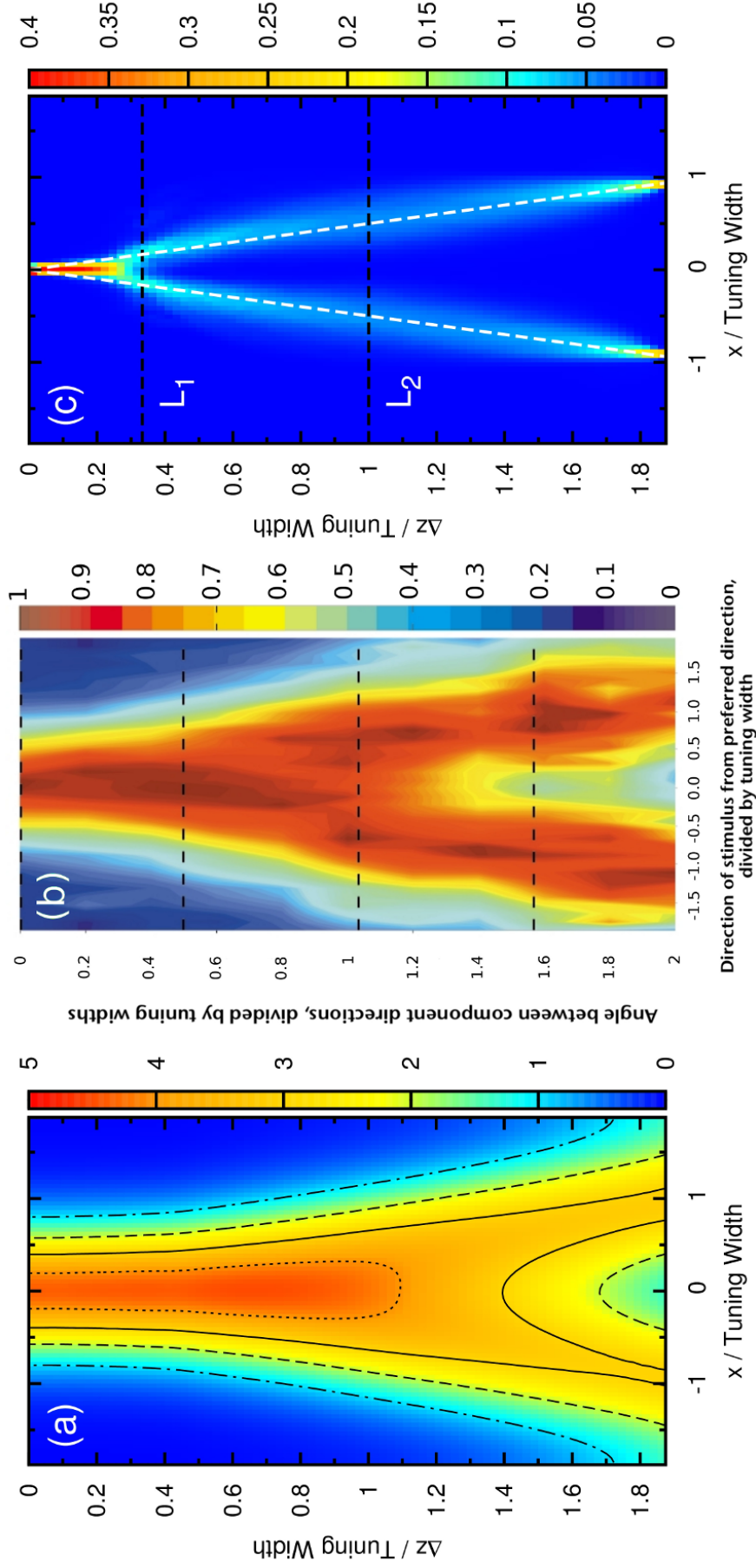


Figure 6.6: (a) Time average of firing rates \tilde{r} as a function of the preferred stimuli x , and the separation between the two stimuli, Δz . Contour lines: $\langle \tilde{r} \rangle_t = 1$ (dotted-dashed line), $\langle \tilde{r} \rangle_t = 2$ (dashed line), $\langle \tilde{r} \rangle_t = 3$ (solid line), $\langle \tilde{r} \rangle_t = 4$ (dotted line). Parameters: same as Figure 6.5. (b) The average neural activity recorded by Treue *et al.* in [37] (with license number 3178600066018 for the reuse purpose). (c) Contours of the distribution of peak positions higher than 6.2 as a function of preferred stimuli, x , and the separation between the two stimuli, Δz . White dashed line: positions of the two stimuli. L_1 : one-third of the tuning width. L_2 : tuning width. Parameters: same as Figure 6.5.

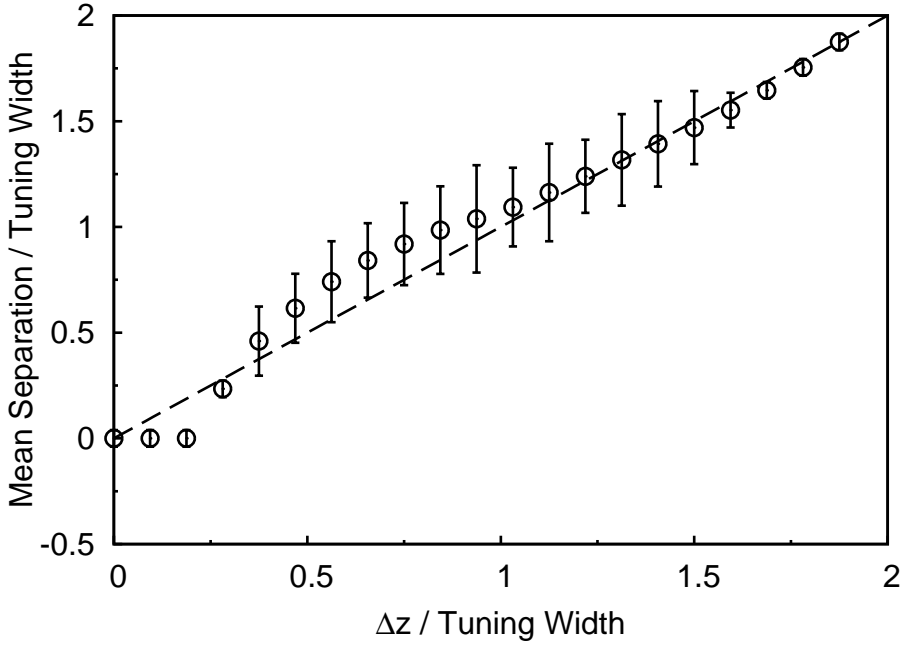


Figure 6.7: The mean separation of peak positions of $\tilde{r}(x, t)$ shown in Figure 6.6(c). Symbols: simulation. Dashed line: diagonal line representing perfect distinguishability.

6.4 Temporal Modulation as a Strategy to Represent Overlapped Information

Using parameters within the parameter region of population spikes in Figure 6.2, I have shown that one can generate periodic excitements of neuronal activities of the network. For an external input containing two independently fluctuating components corresponding to two stimuli, the network can respond to individual stimuli. In the case with two stimuli, we define the separation between two stimuli to be $\Delta z \equiv z_1 - z_0$. For simplicity, we let $z_0 = -0.5\Delta z$ and $z_1 = 0.5\Delta z$. In Figure 6.5, there are three Δz 's: $\Delta z = 0.5$, $\Delta z = 1.0$ and $\Delta z = 2.0$. In Figure 6.5(a), the difference between stimuli is small. However, due to fluctuations on each components, the behavior of the population spike is different from that in Figure 6.3(d), as the peak positions of population spikes are not at the same any more. Also, sometimes, the peak positions are not at $x = 0$. For a larger $\Delta z = 1.0$, the temporal series of the neuronal activity is significantly different from that in Figure 6.3(d). Population spikes are found to form two groups. Each group of population spikes corresponds to one stimuli. For an even larger $\Delta z = 2.0$, as shown in Figure 6.5(c), there are clearly two groups of population spikes. I have plotted the time-averaged neuronal activity profile in Figure 6.6(a) for a range of Δz . This result is highly comparable to the result reported by Treue *et al.* in [37], as shown in Figure 6.6(b). In the plot, we can see that the average neuronal activity profile split

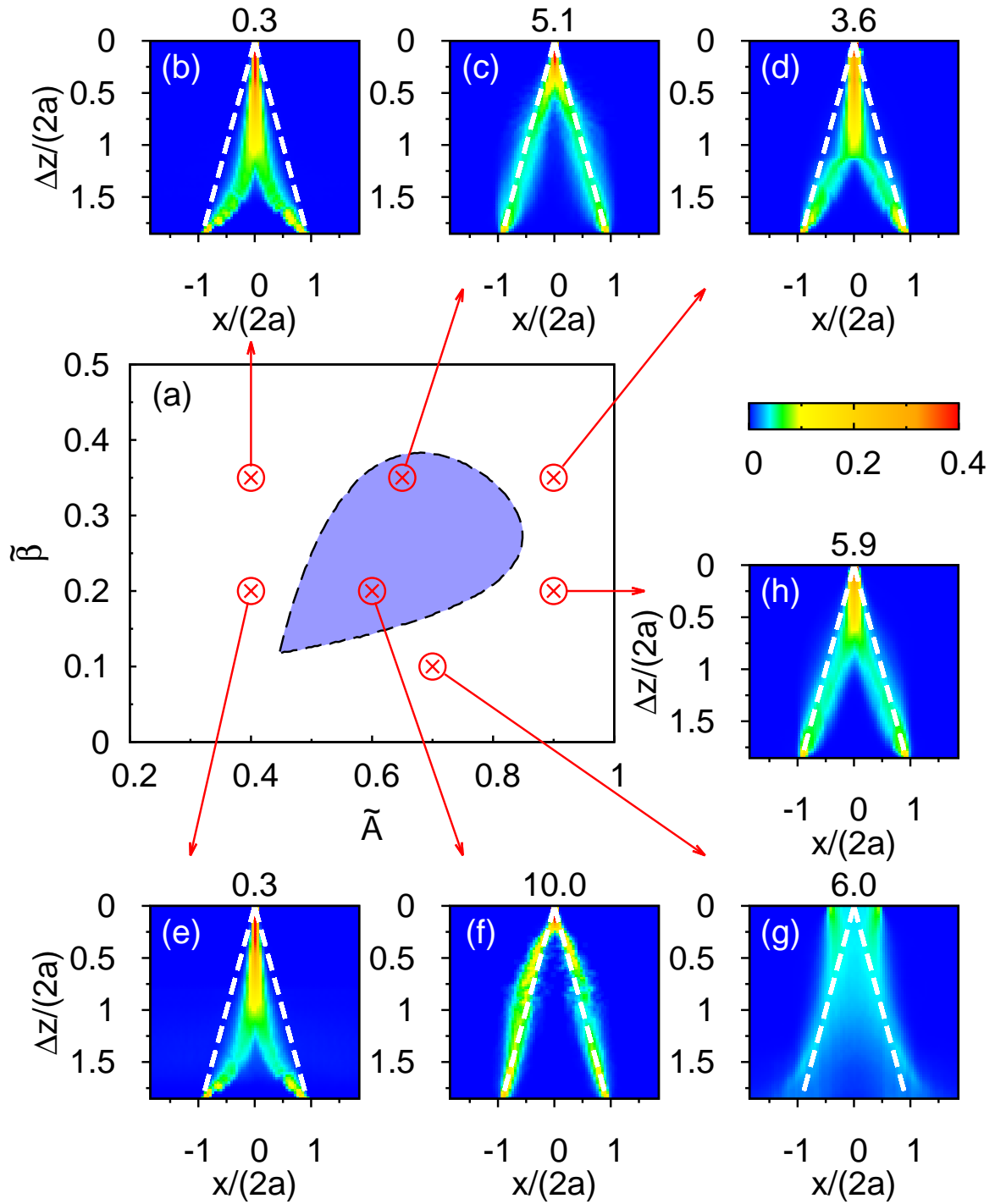


Figure 6.8: (a) The phase diagram of population spikes over the parameter space spanned by $(\tilde{A}, \tilde{\beta})$ with the parameter $\tilde{k} = 0.5$ and $\tau_d/\tau_s = 50$. (b) - (h) are distributions of the occurrence of peak positions as function of Δz . The numbers at the top of (b) - (h) are thresholds used to sample peak positions. Parameters: (b) $\tilde{A} = 0.4$ and $\tilde{\beta} = 0.35$. (c) $\tilde{A} = 0.65$ and $\tilde{\beta} = 0.35$. (d) $\tilde{A} = 0.9$ and $\tilde{\beta} = 0.35$. (e) $\tilde{A} = 0.4$ and $\tilde{\beta} = 0.2$. (f) $\tilde{A} = 0.6$ and $\tilde{\beta} = 0.2$. (g) $\tilde{A} = 0.7$ and $\tilde{\beta} = 0.1$. (h) $\tilde{A} = 0.9$ and $\tilde{\beta} = 0.2$.

for $\Delta z >$ tuning width.

In Figure 6.5, I have shown that multiple fluctuating stimuli can cause a temporal modulation on the population spike pattern similar to that shown in Figure 6.3(d). We propose that these temporally modulated neuronal activity profiles contain information about the components of multiple stimuli. Also, the information contained by a temporal modulated neuronal activity profile can be easily extracted.

I will propose a way to decode the information encoded by the temporally modulated neuronal activity profile. The proposed method is not the only way to implement the decoding process. Also, the proposed way may not be the best implementation. However, this is easy for biological systems. Let us consider the occurrence of population spike as a function of preferred stimuli of neurons, x . I count only population spikes with height higher than a threshold θ , and divide the manifold $[-\pi, \pi)$ into 80 bins. For each Δz , For each instant of time with spike rates above the threshold, I count the occurrence of population spikes as a function of time and preferred stimulus. The location of each population spike is measured by their center of mass. Figure 6.6(c) is the result of the statistics for $500000\tau_s$. A long sampling period is needed to obtain a smooth distribution in Figure 6.6(c). However, a sampling period of the order of $1000\tau_s$ is good enough to get a distribution to perform discrimination tasks [35]. In the raster plot, each row is a histogram for the corresponding Δz . The frequency of the occurrence of each bin is normalized. So, for each row, the histogram can be added to unity. In Figure 6.6(c), we can see that by measuring the occurrence of peak positions of population spikes, one can extract the information of each stimulus contained in the external input. For the time-averaged neuronal activity profile, one can distinguish two stimuli only when the true difference between two stimuli is larger than the tuning width of neurons. However, if one uses the occurrence of peak positions of population spikes to decode the information, two stimuli can be distinguished, even when the true difference between two stimuli is as small as one-third tuning width of neurons.

Apart from the time-averaged neuronal activity profile, the behavior of perceived differences between two stimuli is also similar to the experiment. Braddick *et al.* found that in their transparent motion experiment, subjects overestimated the difference between two moving directions, if differences between two moving directions are between about 30° to 120° [43]. This phenomenon is called ‘motion repulsion’. In Figure 6.6(c), for $1/3 \leq \Delta z/a \leq 1$, peaks of histograms are in the outer region delineated by the two white dashed lines labeling true positions of two stimuli. If we measure positions of two stimuli from histograms, we can have a result similar to that of Braddick *et al.* In Figure 6.7, if we let $2a = 96^\circ$, the region that the network overestimates the difference between

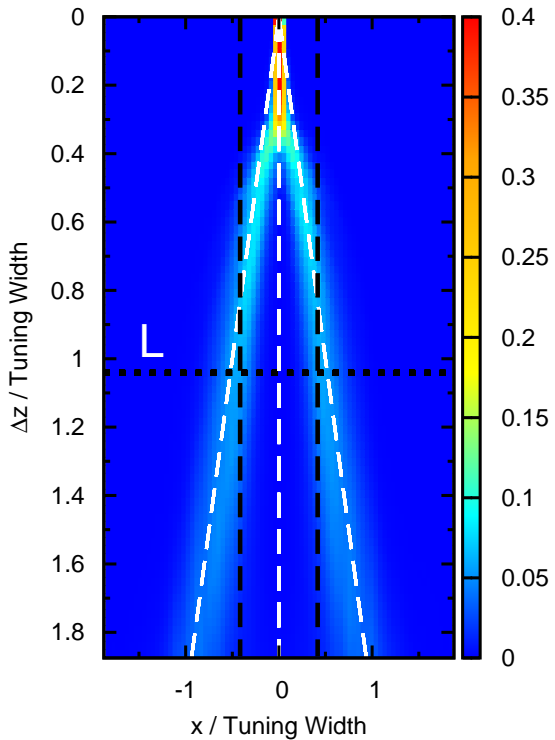


Figure 6.9: Contours of the distribution of peak positions higher than 6.2 as a function of preferred stimuli, x , and the separation between the two outermost stimuli, Δz , in the case of three equally strong stimuli. White dashed line: positions of three stimuli. Horizontal dotted line: the case comparable to the three-stimulus experiment reported by Treue *et al.* [37]. Vertical dashed lines: perception ($\pm 40^\circ$) reported by subjects in the experiment in units of the tuning width (96°). Parameters: same as Figure 6.3.

two stimuli matches the region measured by Braddick *et al.*

We have also tested the model with other parameters. The parameter set I presented right above is the point A in Figure 6.2. For points B - H, the result is shown in Figure 6.8. In Figures 6.8(b), (d), (e) and (h), because there is no population spike, we cannot decode the information using the center of mass of the neuronal activity profile. In Figures 6.8(c) and (f), because of population spikes, we can use the peak positions to determine the information contained in the neuronal activities. For Figure 6.8(g), the network state is highly mobile. The state of the network is called *slosher* [45]. There are two peaks even for $\Delta z = 0$. Since the network is too sensitive, this parameter set is not suitable for discrimination tasks.

For external inputs with three stimuli, we found that the behavior of the network is also similar to the result reported by Treue *et al.* Treue *et al.* reported that, if there are three moving directions, subjects reported that there are just two directions. Also, the perceived difference between directions is less than the difference between two outermost directions. The result from our model is plotted in Figure 6.9. For moving directions at -50° , 0° and 50° , our model can only perceive two moving directions. Also, the two perceived moving directions underestimated the true difference between two outermost stimuli (i.e. -50° and 50°).

6.5 Conditions of the Theory

To implement the model we proposed above, there are several conditions on the continuous attractor neural network. The first condition to implement the above theory is the STD. In Figure 6.10(a), the continuous attractor neural network does not have short-term synaptic depression. In this case, there are two stimuli. However, since there is no STD, there are no population spikes. Without population spikes, the neuronal activity profile cannot shift from one stimulus to another, especially for $\Delta z > 2a$. So, CANN without STD cannot implement discrimination tasks. Some other mechanisms similar to STD may also replace STD in our theory.

To obtain results comparable to the experiment by Braddick *et al.*, we also need STD. Based on this model, we proposed that the ‘motion reulsion’ can be explained by the effect of STD. In Figure 6.11, there is a plot of time-averaged $p(x, t)$. Due to the neuronal activities, $p(x, t)$ has a valley centered at the center of two stimuli. As a result, the outer region delineated by two stimuli has relatively stronger synaptic efficacies than region between two stimuli. Population spikes appear more likely in the outer region. So, in a range of Δz , the perceived difference between two stimuli is larger than the true difference.

An appropriate strength of the external input is also important to the phenomenon. I have shown that in Figure 6.8. If \tilde{A} is too small or too large, the population spike cannot occur. As a result, the discrimination task cannot be done. Also, if \tilde{A} is even smaller, the external input cannot pin the neuronal activities near the stimuli. In Figure 6.10(b), the neuronal activity profile can move spontaneously due to the translational instability provided by STD and a weak external input.

In our model, inputs without fluctuations can make the discrimination task difficult. This idea is similar to the experimental result reported by Qian *et al.* [44]. In Figure 6.10(c), the input of the CANN has no fluctuations. In this case, the network will be single-peaked. So, we cannot use centers of mass of neuronal activity profiles to decode information contained in the external input. So, fluctuations of the external input is important to the discrimination task.

As shown in the previous section, decoding the information from the neuronal activity profile requires thresholding. In Figure 6.10(d), the statistics is done without a threshold, i.e. $\theta = 0$. Without a threshold, the histogram begins to split into two branches only when $\Delta z > 2a$. This does not agree with experimental results. So, thresholds should be required for discrimination tasks.

6.6 Robustness and Biological Relevance

One may query the robustness of the theory, because the result we presented above depends strongly on the choice of stimulus amplitudes, STD strengths and thresholds. We remark that although the threshold is tuned for each plot in Figure 6.8, there is also a range of stimulus amplitudes, STD strengths and thresholds achieving similar results [35, 45]. Furthermore, it is common in biology that animals can acquire the appropriate parameter region through learning and/or evolution.

In our theory, it seems that the phenomenon requires the magnitudes of each stimulus to be the same. However, we observe that the effect is tolerant to a range of difference in stimulus strength in our further studies. The ratio between magnitudes of stimuli can be as large as 1.5 in our simulations.

For the flexibility of the model, I would like to emphasize the key point of my work. The main theme of my model is how periodic excitements of the neuronal activity can be engaged in the encoding process and its advantages in enhancing the information processing capability. While the use of periodic excitements of neuronal activity in neural computation has been suggested long time ago (see, for example, Loebel *et al.* [46]), no concrete examples have been proposed. Our work shows that temporal modulations of neuronal activities contain more information, filling in this long awaited gap. Focusing on the main point of the enhanced information encoded by temporal modulations, we consider thresholding as a simple decoding scheme to show that the temporally modulated neuronal activity is decodable, but other more complicated decoding schemes can serve the same illustrative purpose. For example, an extra network with an inhibition having longer timescale can produce the same effects.

Concerning evidence of periodic excitements in the neuronal activity, we cite experimental results showing that neuronal oscillations are found in the middle temporal area. For example, Ergenoglu *et al.* [47] reported that alpha rhythms can be found in the visual cortex during tasks. Mantini *et al.* [48] found that the alpha rhythm is the major component of the neural oscillations in the middle temporal area. Since the frequency of alpha rhythms is close to the frequency of the periodic excitements in our model, dynamical synapses can be a possible mechanism of the neural oscillators found in the experiments. Future experiments should be designed to monitor whether these bursts are particularly strong when subjects are involved in tasks of differentiating narrowly separated directions.

6.7 Summary

Continuous attractor neural networks (CANNs) with short-term synaptic depression (STD) can implement a mechanism to perform discrimination tasks to distinguish two overlapped stimuli. Using appropriate parameters, the neural network can generate results comparable to experimental results. For example, the time-averaged neuronal activities of the neural network are similar to those measured by Treue *et al.* [37]. The minimum separation between two stimuli can be distinguished by our model is roughly one-third of tuning width of the neurons. Also, the perceived separation between two stimuli in our model has a similar behavior to that reported Braddick *et al.* The range of separations between two stimuli having ‘motion reulsion’ behavior is similar to that measured by Braddick *et al.* [43].

I have also tested the case that an external input contains three stimuli. The behavior is again comparable to the behavior described by Treue *et al.* [37]. In the simulation, our model can perceive two stimuli instead of three, which is the same as the experimental result. Also, the perceived separation between two stimuli is less than the true difference between the two outermost stimuli.

In this chapter, I have shown that short-term synaptic depression (STD) can help the continuous attractor neural network (CANN) to achieve the goal. The key is the population spike. Population spikes enable the neuronal activity profile to shift from one stimulus to another. An external input with appropriate strength, fluctuations on the external input and thresholding are important factors contributing to the enhancement of resolution.

The resolution enhancement due to fluctuations is similar to the stochastic resonance mechanism proposed by Simonotto *et al.* [49]. In their psychophysics experiment, the perception of images can be improved by time varying noise, while our model provides a neural mechanism of how noises can improve visual perception. In the theory proposed by Simonotto *et al.* the visual information is effectively at the subthreshold level so that perceiving the stimulus is impossible. After the addition of noise with an appropriate magnitude, the visual information originally at the subthreshold level becomes superthreshold so that subjects can perceive the visual stimulus. Although our theory and their experiment are not directly related, temporal modulation of neuronal activity profile can point to a new direction how noise and fluctuation can improve the visual perception. As neurons are discrete units, the attractor space is not completely smooth. Low noise can help the network state to overcome low barriers so that the attractor space is effectively smooth even for a population of neurons.

One could observe that the magnitude of STD used here is significantly larger than that in the previous chapter. Here, we argue that the parameters in different regions of the brain should be differently tuned to satisfy different functions. It is widely believed that different brain regions correspond to different brain functions. However, a specific brain function requires some particular brain properties. The brain region concerned in this chapter is different from those in the previous chapter. So, it is natural that the parameters used in these two chapters are different.

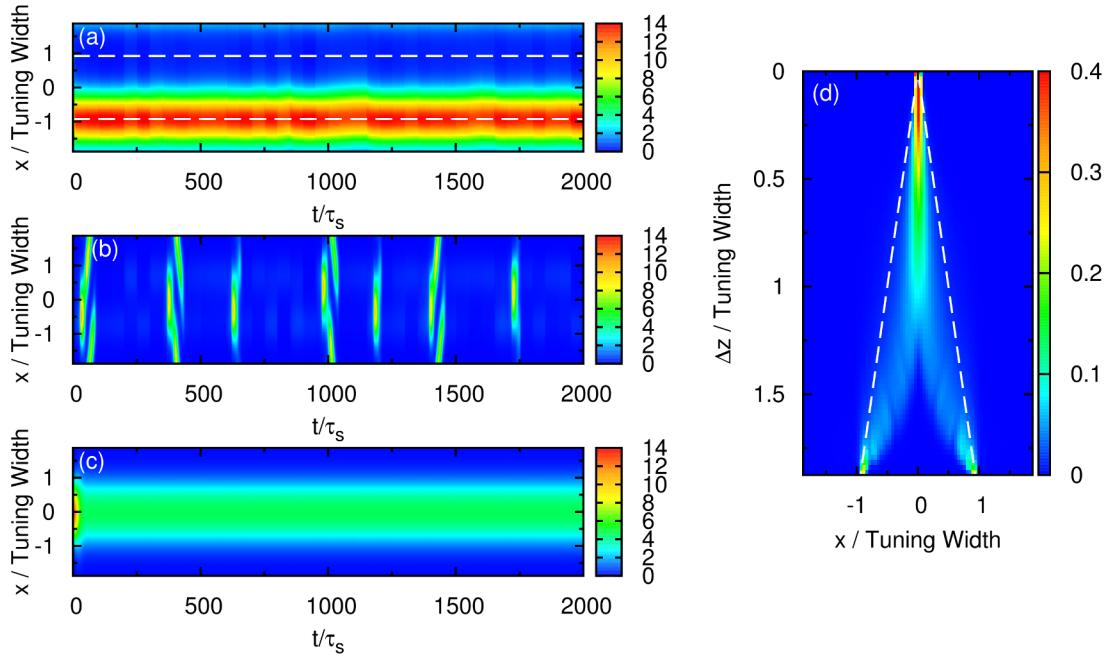


Figure 6.10: (a) Raster plot of firing rate \tilde{r} of the network with two stimuli and without STD. Parameters: $\tilde{k} = 0.5$, $\tilde{\beta} = 0$, $\tilde{A} = 0.8$, $a = 48\pi/180$, $\sigma = 0.3$ and $\Delta z = 3.1$. (b) Raster plot of firing rate \tilde{r} of the network with two stimuli with weak net input profile. Parameters: $\tilde{k} = 0.5$, $\tilde{\beta} = 0.24$, $\tilde{A} = 0.4$, $a = 48\pi/180$, $\sigma = 0.3$ and $\Delta z = 2.5$. (c) Raster plot of firing rate \tilde{r} of the network with two stimuli without height fluctuations in the external input profile. Parameters: $\tilde{k} = 0.5$, $\tilde{\beta} = 0.24$, $\tilde{A} = 0.8$, $a = 48\pi/180$, $\sigma = 0$ and $\Delta z = 1.67$. (d) Contours of the distribution of peak positions for all peak heights. White dashed line: positions of the two stimulus components. Parameters: $\tilde{k} = 0.5$, $\tilde{\beta} = 0.24$, $\tilde{A} = 0.8$, $a = 48\pi/180$, $\sigma = 0.3$ and $\Delta z = 1.0$.

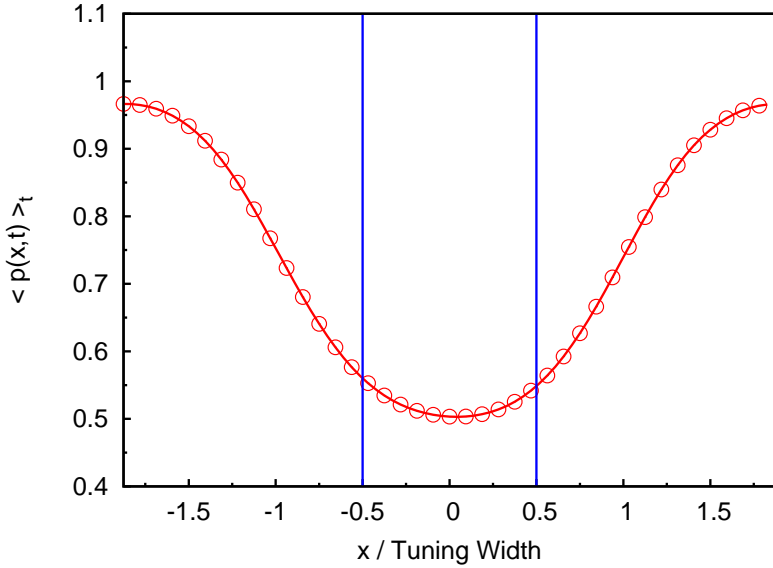


Figure 6.11: The time-averaged dynamical variable $p(x,t)$. Symbols and red line: measurement from the simulation. Blue lines: positions of two stimuli. Parameters: $\tilde{k} = 0.5$, $\tilde{\beta} = 0.24$, $a = 48\pi/180$, $\tau_d/\tau_s = 50$, $\tilde{A} = 0.8$, $\sigma = 0.3$ and $\Delta z = \text{tuning width of attractor states}$.

Chapter 7

Two-dimensional Continuous Attractor Neural Networks with Synaptic Depression and Local Subtractive Inhibition¹

7.1 Introduction

This is the last chapter before the concluding chapter. Unlike the previous two chapters about the implications of one-dimensional continuous attractor neural networks (CANNs) with short-term synaptic depression (STD), this chapter will focus on the intrinsic dynamics of two-dimensional continuous attractor neural networks (2D CANNs) with short-term synaptic depression (STD) and local subtractive inhibition.

Studies of CANNs with short-term synaptic depression were mainly on 1D networks, but the dynamics of 2D CANNs should also be important. O’Keefe reported that place fields of some neurons in the hippocampus of a rat is a two-dimensional localized profile [11]. We have also studied a 2D version of the model we presented in Chapter 2 [22]. In the study, we have employed the perturbative method to analyze the stability of the fixed point solution and the tracking dynamics.

In this chapter, we discuss the intrinsic dynamics of bump-shaped solutions of two-dimensional CANNs with short-term synaptic depression. The 2D model possesses rich dynamical behavior such as spiral waves [50], breathing pulses [50] and various scattering scenarios during the collision of two bump-shaped profiles [51]. Here, we focus on the spontaneous motion of single bump-shaped profile, and analyze its stability. It is necessary to study the instability of a bump not only in its size, but also in a change in

¹The work is collaborated with S. Amari (Affiliation: Brain Science Institute, RIKEN, Saitama, Japan).

its wave stability.

We study not only CANNs with STD and global divisive inhibition, but also CANNs with local subtractive inhibition. Local subtractive inhibition can also destabilize static bumps in amplitude or in position. Similar to that found in the case with STD and global divisive inhibition, local inhibition destabilizes the translational mode first, and then the amplitude. There is a parameter region such that both a spontaneous moving bump solution and a static solution can coexist.

In this chapter, in each case: CANNs with STD and CANNs with local subtractive inhibition, we first introduce a model we used to study the problem. After that, we analyze these scenarios using the perturbative method introduced in Chapter 3. Then, there will be a discussion section comparing the theoretical and simulation results, and the limitation of the perturbative method.

7.2 Two-dimensional Continuous Attractor Neural Networks with Synaptic Depression and Global Inhibition

7.2.1 The Model

Let us consider a 2D neural field, where neurons are located on a 2D field with positional coordinates $\mathbf{x} = (x_1, x_2)$. The state of a neural field is specified by the average membrane potential $u(\mathbf{x}, t)$ of neurons at \mathbf{x} at time t . The neuronal activity of neurons at \mathbf{x} is given by a nonlinear function of $u(\mathbf{x}, t)$,

$$r(\mathbf{x}, t) = \frac{u(\mathbf{x}, t)^2}{B(t)} \Theta[u(\mathbf{x}, t)], \quad (7.1)$$

where Θ is the step function and $B(t)$ is the total activity of the field which gives the divisive global inhibition. The neuronal activity is related to the average firing rate of the neuron. The evolution of the global inhibition is given by

$$\tau_B \frac{dB(t)}{dt} = -B(t) + 1 + \rho k \int d\mathbf{x}' u(\mathbf{x}', t)^2. \quad (7.2)$$

k is the parameter controlling the strength of the divisive global inhibition. Here, we consider the dynamics of $B(t)$ separately to model the inhibitory effect provided by an

inhibitory neuron having time scale τ_B . ρ is the density of neurons over the field. Neurons are connected by excitatory couplings given by

$$J(|\mathbf{x} - \mathbf{x}'|) = \frac{J_0}{2\pi a^2} \exp\left(-\frac{|\mathbf{x} - \mathbf{x}'|^2}{2a^2}\right). \quad (7.3)$$

Here a shows the range of effective excitatory connections and J_0 is the intensity of average coupling over the field. The dynamics of $u(\mathbf{x}, t)$ is governed by

$$\tau_s \frac{\partial u(\mathbf{x}, t)}{\partial t} = -u(\mathbf{x}, t) + \rho \int d\mathbf{x}' J(|\mathbf{x} - \mathbf{x}'|) p(\mathbf{x}', t) r(\mathbf{x}', t) + I^{\text{ext}}(\mathbf{x}, t). \quad (7.4)$$

$I^{\text{ext}}(\mathbf{x}, t)$ is an external stimulus and $p(\mathbf{x}, t)$ is the available fraction of neurotransmitters of the presynaptic neuron. The dynamics of $p(\mathbf{x}, t)$ evolves as

$$\tau_d \frac{\partial p(\mathbf{x}, t)}{\partial t} = -p(\mathbf{x}, t) + 1 - \tau_d \beta p(\mathbf{x}, t) r(\mathbf{x}, t). \quad (7.5)$$

The first two terms are the relaxation of $p(\mathbf{x}, t)$ with time constant τ_d . The last term is the consumption of neurotransmitters.

7.2.2 Stationary Solution

For $\beta = 0$ and $I^{\text{ext}}(\mathbf{x}, t) = 0$, the non-zero fixed point solution to Eq. (7.4) exists when $k < k_c \equiv \rho J_0^2 / (32\pi a)$:

$$u(\mathbf{x}) = u_{00} \exp\left(-\frac{|\mathbf{x} - \mathbf{z}|^2}{4a^2}\right), \quad (7.6)$$

where $\rho J_0 u_{00} = 4(1 \pm \sqrt{1 - k/k_c})/(k/k_c)$ and \mathbf{z} is an arbitrary point over the field. It is obvious that the fixed point solution with larger amplitude is stable, while the other is unstable. The solutions of u_{00} as a function of k/k_c are shown in Figure 7.1.

For $\beta > 0$ and $I^{\text{ext}}(\mathbf{x}, t) = 0$, we approximate the attractor profiles of $u(\mathbf{x}, t)$ and $1 - p(\mathbf{x}, t)$ by non-moving Gaussian distributions

$$u(\mathbf{x}, t) = u_{00}(t) \exp\left(-\frac{|\mathbf{x}|^2}{4a^2}\right) \text{ and} \quad (7.7)$$

$$1 - p(\mathbf{x}, t) = p_{00}(t) \exp\left(-\frac{|\mathbf{x}|^2}{2a^2}\right). \quad (7.8)$$

They are not the exact solutions of Eqs. (7.11), (7.4) and (7.5). However, by projecting

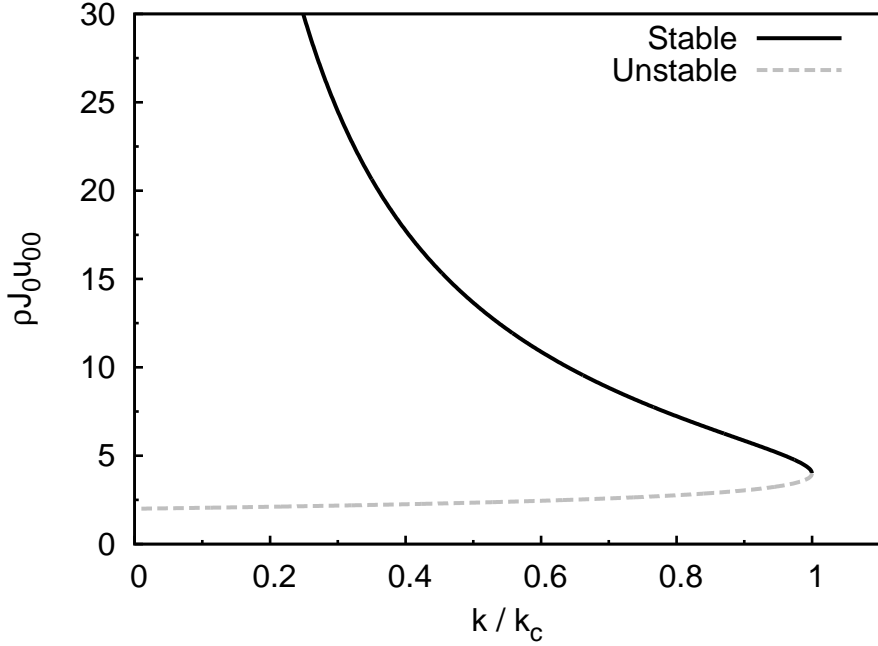


Figure 7.1: Solution of $\rho J_0 u_{00}$ as a function of k/k_c . For each k/k_c less than 1, the larger solution of $\rho J_0 u_{00}$ is stable, while the smaller solution is unstable.

Eqs. (7.4) and (7.5) onto $\exp[-|\mathbf{x}|^2/(4a^2)]$ and $\exp[-|\mathbf{x}|^2/(2a^2)]$, respectively, differential equations of $u_{00}(t)$ and $p_{00}(t)$ can be obtained. Similar to the study by Fung *et al.* [24], $u(\mathbf{x}, t)$ can be replaced by rescaled variables $\tilde{u}(\mathbf{x}, t)$, because $u_{00}(t)$ has a dimension $1/(\rho J_0)$. $\tilde{u}_{00}(t) \equiv \rho J_0 u_{00}(t)$. k and β can also be rescaled by $\tilde{k} \equiv k/k_c$ and $\tilde{\beta} \equiv \tau_d \beta / (\rho^2 J_0^2)$.

With these rescaled variables, the differential equations of $\tilde{u}_{00}(t)$, $p_{00}(t)$ and $B(t)$ are

$$\tau_s \frac{d\tilde{u}_{00}}{dt}(t) = -\tilde{u}_{00}(t) + \frac{1}{2} \frac{1}{B(t)} \tilde{u}_{00}(t)^2 \left[1 - \frac{4}{7} p_{00}(t) \right], \quad (7.9)$$

$$\tau_d \frac{dp_{00}}{dt}(t) = -p_{00}(t) + \frac{1}{B(t)} \tilde{\beta} \tilde{u}_{00}(t)^2 \left[1 - \frac{2}{3} p_{00}(t) \right] \text{ and} \quad (7.10)$$

$$\tau_B \frac{dB}{dt}(t) = -B(t) + 1 + \frac{1}{16} \tilde{k} \tilde{u}_{00}(t)^2. \quad (7.11)$$

Since we are interested in the steady state of the network. Let us consider the case with $d\tilde{u}_{00}/dt = 0$, $dp_{00}/dt = 0$ and $dB/dt = 0$. For the first two differential equations, we may let $\tilde{\beta}B$ as given. Then, we can numerically solve for \tilde{u}_{00}/B and p_{00} . For a given $\tilde{\beta}B$, \tilde{k}

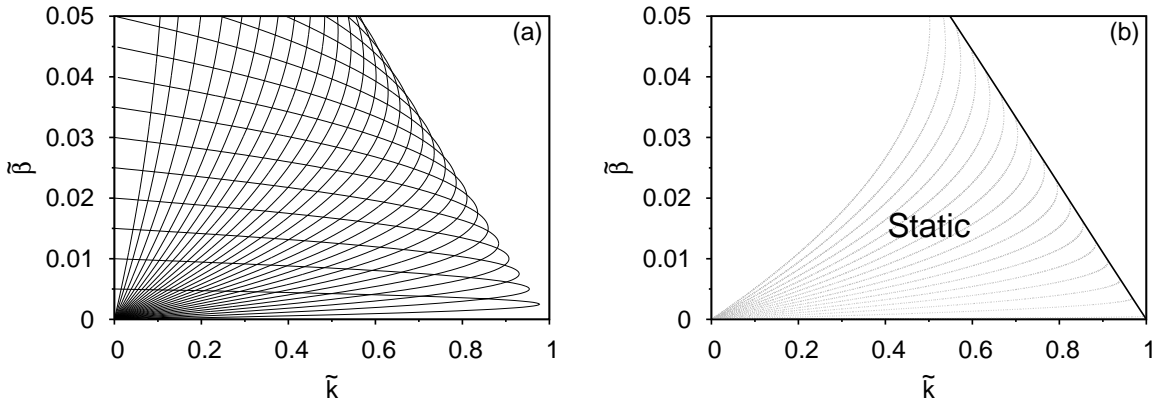


Figure 7.2: (a) Parabolas given by Eq. (7.12). (b) Grey curves are stable branches of parabolas in (a). Solid line is the phase boundary of static bumps.

and $\tilde{\beta}$ can be related by a parabola given by

$$\tilde{k} = \frac{16}{\left(\frac{\tilde{u}_{00}}{B}\right)^2} \left[-\frac{1}{\left(B\tilde{\beta}\right)^2} \tilde{\beta}^2 + \frac{1}{B\tilde{\beta}} \tilde{\beta} \right]. \quad (7.12)$$

Figure 7.2(a) shows parabolas in the parameter space spanned by \tilde{k} and $\tilde{\beta}$. The region spanned by the parabolas is the region of existence of fixed point solutions. By solving them, we see that the fixed point solution exists only when

$$\begin{cases} \tilde{\beta} \leq \frac{3}{16} \tilde{k} \frac{1-\sqrt{\tilde{k}}}{\sqrt{\tilde{k}-\frac{1}{7}}} & , \text{ if } \frac{9}{49} \leq \tilde{k} \leq 1 \\ \tilde{\beta} \leq \frac{9}{56} \left(\frac{3}{7} - \sqrt{\frac{9}{49} - \tilde{k}} \right) & , \text{ if } 0 \leq \tilde{k} \leq \frac{9}{49} \end{cases}. \quad (7.13)$$

It can be shown that, for a given set of \tilde{k} and $\tilde{\beta}$, if non-zero solutions exist, there is one solution such that its amplitude is stable, if $\tau_B < \tau_s$. In Figure 7.2(b), gray curves are stable branches of parabolas in Figure 7.2(a). The stability of a fixed point solution can be checked by studying Eqs. (7.9) - (7.11).

7.2.3 Translational Instability

We have simplified Eqs. (7.11), (7.4) and (7.5) by introducing the approximation given by Eqs. (7.7) and (7.8). However, this simplification is useful only to study the stability of the amplitude of the bump-shaped solution. For the translational stability, we need to consider the stability of the solution against asymmetric distortions of the waveform.

Considering the stability of the solution against asymmetric distortions is a reasonable test, as the dip of $p(\mathbf{x}, t)$ is generated by activities of neurons. If the solution is moving, the dip of $p(\mathbf{x}, t)$ is always lagging behind. As a result, the asymmetric components of $p(\mathbf{x}, t)$ with respect to the center of mass of $u(\mathbf{x}, t)$ becomes non-zero. We may drop the asymmetric component of $u(\mathbf{x}, t)$ if we choose a moving frame such that the major asymmetric mode is zero. Let us assume

$$u(\mathbf{x}, t) = u_{00}(t) \exp\left(-\frac{|\mathbf{x}|^2}{4a^2}\right) \text{ and} \quad (7.14)$$

$$p(\mathbf{x}, t) = p_{00}(t) \exp\left(-\frac{|\mathbf{x}|^2}{2a^2}\right) + p_{10}(t) \frac{x_0}{a} \exp\left(-\frac{|\mathbf{x}|^2}{2a^2}\right). \quad (7.15)$$

Here, due to the symmetry of the space of the preferred stimulus, we consider only the distortion along the x_1 -direction. By substituting these two assumptions in Eqs. (7.11), (7.4) and (7.5), we may study the stability of static solutions against asymmetric distortions.

With the assumptions Eqs. (7.14) and (7.15), we can derive the stability matrix by calculating Jacobian matrix around the fixed point solution. Then, we have

$$\begin{pmatrix} \mathcal{A} & 0 \\ 0 & M \end{pmatrix}, \quad (7.16)$$

where

$$\begin{aligned} \mathcal{A} \\ = & \begin{pmatrix} -1 + \frac{1}{B} \tilde{u}_{00} (1 - \frac{4}{7} \tilde{p}_{00}) & -\frac{2}{7} \frac{1}{B} \tilde{u}_{00}^2 & -\frac{1}{2} \frac{1}{B^2} \tilde{u}_{00}^2 (1 - \frac{4}{7} \tilde{p}_{00}) \\ \frac{2}{\tau_d} \frac{\tilde{\beta}}{B} \tilde{u}_{00} (1 - \frac{2}{3} \tilde{p}_{00}) & -\frac{1}{\tau_d} - \frac{2}{3} \frac{1}{\tau_d} \frac{\tilde{\beta}}{B} \tilde{u}_{00}^2 & -\frac{1}{\tau_d} \frac{\tilde{\beta}}{B^2} \tilde{u}_{00}^2 (1 - \frac{2}{3} \tilde{p}_{00}) \\ \frac{1}{8} \frac{1}{\tau_B} \tilde{k} \tilde{u}_{00} & 0 & -\frac{1}{\tau_B} \end{pmatrix}, \end{aligned} \quad (7.17)$$

$$\begin{aligned} M \\ = & \frac{1}{\tau_d} \left(-1 + \frac{\tilde{\beta}}{B} \frac{4}{9} \tilde{u}_{00}^2 + \frac{\tau_d}{\tau_s} \frac{1}{B} \frac{8}{49} \tilde{u}_{00} \tilde{p}_{00} \right). \end{aligned} \quad (7.18)$$

Here, obviously, if $M > 0$, the static solution of two-dimensional CANNs with short-term synaptic depression will be translationally unstable.

By studying the stability matrix, we found that the bump-shaped solution will be stable only if

$$\frac{4}{9} \left(\tilde{\beta} B \right) \left(\frac{\tilde{u}_{00}}{B} \right)^2 + \frac{\tau_d}{\tau_s} \frac{8}{49} \frac{\tilde{u}_{00}}{B} p_{00} < 1. \quad (7.19)$$

In this case, asymmetric distortions cannot initiate spontaneous motion. In the case that this inequality does not hold, there may be a moving solution such that the bump-shaped profile can move spontaneously with a speed dictated by \tilde{k} , $\tilde{\beta}$ and τ_d/τ_s .

7.2.4 Moving Solution

In the one-dimensional situation, when \tilde{k} is small and $\tilde{\beta}$ is relatively large, there may be spontaneous moving solutions (see Chapter 3). To analyze the moving solution, we need to consider higher order expansion of $u(\mathbf{x}, t)$ and $p(\mathbf{x}, t)$. In general, $u(\mathbf{x}, t)$ and $p(\mathbf{x}, t)$ can be expanded by any basis functions. Here, we have chosen eigenstates of quantum harmonic oscillator as basis functions.

$$u(\mathbf{x}, t) = \sum_{k_0, k_1} u_{k_0 k_1}(t) \psi_{k_0}(\xi_0) \psi_{k_1}(\xi_1), \text{ and} \quad (7.20)$$

$$1 - p(\mathbf{x}, t) = \sum_{k_0, k_1} p_{k_0 k_1}(t) \varphi_{k_0}(\xi_0) \varphi_{k_1}(\xi_1), \quad (7.21)$$

where

$$\psi_k(\xi_i) = \frac{1}{\sqrt{\sqrt{2\pi}a2^k k!}} H_n\left(\frac{\xi_i}{\sqrt{2a}}\right) \exp\left(-\frac{\xi_i^2}{4a^2}\right), \text{ and} \quad (7.22)$$

$$\varphi_k(\xi_i) = \frac{1}{\sqrt{\sqrt{\pi}a2^k k!}} H_n\left(\frac{\xi_i}{a}\right) \exp\left(-\frac{\xi_i^2}{2a^2}\right). \quad (7.23)$$

Here $\xi_i \equiv x_i - c_i t$. c_i is the velocity of the moving frame on the x_i -direction. H_n is the n^{th} order physicists' Hermite polynomial. After substituting Eqs. (7.20) and (7.21) into Eqs. (7.11), (7.4) and (7.5), we should obtain

$$\begin{aligned} & \tau_s \frac{d\tilde{u}_{k_0 k_1}}{dt}(t) \\ &= -\tilde{u}_{k_0 k_1}(t) + \frac{\tau_s c_0}{2a} \left[\sqrt{k_0 + 1} \tilde{u}_{k_0+1, k_1}(t) - \sqrt{k_0} \tilde{u}_{k_0-1, k_1}(t) \right] \\ & \quad + \frac{\tau_s c_1}{2a} \left[\sqrt{k_1 + 1} \tilde{u}_{k_0, k_1+1}(t) - \sqrt{k_1} \tilde{u}_{k_0, k_1-1}(t) \right] \\ & \quad + \frac{1}{B(t)} \sum_{n_0 n_1 m_0 m_1} C_{n_0 m_0}^{k_0} C_{n_1 m_1}^{k_1} \tilde{u}_{n_0 n_1}(t) \tilde{u}_{m_0 m_1}(t) \\ & \quad - \frac{1}{B(t)} \sum_{n_0 n_1 m_0 m_1 l_0 l_1} D_{n_0 m_0 l_0}^{k_0} D_{n_1 m_1 l_1}^{k_1} \tilde{u}_{n_0 n_1}(t) \tilde{u}_{m_0 m_1}(t) p_{l_0 l_1}(t) \end{aligned} \quad (7.24)$$

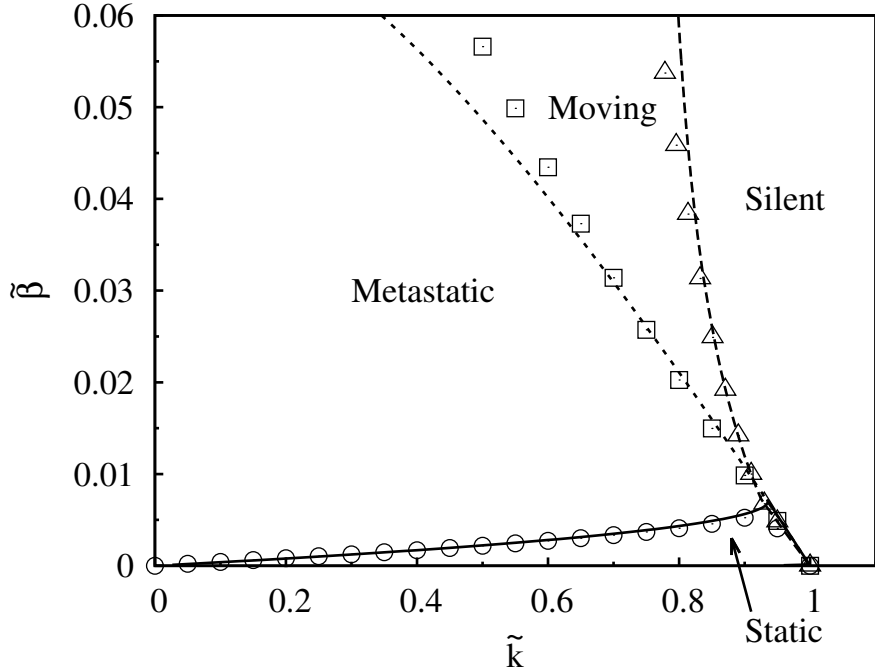


Figure 7.3: Phase diagram of different phases under this theoretical framework. Circles: boundary of the translational stability through simulations. Squares: boundary of the amplitude stability through simulations. Triangles: boundary of the stability of moving bumps through simulations. Curves: corresponding theoretical predictions. Parameter: $\tau_d/\tau_s = 50$.

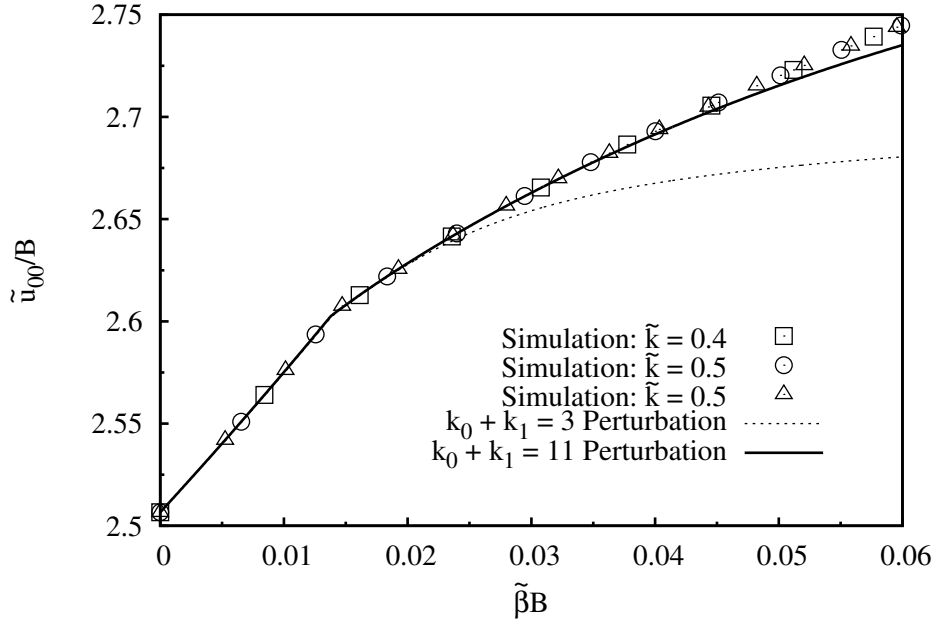


Figure 7.4: Measurements and predictions of \tilde{u}_{00}/B . Symbols: measurements from various \tilde{k} . Curves: Different levels of predictions of $0 \leq \tilde{k} \leq 1$. Parameter: $\tau_d/\tau_s = 50$.

$$\begin{aligned}
& \tau_d \frac{dp_{k_0 k_1}}{dt} (t) \\
= & -p_{k_0 k_1} (t) + \frac{\tau_d c_0}{\sqrt{2}a} \left[\sqrt{k_0 + 1} p_{k_0 + 1, k_1} (t) - \sqrt{k_0} p_{k_0 - 1, k_1} (t) \right] \\
& + \frac{\tau_d c_1}{\sqrt{2}a} \left[\sqrt{k_1 + 1} p_{k_0, k_1 + 1} (t) - \sqrt{k_1} p_{k_0, k_1 - 1} (t) \right] \\
& + \frac{\tilde{\beta}}{B(t)} \sum_{n_0 n_1 m_0 m_1} E_{n_0 m_0}^{k_0} E_{n_1 m_1}^{k_1} \tilde{u}_{n_0 n_1} (t) \tilde{u}_{m_0 m_1} (t) \\
& - \frac{\tilde{\beta}}{B(t)} \sum_{n_0 n_1 m_0 m_1} F_{n_0 m_0 l_0}^{k_0} F_{n_1 m_1 l_1}^{k_1} \tilde{u}_{n_0 n_1} (t) \tilde{u}_{m_0 m_1} (t) p_{l_0 l_1} (t) \quad (7.25)
\end{aligned}$$

$$\begin{aligned}
& \tau_B \frac{dB}{dt} (t) \\
= & -B(t) + 1 + k\rho \sum_{k_0 k_1} \tilde{u}_{k_0 k_1} (t)^2. \quad (7.26)
\end{aligned}$$

$\tilde{u}_{k_0 k_1}$'s are rescaled dynamical variables. $\tilde{u}_{k_0 k_1} (t) \equiv \rho J_0 u_{k_0 k_1} (t)$. C_{nm}^k , D_{nml}^k , E_{nm}^k and F_{nml}^k are defined in the same way as in Appendix B in [24]. However, the above equations cannot form a complete set of equations sufficient to solve the fixed point solution. We also need to consider the self-consistent condition:

$$\frac{\int d\xi \tilde{u}(\xi, t) \xi_i}{\int d\xi \tilde{u}(\xi, t)} = 0. \quad (7.27)$$

With this condition, the fixed point solution of these differential equations is also determined by $\tilde{\beta}B$. By comparing with the simulation results, we found that not only solutions to these fixed point equations, but also various measurements of the network state are determined by $\tilde{\beta}B$, as shown in Figures 7.4 - 7.7. In Figures 7.5 and 7.6, I compare second order variables between simulations and predictions by transforming to polar coordinates via $\xi_0 = r \cos \theta$ and $\xi_1 = r \sin \theta$,

$$\begin{aligned}
\psi_2(\xi_0) \psi_0(\xi_1) &= \frac{1}{4a\sqrt{\pi}} H_2 \left(\frac{\xi_0}{\sqrt{2}a} \right) H_0 \left(\frac{\xi_1}{\sqrt{2}a} \right) \exp \left(-\frac{\xi_0^2 + \xi_1^2}{4a^2} \right) \\
&= \frac{1}{2a\sqrt{\pi}} \left(\frac{1}{4} \frac{r^2}{a^2} - 1 \right) e^{-\frac{r^2}{4a^2}} + \frac{1}{8a\sqrt{\pi}} \frac{r^2}{a^2} (e^{i2\theta} + e^{-i2\theta}) e^{-\frac{r^2}{4a^2}}, \quad (7.28)
\end{aligned}$$

$$\psi_0(\xi_0) \psi_2(\xi_1) = \frac{1}{2a\sqrt{\pi}} \left(\frac{1}{4} \frac{r^2}{a^2} - 1 \right) e^{-\frac{r^2}{4a^2}} - \frac{1}{8a\sqrt{\pi}} \frac{r^2}{a^2} (e^{i2\theta} + e^{-i2\theta}) e^{-\frac{r^2}{4a^2}}, \quad (7.29)$$

$$\psi_1(\xi_0) \psi_1(\xi_1) = -\sqrt{2}i \frac{1}{8\sqrt{\pi}a} \frac{r^2}{a^2} (e^{i2\theta} - e^{-i2\theta}) e^{-\frac{r^2}{4a^2}}. \quad (7.30)$$

Therefore,

$$\begin{aligned}
& \tilde{u}_{20}\psi_2(\xi_0)\psi_0(\xi_1) + \tilde{u}_{02}\psi_0(\xi_0)\psi_2(\xi_1) + \tilde{u}_{11}\psi_1(\xi_0)\psi_1(\xi_1) \\
= & (\tilde{u}_{20} + \tilde{u}_{02}) \frac{1}{2a\sqrt{\pi}} \left(\frac{1}{4} \frac{r^2}{a^2} - 1 \right) e^{-\frac{r^2}{4a^2}} \\
& + \left(\tilde{u}_{20} - \tilde{u}_{02} - \sqrt{2}i\tilde{u}_{11} \right) \frac{1}{8a\sqrt{\pi}} \frac{r^2}{a^2} e^{-\frac{r^2}{4a^2}} e^{i2\theta} \\
& + \left(\tilde{u}_{20} - \tilde{u}_{02} + \sqrt{2}i\tilde{u}_{11} \right) \frac{1}{8a\sqrt{\pi}} \frac{r^2}{a^2} e^{-\frac{r^2}{4a^2}} e^{-i2\theta}
\end{aligned} \tag{7.31}$$

In order to compare predictions to simulation results without considering the moving direction along the space, I use $(\tilde{u}_{20} + \tilde{u}_{02})/B$ (in Figure 7.5) and $|\tilde{u}_{20} - \tilde{u}_{02} - \sqrt{2}i\tilde{u}_{11}|/B$ (in Figure 7.6) for the case of $k_0+k_1=2$ to achieve the purpose. $(\tilde{u}_{20} + \tilde{u}_{02})$ is the average change in width of the bump-shaped profile, while $|\tilde{u}_{20} - \tilde{u}_{02} - \sqrt{2}i\tilde{u}_{11}|$ is the magnitude of the anisotropic mode.

Since B is proportional to \tilde{u}_{00}^2 , an increase of \tilde{u}_{00}/B implies a decrease in \tilde{u}_{00} . In Figure 7.4, the slope of \tilde{u}_{00}/B is discontinuous at about $\tilde{\beta}B \approx 0.0137$. For $\tilde{\beta}B \lesssim 0.0137$, the slope is significantly larger than that in the region of $\tilde{\beta}B \gtrsim 0.0137$. It implies that the motion of the bump helps the bump to maintain its magnitude. Figure 7.6 suggests that anisotropic mode happens only when the bump is not static.

7.3 Two-dimensional Continuous Attractor Neural Network with Local Subtractive Inhibition

7.3.1 The Model

In the case of local subtractive inhibition, we consider a field of inhibitory neurons of which activities are denoted by $v(\mathbf{x}, t)$. The dynamics of the neuronal current is similar to Eq. (7.4).

$$\tau_s \frac{du(\mathbf{x}, t)}{dt} = -u(\mathbf{x}, t) + \rho \int d\mathbf{x}' J(\mathbf{x}, \mathbf{x}') r(\mathbf{x}', t) - v(\mathbf{x}, t) + I^{\text{ext}}(\mathbf{x}, t). \tag{7.32}$$

This differential equation is similar to Eq. (7.4). The second last term in this equation models the local subtractive inhibition. The dynamics of the local subtractive inhibition is governed by

$$\tau_i \frac{dv}{dt}(\mathbf{x}, t) = -v(\mathbf{x}, t) + \gamma f[u(\mathbf{x}, t)]. \tag{7.33}$$

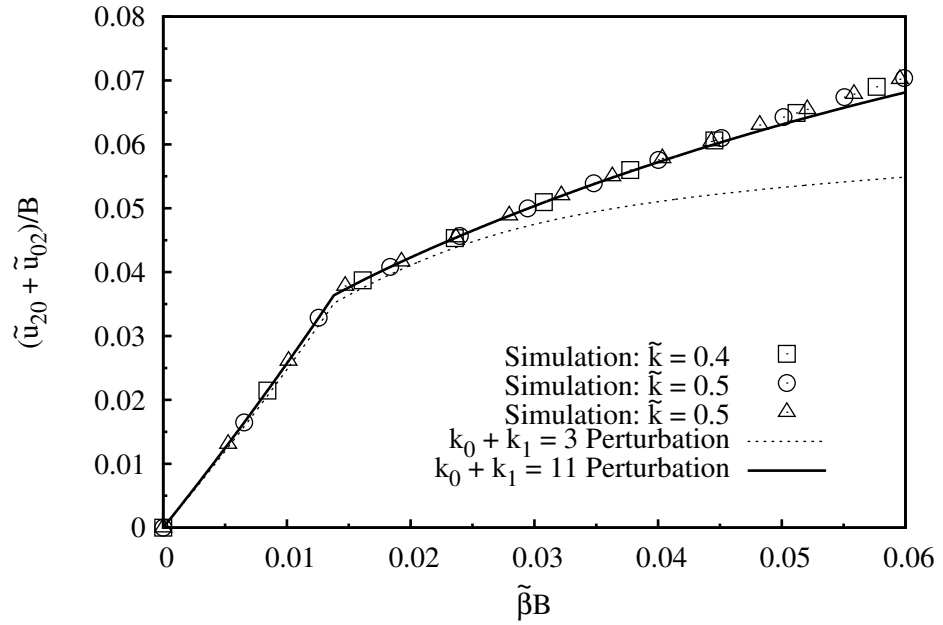


Figure 7.5: Measurements and predictions of $(\tilde{u}_{20} + \tilde{u}_{02})/B$. Symbols: measurements from various \tilde{k} . Curves: Different levels of predictions for $0 \leq \tilde{k} \leq 1$. Parameter: $\tau_d/\tau_s = 50$.

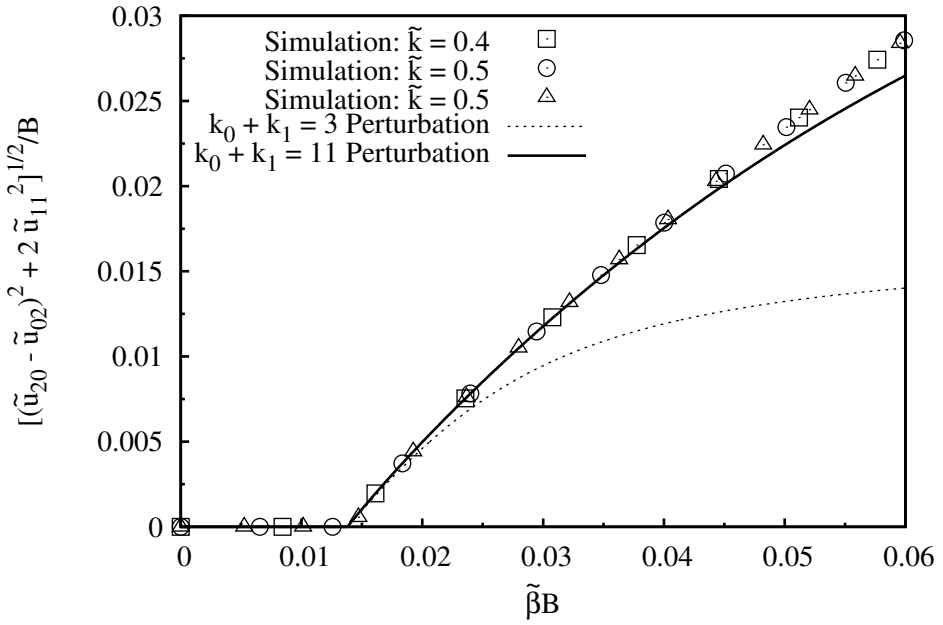


Figure 7.6: Measurements and predictions of $\sqrt{(\tilde{u}_{20} - \tilde{u}_{02})^2 + \tilde{u}_{11}^2}/B$. Symbols: measurements from various \tilde{k} . Curves: Different levels of predictions for $0 \leq \tilde{k} \leq 1$. Parameter: $\tau_d/\tau_s = 50$.

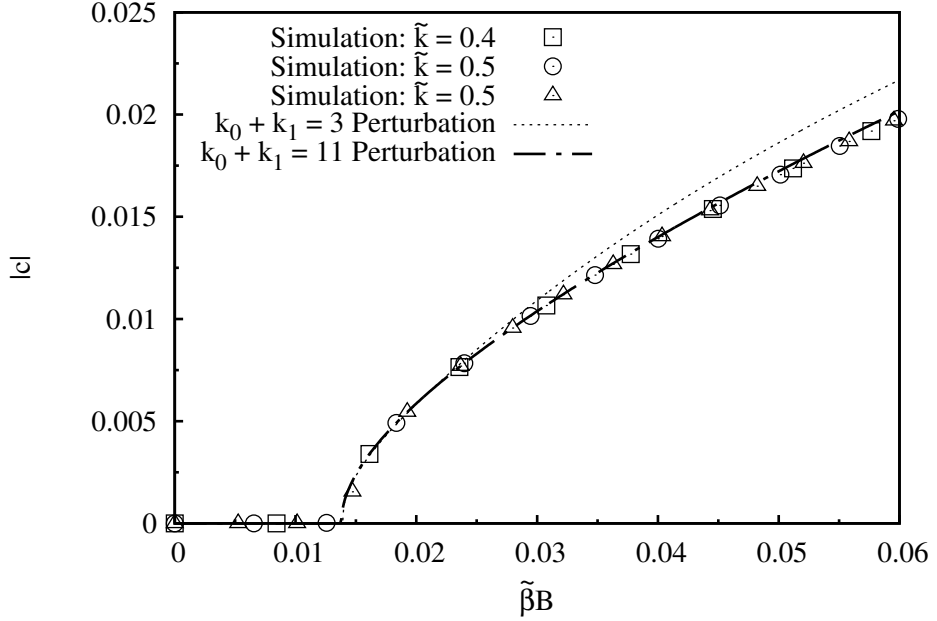


Figure 7.7: Measurements and predictions of the intrinsic moving speed. Symbols: measurements from various \tilde{k} . Curves: Different levels of predictions for $0 \leq \tilde{k} \leq 1$. Parameter: $\tau_d/\tau_s = 50$.

τ_i is the timescale of the local subtractive inhibition. γ is the degree of the local subtractive inhibition. f is the coupling from excitatory neurons to inhibitory neurons. This local subtractive inhibition is equivalent to spike frequency adaptation. Because the dynamical variable $v(x, t)$ increases in response to increase of $u(x, t)$, which can in turn suppress the growth of $u(x, t)$. The second last term in Eq. (7.32) is subtractive, because action potentials can turn on potassium currents to suppress future neuronal activities [52]. For simplicity, we have chosen

$$f(u) = u\Theta(u). \quad (7.34)$$

This choice is convenient for our analytic purpose. However, this choice should not affect the main conclusion qualitatively, so far as the firing rates of locally inhibitory neurons increase with $u(\mathbf{x}, t)$.

Like Eqs. (7.1) and (7.2), the neuronal activity of neurons at \mathbf{x} is given by a nonlinear function of $u(\mathbf{x}, t)$,

$$r(\mathbf{x}, t) = \frac{u(\mathbf{x}, t)^2}{B(t)}\Theta[u(\mathbf{x}, t)], \quad (7.35)$$

where Θ is the step function and $B(t)$ is the total activity of the field which gives the

divisive global inhibition. The neuronal activity is related to the average firing rate of the neuron. The evolution of the global inhibition is given by

$$\tau_B \frac{dB(t)}{dt} = -B(t) + 1 + \rho k \int d\mathbf{x}' u(\mathbf{x}', t)^2. \quad (7.36)$$

k is the parameter controlling the strength of the divisive global inhibition.

7.3.2 Stationary Solution

To study the stationary solution, we assume

$$u(\mathbf{x}) = u_{00} \exp\left(-\frac{\mathbf{x}^2}{4a^2}\right) \quad (7.37)$$

$$v(\mathbf{x}) = v_{00} \exp\left(-\frac{\mathbf{x}^2}{4a^2}\right). \quad (7.38)$$

The fixed point solution is given by

$$\tilde{u}_{00} = 4 \frac{1 + \sqrt{1 - (1 + \gamma)^2 \tilde{k}}}{(1 + \gamma) \tilde{k}} \quad (7.39)$$

$$\tilde{v}_{00} = 4\gamma \frac{1 + \sqrt{1 - (1 + \gamma)^2 \tilde{k}}}{(1 + \gamma) \tilde{k}} \quad (7.40)$$

$$B = 2 \frac{1 + \sqrt{1 - (1 + \gamma)^2 \tilde{k}}}{(1 + \gamma)^2 \tilde{k}} \quad (7.41)$$

\tilde{u}_{00} is a rescaled variable defined by $\tilde{u}_{00} \equiv \rho J_0 u_{00}$. Similarly, $\tilde{v}_{00} \equiv \rho J_0 v_{00}$. For $\tau_B = 0$, the fixed point solution with larger \tilde{u}_{00} and \tilde{v}_{00} is stable whenever the solution exists, i.e.

$$0 < \tilde{k} < \frac{1}{(1 + \gamma)^2}, \quad (7.42)$$

labeled by L_1 in Figure 7.8 with $\tilde{k} = 0.3$. The stability issue can be studied by considering the dynamics of distortions of variables:

$$\tau_s \frac{d}{dt} \begin{pmatrix} \delta \tilde{u}_{00}(t) \\ \delta \tilde{v}_{00}(t) \\ \delta B(t) \end{pmatrix} = \begin{pmatrix} -1 + 2(1 + \gamma) & -1 & -2(1 + \gamma)^2 \\ \gamma \frac{\tau_s}{\tau_i} & -\frac{\tau_s}{\tau_i} & 0 \\ \frac{\tau_s}{\tau_B} \frac{1 \pm \sqrt{1 - (1 + \gamma)^2 \tilde{k}}}{2(1 + \gamma)} & 0 & -\frac{\tau_s}{\tau_B} \end{pmatrix} \begin{pmatrix} \delta \tilde{u}_{00}(t) \\ \delta \tilde{v}_{00}(t) \\ \delta B(t) \end{pmatrix} \quad (7.43)$$

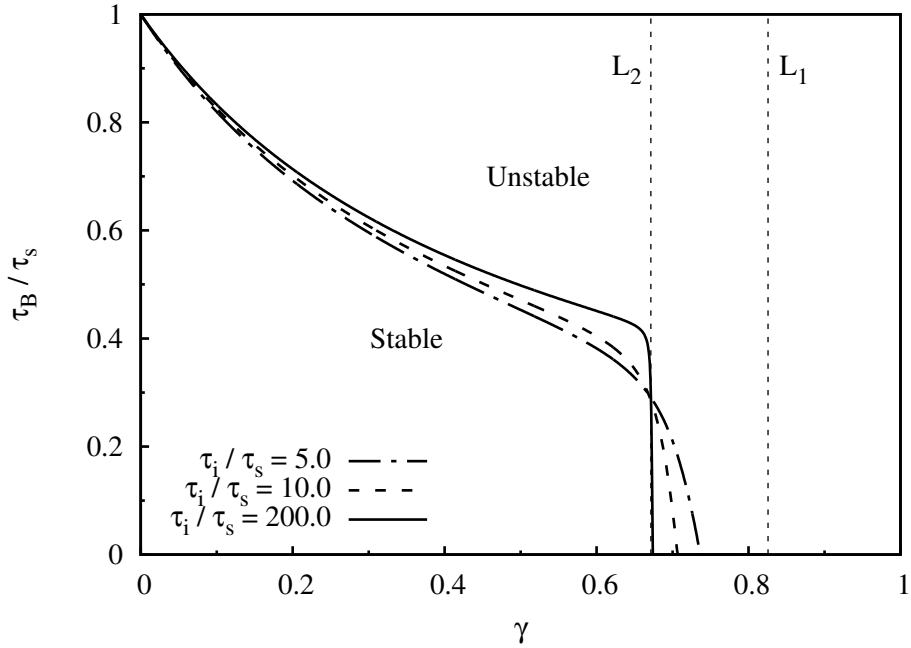


Figure 7.8: Maximum τ_B/τ_s able to stabilize the amplitude of stationary solutions as a function of γ , given that $\tilde{k} = 0.3$. L_1 : maximum γ of the existence of stationary solutions. L_2 : maximum γ of the existence of stationary solution with stable amplitude at the limit $\tau_i/\tau_s \rightarrow +\infty$.

For $\tau_B > 0$, the stable parameter region over the (\tilde{k}, γ) space becomes smaller as τ_B increases. For $\tau_i \gg \tau_s$, the range of \tilde{k} to stabilize the stationary solution is given by

$$0 < \tilde{k} < \frac{2\gamma + 1}{(1 + \gamma)^4}, \quad (7.44)$$

labeled by L_2 in Figure 7.8 with $\tilde{k} = 0.3$. On the other hand, if $\tau_B/\tau_s \geq 1$, there will be no stable stationary solution. In Figure 7.8, we have shown that if γ becomes larger, the maximum value of τ_B/τ_s to stabilize the stationary solution will be smaller.

7.3.3 Translational Stability

To study the translational stability, we consider lower order asymmetric distortions added to the stationary solution. The major concern here is the step function appearing in Eq. (7.34). But the step function does not have a first order effect on translational distortions.

We let

$$u(\mathbf{x}, t) = u_{00}(t) \exp\left(-\frac{|\mathbf{x}|^2}{4a^2}\right) \text{ and} \quad (7.45)$$

$$v(\mathbf{x}, t) = v_{00}(t) \exp\left(-\frac{|\mathbf{x}|^2}{4a^2}\right) + v_{10}(t) \frac{x_0}{a} \exp\left(-\frac{|\mathbf{x}|^2}{4a^2}\right). \quad (7.46)$$

As we are studying the stability issue of the stationary solution, let us adopt the solution in Eqs. (7.39) - (7.41) and put $v_{10} = 0$. Then, the dynamics of distortions of variables become

$$\begin{aligned} & \tau_s \frac{d}{dt} \begin{pmatrix} \delta \tilde{u}_{00}(t) \\ \delta \tilde{v}_{00}(t) \\ \delta B(t) \\ \delta \tilde{v}_{10} \end{pmatrix} \\ &= \begin{pmatrix} -1 + 2(1 + \gamma) & -1 & -2(1 + \gamma)^2 & 0 \\ \gamma \frac{\tau_s}{\tau_i} & -\frac{\tau_s}{\tau_i} & 0 & 0 \\ \frac{1}{2} \frac{\tau_s}{\tau_B} \frac{1 \pm \sqrt{1-(1+\gamma)^2 \bar{k}}}{(1+\gamma)} & 0 & -\frac{\tau_s}{\tau_B} & 0 \\ 0 & 0 & 0 & -\frac{\tau_s}{\tau_i} + \gamma \end{pmatrix} \begin{pmatrix} \delta \tilde{u}_{00}(t) \\ \delta \tilde{v}_{00}(t) \\ \delta B(t) \\ \delta \tilde{v}_{10} \end{pmatrix} \end{aligned} \quad (7.47)$$

Clearly, the variable v_{10} becomes unstable if $\gamma > \tau_s/\tau_i$. It implies that if the dynamics of local subtractive inhibition is slower, the stationary solution will be easier to become translationally unstable.

7.3.4 Moving Solution

Once $\gamma > \tau_s/\tau_i$ is satisfied, the spontaneous motion of a bump-shaped solution becomes possible. However, as mentioned in the case with STD, low order expansion of $u(\mathbf{x}, t)$ and $p(\mathbf{x}, t)$ is not sufficient to describe moving solutions. In this case, we have to consider higher order expansion to obtain good predictions on the behaviors of moving solutions. Surprisingly, we found that a limited order of expansion of $u(\mathbf{x}, t)$ and $v(\mathbf{x}, t)$ can give a fairly good predictions on moving solutions.

In general, we consider

$$u(\mathbf{x}, t) = \sum_{k_0 k_1} u_{k_0 k_1}(t) \phi_{k_0}(\xi_0) \phi_{k_1}(\xi_1), \text{ and} \quad (7.48)$$

$$v(\mathbf{x}, t) = \sum_{k_0 k_1} v_{k_0 k_1}(t) \phi_{k_0}(\xi_0) \phi_{k_1}(\xi_1). \quad (7.49)$$

Here,

$$\phi_{k_i}(\xi_i) = \frac{1}{\sqrt{\sqrt{2\pi}ak_i!}} H_{k_i}\left(\frac{\xi_i}{a}\right) \exp\left(-\frac{\xi_i^2}{4a^2}\right) \quad (7.50)$$

and H_{k_i} is the k_i^{th} order probabilist's Hermite polynomial. Eqs. (7.39) and (7.40) become

$$\begin{aligned} & \tau_s \frac{d\tilde{u}_{k_0 k_1}}{dt}(t) + \frac{\tau_s c_0}{2a} \left[\sqrt{k_0} \tilde{u}_{k_0-1, k_1}(t) - \sqrt{k_0+1} \tilde{u}_{k_0+1, k_1}(t) \right] \\ & \quad + \frac{\tau_s c_1}{2a} \left[\sqrt{k_1} \tilde{u}_{k_0, k_1-1}(t) - \sqrt{k_1+1} \tilde{u}_{k_0, k_1+1}(t) \right] \quad (7.51) \\ &= -\tilde{u}_{k_0 k_1}(t) - \tilde{v}_{k_0 k_1}(t) + \frac{1}{B(t)} \sum_{n_0 n_1 m_0 m_1} C_{n_0 m_0}^{k_0} C_{n_1 m_1}^{k_1} \tilde{u}_{n_0 n_1}(t) \tilde{u}_{m_0 m_1}(t) \end{aligned} \quad (7.52)$$

$$\begin{aligned} & \tau_i \frac{d\tilde{v}_{k_0 k_1}}{dt}(t) + \frac{\tau_i c}{2a} \left[\sqrt{k_0} \tilde{v}_{k_0-1, k_1}(t) - \sqrt{k_0+1} \tilde{v}_{k_0+1, k_1}(t) \right] \\ & \quad + \frac{\tau_i c_1}{2a} \left[\sqrt{k_1} \tilde{v}_{k_0, k_1-1}(t) - \sqrt{k_1+1} \tilde{v}_{k_0, k_1+1}(t) \right] \\ &= -\tilde{v}_{k_0 k_1}(t) + \gamma \tilde{u}_{k_0 k_1}(t) \quad (7.53) \end{aligned}$$

Together with the self-consistent condition, Eq. (7.27), the fixed point solution is solvable. If we consider only terms up to $k_0 + k_1 = 2$ and motion along x_1 -direction, we can obtain the intrinsic speed of the moving solution,

$$\frac{\tau_s |c_0|}{2a} = \frac{\tau_s}{\tau_i} \sqrt{\frac{1}{3} \left(\frac{\tau_i}{\tau_s} \gamma - 1 \right)}. \quad (7.54)$$

As the space of the preferred stimulus is rotationally symmetric, this speed is applicable to motion in any direction. Even though this is an approximated solution with relatively few terms, the prediction on the intrinsic speed is fairly good, as shown in Figure 7.9.

Expansion up to $k_0 + k_1 = 2$ can also predict the phase diagram well. Although the intrinsic speed can be solved explicitly, other variables can only be solved numerically. By solving the moving solution numerically and testing their stability, we found that the predicted phase diagram matches the phase diagram obtained by computer simulations, as shown in Figure 7.10.

These two results suggest that, in this case, terms with $k_0 + k_1 \leq 2$ are sufficient to give good predictions on the behavior of bump-shaped solutions. However, for predictions on measurements of different components of the moving bump, we need to use higher order perturbation. In Figures 7.11 - 7.13, we have shown that higher order perturbation is needed to predict $\tilde{u}_{k_0 k_1}/B$, if the bump is moving. In Figures 7.12 and 7.13, like Figures 7.5 and 7.6, comparisons are not direct for \tilde{u}_{20} , \tilde{u}_{02} and \tilde{u}_{11} . Let us consider $\xi_0 = r \cos \theta$

and $\xi_1 = r \sin \theta$,

$$\phi_2(\xi_0)\phi_0(\xi_1) = \frac{1}{2a\sqrt{\pi}} \left(\frac{1}{2} \frac{r^2}{a^2} - 1 \right) e^{-\frac{r^2}{4a^2}} + \frac{1}{8a\sqrt{\pi}} \frac{r^2}{a^2} (e^{i2\theta} + e^{-i2\theta}) e^{-\frac{r^2}{4a^2}}, \quad (7.55)$$

$$\phi_0(\xi_0)\phi_2(\xi_1) = \frac{1}{2a\sqrt{\pi}} \left(\frac{1}{2} \frac{r^2}{a^2} - 1 \right) e^{-\frac{r^2}{4a^2}} - \frac{1}{8a\sqrt{\pi}} \frac{r^2}{a^2} (e^{i2\theta} + e^{-i2\theta}) e^{-\frac{r^2}{4a^2}}, \quad (7.56)$$

$$\phi_1(\xi_0)\phi_1(\xi_1) = -\sqrt{2}i \frac{1}{8\sqrt{\pi}a} \frac{r^2}{a^2} (e^{i2\theta} - e^{-i2\theta}) e^{-\frac{r^2}{4a^2}}. \quad (7.57)$$

So,

$$\begin{aligned} & \tilde{u}_{20}\phi_2(\xi_0)\phi_0(\xi_1) + \tilde{u}_{02}\phi_0(\xi_0)\phi_2(\xi_1) + \tilde{u}_{11}\phi_1(\xi_0)\phi_1(\xi_1) \\ = & (\tilde{u}_{20} + \tilde{u}_{02}) \frac{1}{2a\sqrt{\pi}} \left(\frac{1}{2} \frac{r^2}{a^2} - 1 \right) e^{-\frac{r^2}{4a^2}} \\ & + (\tilde{u}_{20} - \tilde{u}_{02} - \sqrt{2}i\tilde{u}_{11}) \frac{1}{8a\sqrt{\pi}} \frac{r^2}{a^2} e^{-\frac{r^2}{4a^2}} e^{i2\theta} \\ & + (\tilde{u}_{20} - \tilde{u}_{02} + \sqrt{2}i\tilde{u}_{11}) \frac{1}{8a\sqrt{\pi}} \frac{r^2}{a^2} e^{-\frac{r^2}{4a^2}} e^{-i2\theta}. \end{aligned}$$

In Figures 7.12 and 7.13, I compare predictions and simulation results of $(\tilde{u}_{20} + \tilde{u}_{02})$ and $|\tilde{u}_{20} - \tilde{u}_{02} - \sqrt{2}i\tilde{u}_{11}|$ for $k_0 + k_1 = 2$. $(\tilde{u}_{20} + \tilde{u}_{02})$ is the average change in width of the bump-shaped profile, while $|\tilde{u}_{20} - \tilde{u}_{02} - \sqrt{2}i\tilde{u}_{11}|$ is the magnitude of the anisotropic mode.

The behavior of moving solutions of CANNs with local subtractive inhibition is similar to that of CANNs with STD and global subtractive inhibition. For \tilde{u}_{00}/B , its trend is basically the same as \tilde{u}_{00}/B in the case with STD, shown in Figure 7.4. This transition happens whenever $\gamma = \tau_s/\tau_i$. Also, anisotropic modes will only appear when the bump is moving.

7.4 Discussion

In this chapter, I have presented the work on two-dimensional CANNs with STD and global divisive inhibition only, and two-dimensional CANNs with local subtractive inhibition. I found that their general behaviors of these two systems are very similar. Their phase diagrams are similar. In Figures 7.3 and 7.10, there are phase diagrams corresponding to these two models. In each of them, there is a region named static phase. Within the static phase, only static solutions are fixed point solution of the system.

If we increase the degree of STD or local subtractive inhibition further, the static

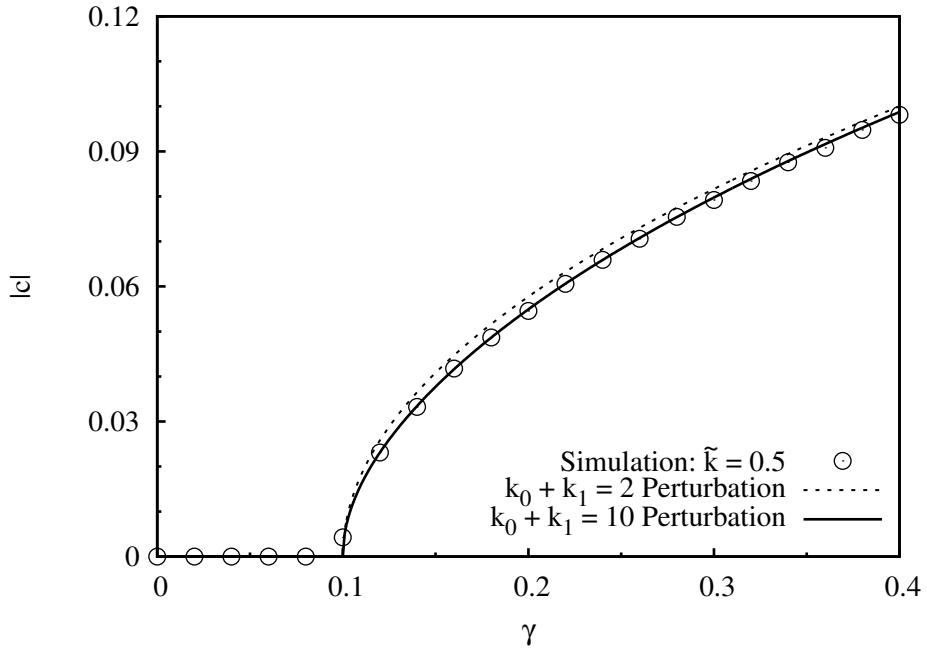


Figure 7.9: Speed of spontaneous motions as a function of γ .

state starts to become unstable translationally. There is a parameter region called the metastatic phase. In the metastatic region, either STD or local subtractive inhibition makes the bump-shaped network state favor their nearby regions rather than the location they are currently at. However, since the magnitude of STD or local subtractive inhibition are not too strong in this region, static bumps may also exist. For even larger degrees of STD or local subtractive inhibition, static bumps can no longer be stable in amplitude. So, we name this parameter region the moving phase, because only spontaneously moving solutions exist.

In the literature, there are richer phenomena reported in neural networks other than spontaneous motions of local neural activity. For example, breathing wavefronts on neural networks were found in theoretical analyses [50]. However, the perturbative formalism is not applicable in this case, because the basis function we used here are local, while the traveling wavefronts are globally spreading. Not only for breathing wavefront, but also spiral waves in the neural field cannot be analyzed using this method, due to the same reason.

In the case of collisions of two moving bump-shaped profiles of neuronal activity, one may find the perturbative method difficult when analyzing the dynamics. This is because there are two centers of mass of individual bumps. It makes the definition of the origin of the basis functions confusing. For example, if one chooses one of the centers of mass to be the origin of the basis functions, this family of basis functions will not be

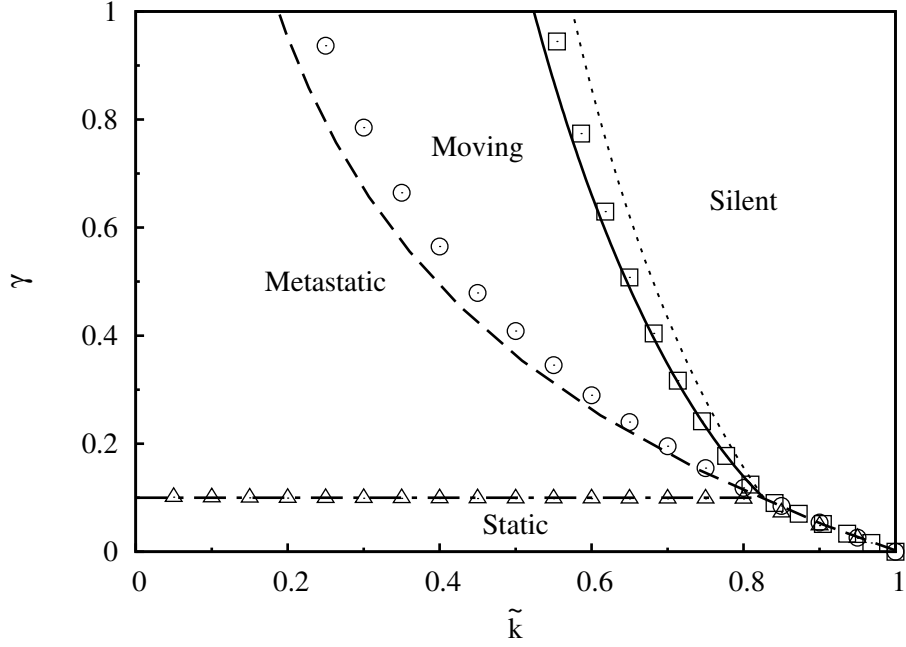


Figure 7.10: Phase diagram over the parameter space spanned by (\tilde{k}, γ) . Dotted line: predicted boundary for moving solutions by $k_0 + k_1 = 2$ perturbation. Solid line: predicted boundary for moving solutions by $k_0 + k_1 = 10$ perturbation. Dotted line: predicted boundary for static solutions with stable amplitudes by $k_0 + k_1 = 0$ perturbation. Dot-dashed line: predicted boundary for static solutions with stable amplitudes and translational stability by $k_0 + k_1 = 0$ perturbation. Parameters: $a = 0.5$, $\tau_i/\tau_s = 10$ and $\tau_B/\tau_s = 0.1$. Symbols: corresponding simulations.

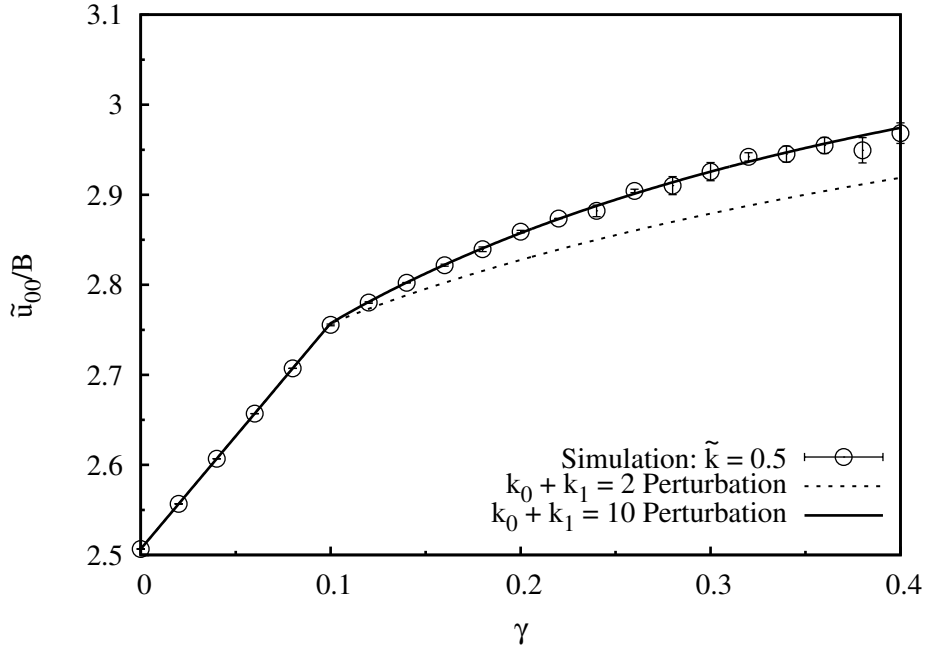


Figure 7.11: Projection of $\tilde{u}(x, t)$ on $\phi_0(\xi_0)\phi_0(\xi_1)$ at $\tilde{k} = 0.5$. Other parameters: same as Figure 7.10.

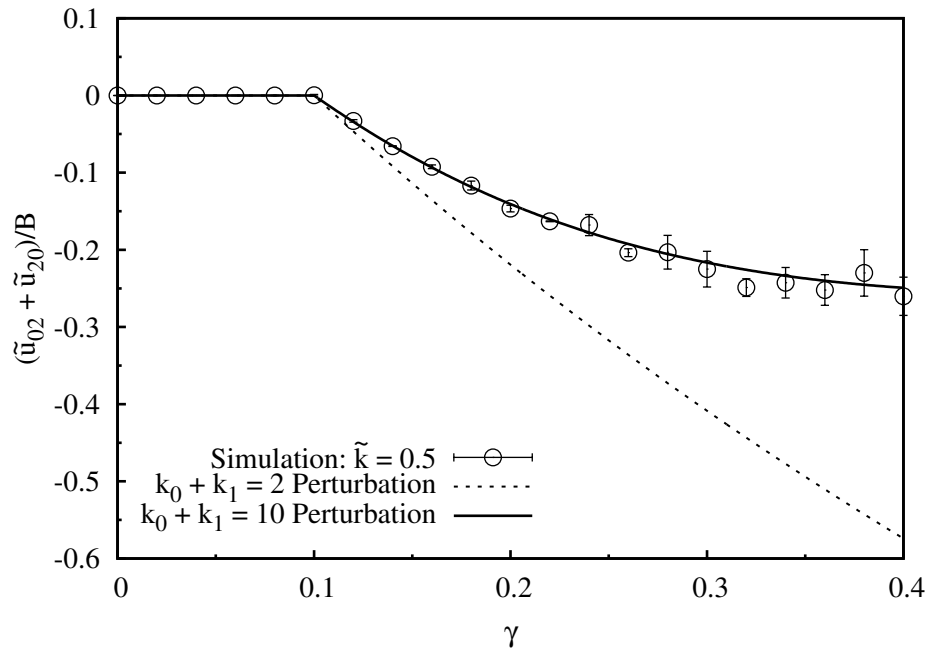


Figure 7.12: Projection of $\tilde{u}(x, t)$ on rotational symmetric basis function with $k_0+k_1=2$. Parameters: same as Figure 7.10.

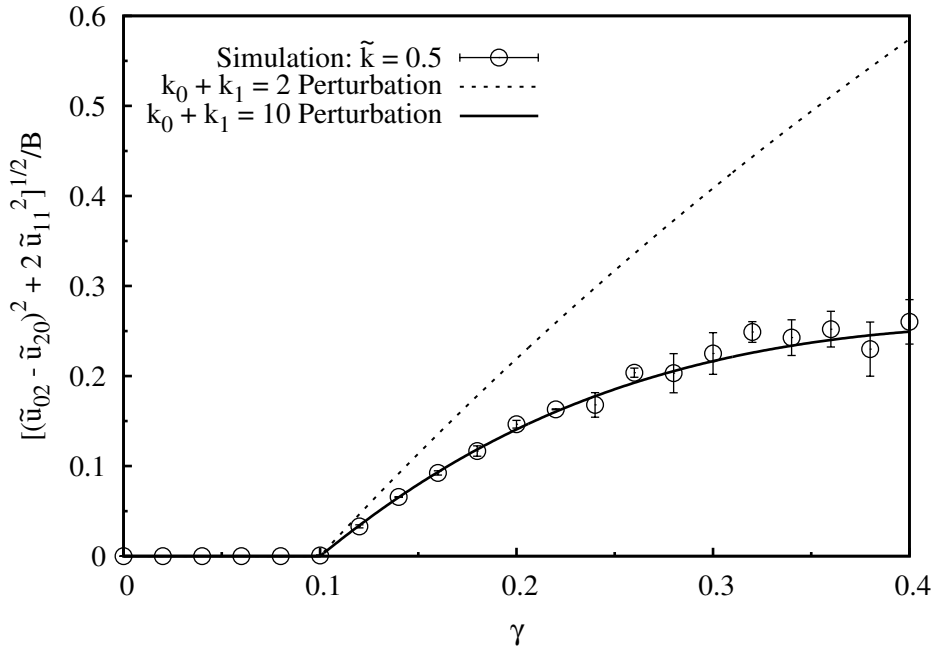


Figure 7.13: Projection of $\tilde{u}(x, t)$ on anisotropic basis function with $k_0+k_1=2$. Parameters: same as Figure 7.10.

optimal for the another bump. It makes the expansion of another bump less efficient.

Since either STD or local subtractive inhibition can drive the neuronal activity profile to move spontaneously, the behavior of the neuronal activity profile under the influence of external input should be similar to that in one-dimensional CANN with STD. For example, the dynamics driving spontaneous may enable delay compensation in 2D CANN with STD or local subtractive inhibition. Also, temporal modulation reported in the last chapter can happen in 2D CANNs with STD or local subtractive inhibition. However, since there is an extra dimension, the degree of freedom of the dynamics of the neuronal activity profile is higher due the symmetry of the neural field. For example, during the tracking process, oscillation of the center of mass of the neuronal activity profile along the direction perpendicular to the tracking direction may happen. Property of the neuronal activity profile in 2D CANNs under influences of STD, local subtractive inhibition and an external input will be an open question to be addressed in the future.

Chapter 8

Conclusion

In this thesis, I have presented our analyses on continuous attractor neural networks (CANNs) with dynamical synapses. The family of models named continuous attractor neural networks are models to simplify the neural process by neuronal activities (or neuronal firing rate). CANNs can support a continuous family of neuronal activity states. Neurons in the system have their own preferred stimuli. Their firing rates are Gaussian-like functions of external stimuli. The firing rate reaches maximum when the external stimulus matches the preferred stimulus of the neuron. So, neuronal firing rate profiles of CANNs responding to an external stimulus is a bump-shaped function of preferred stimuli of neurons (c.f. Figure 1.2).

Throughout the thesis, I present my work on a specific model (c.f. Eqs. (2.1) - (2.3)) and its variants. The major results of this model should apply to other similar models. The most important factor is the local spatial structure of the system. Other models with translationally invariant couplings can also support a family of attractor states and share similar qualitative properties of our specific model. In Chapter 2, I have reviewed the work on the intrinsic dynamics of CANNs. We used the perturbative method to analyze the stability of attractor profiles against various modes of distortions. By using this method, we can also predict the tracking dynamics of the attractor bump states.

Most simulations of neural networks can be easily done on modern computers. Perturbative analysis seems to be a relatively inefficient method to study properties of CANNs. However, by doing perturbative analysis, we can see the interaction between different modes of distortions. This enables us to figure out which mode is important to obtain good enough predictions. For example, in Figure 4.2, the lowest order prediction of the decay of bump height cannot determine the right time span of the plateau state. However, after adding the mode corresponding to changes in width, the prediction works well. It shows that the mode corresponding to width should be included in the theory and it is important to the evolution of dynamical variables.

Due to the physical and chemical conditions of chemical synapses, the synaptic efficacies depend on the firing history of presynaptic neurons in a short-term time window. After a spike arrives at the terminal of an axon, the terminal of the axon will release neurotransmitters. Those neurotransmitters will diffuse to the postsynaptic side to cause the opening of ion channels. Opened ion channels can further cause changes in the membrane potential of the postsynaptic neuron. Since the timescale of the recovery of neurotransmitters is significantly longer than that of synaptic currents, it causes a short-term degradation in the synaptic efficacy between neurons. This phenomenon is called short-term synaptic depression (STD). In 2012, we have reported that CANNs with STD may have various instability (c.f. Chapter 3). If the degree of STD is not significant, the steady state of the network will be static, which is similar to that without STD. If the degree of STD is moderate, the effect of STD can drive the network states to move spontaneously. In Chapter 5, I have shown that this translationally instability can modify the tracking dynamics of the network state against a moving stimulus. If the degree of STD is about right, the network activity can track the moving stimulus almost on-time. If the degree of STD is even larger, the network activity can overtake the moving stimulus. This is called ‘anticipatory tracking’. We proposed that this anticipatory tracking can be used to account for the anticipatory behavior of the head direction neurons as shown by their temporal difference between anterior thalamus (ATN) and postsubiculum (PoS) reported by Taube *et al.* [31]. The prediction by our model is plotted in Figure 5.7 and is comparable with the anticipatory time analyzed by Goodridge *et al.* [32].

Also, STD enables a parameter region, in the silent phase just outside static phase, that supports the neuronal activity profile for a relative longer time, c.f. Figure 4.2. Those temporally sustained states are called plateau states. These plateau states can last for a period of the order of magnitude of 100 ms. The plateau states can account for the iconic memory in the nervous system.

Apart from the translationally instability and plateau states, STD can also make periodic excitements of neuronal activity happen. In Chapter 6, I presented a mechanism of how periodic excitement of neuronal activity (population spikes) can enhance the resolution in discrimination tasks. In the parameter region for population spikes, for a single stimulus, the neuronal activity profile gets excited periodically. Each excitement of neuronal activity is bump-shaped and centered at the external stimulus. For two stimuli, the neuronal activity profile can center at one of the stimuli at the beginning. However, due to the effect of STD, the concentration of neurotransmitter is higher in the neighborhood of another stimulus. As a result, the next population spike will be likely to appear at the position of another stimulus. As a result, the neuronal activity

profile can center at the two stimuli in turns. We say that the network can represent two stimuli simultaneously. The behavior that the network can switch from one stimulus to another shows that ‘temporal modulation’ can be used to encode information. Kilpatrick also shows that STD can enable perceptual multistability such that the neural network can represent two stimuli in turns [53]. The temporal modulation enables CANNs to represent two stimuli, although the two stimuli may differ by less than a tuning width from each other. We have also found that the predictions by our model are highly comparable to experimental results, as shown in Figures 6.6 and 6.7.

Short-term synaptic depression is not the only mechanism to make synapses dynamic. After a spike, the concentration of calcium ions will be increased to release neurotransmitters. After releases, the concentration of calcium ions is still relatively high. It makes the release probability of neurotransmitters caused by the next spike to raise. As a result, this process makes the synaptic efficacy between two neurons increases after spikes. This effect is called short-term synaptic facilitation (STF). Because STF always strengthens the synaptic coupling between neurons where they are active, STF always stabilize the neuronal activity states. In Figure 4.4, I have shown that STF can slow down the tracking dynamics compared with CANN without STF. This intrinsic dynamics of STF can reduce the effect of noises, as shown in Figures 4.5 and 4.6.

Two-dimensional continuous attractor neural networks (2D CANNs) with short-term synaptic depression (STD) and local subtractive inhibition are also studied in this thesis. I found that the intrinsic dynamics of these two systems are similar. Also, I have obtained the speed of spontaneous motions of bump-shaped states in two-dimensional neural fields, which is not available in the literature.

All in all, CANNs are simplified models to describe neural systems that use localized bump-shaped neuronal activities to represent continuous information. These models are useful. In this thesis, I have presented my work on CANNs with dynamical synapses. It shows that CANNs with dynamical synapses have rich dynamical properties, and are able to account for experimental observations such as the graceful degradation of iconic memory, delay compensation and enhanced resolution in transparent motion.

We can see that the different applications proposed in the thesis correspond to different parameter regions on the phase diagram. We argue that, although behaviors of neuronal networks can be summarized by the phase diagram, different brain functions require different dynamical properties to achieve various purposes. Brain regions experimentally found to correspond to the different brain functions discussed in the thesis are different. It is natural that those brain functions correspond to different parameters on

the phase diagram. We propose that the nervous system can acquire right parameters through learning or/and evolution.

Dynamical synapse, especially short-term synaptic depression (STD), is relevant to many aspects of the nervous system. Micro-saccade is one phenomenon possibly to be relevant to STD. Micro-saccades are small eye movements to avoid neural adaptation in the visual cortex [30]. STD could be a candidate of the neural adaptation mechanism [54]. Gur *et al.* reported that receptive field of neurons in area V1 correspond to retinal position [55]. So, the dynamics driven by STD should also be important during the eye movement process. STD is also related to stability issue of associate memory neural network [56].

As mentioned in Chapter 7, in a 2D CANN, translational instability driven by STD or local subtractive inhibition can achieve similar behaviors that observed in 1D CANNs with STD. However, in 2D CANNs, there is an additional dimension so that the degree of freedom of the neuronal activity profile will be higher. In the scenario of tracking a moving stimulus, the stability issue is to be addressed in the future. Because the center of mass of the neuronal activity profile may oscillate along the direction perpendicular to the direction of the moving stimulus. Also, due to the additional dimension, the stability issue for population spikes will be more complicated.

The perturbative approach is a powerful method to analyze system with localized state function, especially neural systems. In the future, it could be applied on other neural models having localized neuronal activity to study their general behavior and intrinsic dynamics.

Appendix A

Consistency with the Model of Tsodyks, Pawelzik, and Markram

A.1 The Model of Tsodyks, Pawelzik, and Markram

Our modeling of the dynamics of STP is consistent with the phenomenological model proposed by Tsodyks et al. (1998). They modeled STD by considering p as the fraction of usable neurotransmitters, and STF by introducing U_0 as the release probability of the neurotransmitters. The release probability U_0 relaxes to a nonzero constant, u_{rest} , but is enhanced at the arrival of a spike by an amount equal to $u_0(1-U_0)$. Hence, the dynamics of p and U_0 are given by

$$\tau_s \frac{\partial u}{\partial t} = I_{\text{ext}} - u + \rho \int dx' J(x-x') p(x') U_1(x') r(x'), \quad (\text{A.1})$$

$$\tau_d \frac{\partial p}{\partial t} = 1 - p - U_1 \tau_d p r, \quad (\text{A.2})$$

$$\tau_f \frac{\partial U_0}{\partial t} = u_{\text{rest}} - U_0 + u_0 (1 - U_0) \tau_f r, \quad (\text{A.3})$$

where $U_1 \equiv u_0 + U_0(1-u_0)$ is the release probability of the neurotransmitters after the arrival of a spike. The x and t dependence of u , p , r , and U_0 are omitted in the above equations for convenience. Eliminating U_0 , we obtain from Eq. (A.3).

$$\frac{\partial U_1}{\partial t} = \frac{u_0 + (1 - u_0) u_{\text{rest}} - U_1}{\tau_f} + u_0 (1 - U_1) r. \quad (\text{A.4})$$

Substituting α , β and f via $\alpha = u_0$, $\beta = u_0 + (1 - u_0) u_{\text{rest}}$, $U_1 = [u_0 + (1 - u_0) u_{\text{rest}}] (1 + f)$, $f_{\max} = (1 - \beta) / \beta$, we obtain Eqs. (4.2) and (4.3). Rescaling βJ to J , we obtain Eq. (4.1). α and β are the STF and STD parameters, respectively, subject to $\beta \geq \alpha$.

Appendix B

Recursions of C_{nm}^k , D_{nml}^k , E_{nm}^k and F_{nml}^k

B.1 Recursions

From chapter 4, there are constants defined by

$$C_{nm}^k = \int dx \psi_k(x) \int dx' \tilde{J}(x, x') \psi_n(x') \psi_m(x') \quad (B.1)$$

$$D_{nml}^k = \int dx \psi_k(x) \int dx' \tilde{J}(x, x') \psi_n(x') \psi_m(x') \varphi_l(x') \quad (B.2)$$

$$E_{nm}^k = \int dx \varphi_k(x) \psi_n(x) \psi_m(x) \quad (B.3)$$

$$F_{nml}^k = \int dx \psi_k(x) \psi_n(x) \psi_m(x) \varphi_l(x), \quad (B.4)$$

where $\psi_n(x)$ and $\varphi_n(x)$ are defined by Eqs. (4.14) and (4.15). By using integration by parts and

$$H_{n+1}(x) = 2xH_n(x) - 2nH_{n-1}(x), \quad (B.5)$$

$$H'_n(x) = 2nH_{n-1}(x), \quad (B.6)$$

one can derive recursion relations of C_{nm}^k , D_{nml}^k , E_{nm}^k and F_{nml}^k :

$$C_{nm}^k = \frac{1}{2} \left(\sqrt{\frac{n}{k}} C_{n_1 m}^{k_1} + \sqrt{\frac{m}{k}} C_{n m_1}^{k_1} \right), \quad (B.7)$$

$$C_{nm}^k = -\frac{1}{4} \sqrt{\frac{n_1}{n}} C_{n_2 m}^k + \frac{3}{4} \sqrt{\frac{m}{n}} C_{n_1 m_1}^k + \frac{1}{2} \sqrt{\frac{k}{n}} C_{n_1 m}^{k_1}, \quad (B.8)$$

$$C_{nm}^k = -\frac{1}{4} \sqrt{\frac{m_1}{m}} C_{n m_2}^k + \frac{3}{4} \sqrt{\frac{n}{m}} C_{n_1 m_1}^k + \frac{1}{2} \sqrt{\frac{k}{m}} C_{n m_1}^{k_1}, \quad (B.9)$$

where $n_1 \equiv n - 1$ and $m_2 \equiv m - 2$ etc. in the indices. Similarly,

$$D_{nml}^k = \frac{2}{7} \left(\sqrt{\frac{n}{k}} D_{n_1 ml}^{k_1} + \sqrt{\frac{m}{k}} D_{nm_1 l}^{k_1} + \sqrt{2} \sqrt{\frac{l}{k}} D_{nml_1}^{k_1} \right) - \frac{1}{7} \sqrt{\frac{k_1}{k}} D_{nml}^{k_2}, \quad (\text{B.10})$$

$$D_{nml}^k = \frac{6}{7} \left(\sqrt{\frac{1}{2}} \sqrt{\frac{n}{l}} D_{n_1 ml_1}^k + \sqrt{\frac{1}{2}} \sqrt{\frac{m}{l}} D_{nm_1 l_1}^k + \sqrt{\frac{2}{3}} \sqrt{\frac{k}{l}} D_{nml_1}^{k_1} \right) - \frac{1}{7} \sqrt{\frac{l_1}{l}} D_{nm_2 l}^k, \quad (\text{B.11})$$

$$D_{nml}^k = -\frac{4}{7} \sqrt{\frac{n_1}{n}} D_{n_2 ml}^k + \frac{3}{7} \sqrt{\frac{m}{n}} D_{n_1 m_1 l}^k + \frac{3\sqrt{2}}{7} \sqrt{\frac{l}{n}} D_{n_1 ml_1}^k + \frac{2}{7} \sqrt{\frac{k}{n}} D_{n_1 ml}^{k_1}, \quad (\text{B.12})$$

$$D_{nml}^k = -\frac{4}{7} \sqrt{\frac{m_1}{m}} D_{nm_2 l}^k + \frac{3}{7} \sqrt{\frac{n}{m}} D_{n_1 m_1 l}^k + \frac{3\sqrt{2}}{7} \sqrt{\frac{l}{m}} D_{nm_1 l_1}^k + \frac{2}{7} \sqrt{\frac{k}{m}} D_{nm_1 l}^{k_1}, \quad (\text{B.13})$$

$$E_{nm}^k = \frac{1}{\sqrt{2}} \left(\sqrt{\frac{n}{k}} E_{n_1 m}^{k_1} + \sqrt{\frac{m}{k}} E_{nm_1}^{k_1} \right), \quad (\text{B.14})$$

$$E_{nm}^k = -\frac{1}{2} \sqrt{\frac{n_1}{n}} E_{n_2 m}^k + \frac{1}{2} \sqrt{\frac{m}{n}} E_{n_1 m_1}^k + \frac{1}{\sqrt{2}} \sqrt{\frac{k}{n}} E_{n_1 m}^{k_1}, \quad (\text{B.15})$$

$$E_{nm}^k = -\frac{1}{2} \sqrt{\frac{m_1}{m}} E_{nm_2}^k + \frac{1}{2} \sqrt{\frac{n}{m}} E_{n_1 m_1}^k + \frac{1}{\sqrt{2}} \sqrt{\frac{k}{m}} E_{nm_1}^{k_1}, \quad (\text{B.16})$$

$$F_{nml}^k = \frac{\sqrt{2}}{3} \left(\sqrt{\frac{n}{k}} F_{n_1 ml}^{k_1} + \sqrt{\frac{m}{k}} F_{nm_1 l}^{k_1} + \sqrt{2} \sqrt{\frac{l}{k}} F_{nml_1}^{k_1} \right) - \frac{1}{3} \sqrt{\frac{k_1}{k}} F_{nml}^{k_2}, \quad (\text{B.17})$$

$$F_{nml}^k = \frac{\sqrt{2}}{3} \left(\sqrt{\frac{n}{l}} F_{n_1 ml_1}^k + \sqrt{\frac{m}{l}} F_{nm_1 l_1}^k + \sqrt{2} \sqrt{\frac{k}{l}} F_{nml_1}^{k_1} \right) - \frac{1}{3} \sqrt{\frac{l_1}{l}} F_{nm_2 l}^k, \quad (\text{B.18})$$

$$F_{nml}^k = -\frac{2}{3} \sqrt{\frac{n_1}{n}} F_{n_2 ml}^k + \frac{1}{3} \sqrt{\frac{m}{n}} F_{n_1 m_1 l}^k + \frac{\sqrt{2}}{3} \left(\sqrt{\frac{l}{n}} F_{n_1 ml_1}^k + \sqrt{\frac{k}{n}} F_{n_1 ml}^{k_1} \right), \quad (\text{B.19})$$

$$F_{nml}^k = -\frac{2}{3} \sqrt{\frac{m_1}{m}} F_{nm_2 l}^k + \frac{1}{3} \sqrt{\frac{n}{m}} F_{n_1 m_1 l}^k + \frac{\sqrt{2}}{3} \left(\sqrt{\frac{l}{m}} F_{nm_1 l_1}^k + \sqrt{\frac{k}{m}} F_{nm_1 l}^{k_1} \right). \quad (\text{B.20})$$

Since C_{00}^0 , D_{000}^0 , E_{00}^0 and F_{000}^0 can be calculated explicitly, all other C_{nm}^k , D_{nml}^k , E_{nm}^k and F_{nml}^k can be deduced.

Appendix C

Derivation of $\tilde{\beta}_{\text{perfect}}$

C.1 First Order Perturbation Equations

For the lowest order analysis, $k = 1$ perturbation, we approximate $\tilde{u}(x, t)$ and $p(x, t)$ by

$$\tilde{u}(x, t) = \tilde{u}_0(t) \exp\left(-\frac{|x - z(t)|^2}{4a^2}\right) \quad (\text{C.1})$$

$$p(x, t) = 1 - p_0(t) \exp\left(-\frac{|x - z(t)|^2}{2a^2}\right) + p_1(t) \left(\frac{x - z(t)}{a}\right) \exp\left(-\frac{|x - z(t)|^2}{2a^2}\right) \quad (\text{C.2})$$

Substituting these two approximations into Eq. (5.1) results in the following terms:

- (a) The time derivative of $\tilde{u}(x, t)$ given by

$$\frac{d\tilde{u}}{dt}(x, t) = \tau_s \frac{d\tilde{u}_0}{dt} \exp\left[-\frac{(x - z)^2}{4a^2}\right] + \tilde{u}_0 \left(\frac{\tau_s}{2a}\right) \frac{dz}{dt} \left(\frac{x - z}{a}\right) \exp\left[-\frac{(x - z)^2}{4a^2}\right]. \quad (\text{C.3})$$

(b) The integral in the right hand side of Eq. (5.1) given by

$$\begin{aligned}
& \frac{1}{B} \int dx' \tilde{J}(x - x') p(x', t) \tilde{u}(x', t)^2 \\
= & \frac{\tilde{u}_0^2}{B\sqrt{2\pi}a} \int dx' \exp\left[-\frac{(x-x')^2}{2a^2}\right] \exp\left[-\frac{(x'-z)^2}{2a^2}\right] \\
& - \frac{\tilde{u}_0^2}{B\sqrt{2\pi}a} p_0 \int dx' \exp\left[-\frac{(x-x')^2}{2a^2}\right] \exp\left[-\frac{(x'-z)^2}{a^2}\right] \\
& + \frac{\tilde{u}_0^2}{B\sqrt{2\pi}a} p_1 \int dx' \exp\left[-\frac{(x-x')^2}{2a^2}\right] \left(\frac{x'-z}{a}\right) \exp\left[-\frac{(x-z)^2}{a^2}\right] \\
= & \frac{\tilde{u}_0^2}{B\sqrt{2}} \exp\left[-\frac{(x-z)^2}{4a^2}\right] - \frac{\tilde{u}_0^2}{B\sqrt{3}} p_0 \exp\left[-\frac{(x-z)^2}{3a^2}\right] \\
& + \frac{\tilde{u}_0^2}{B3\sqrt{3}} p_1 \left(\frac{x-z}{a}\right) \exp\left[-\frac{(x-z)^2}{3a^2}\right]. \tag{C.4}
\end{aligned}$$

Since the basis functions are proportional to $\exp[-(x-z)^2/(4a^2)]$ and $[(x-z)/a] \exp[-(x-z)^2/(4a^2)]$, we multiply both sides of Eq. (5.1) by $\exp[-(x-z)^2/(4a^2)]$ and integrate over x . This results in the equation

$$\tau_s \frac{d\tilde{u}_0}{dt} = \frac{\tilde{u}_0^2}{B\sqrt{2}} \left(1 - p_0 \sqrt{\frac{4}{7}}\right) - \tilde{u}_0 + \tilde{A} e^{-\frac{(z_0-z)^2}{8a^2}}. \tag{C.5}$$

Similarly, multiplying both sides of Eq. (5.1) by $[(x-z)/a] \exp[-(x-z)^2/(4a^2)]$ and integrating over x , we obtain

$$\frac{\tau_s}{2a} \frac{dz}{dt} = \frac{\tilde{u}_0^2}{B} \left(\frac{2}{7}\right)^{\frac{3}{2}} p_1 + \frac{\tilde{A}}{2\tilde{u}} \left(\frac{z_0-z}{a}\right) e^{-\frac{(z_0-z)^2}{8a^2}}. \tag{C.6}$$

Respectively, multiplying both sides of Eq. (5.2) by $\exp[-(x-z)^2/(2a^2)]$ and $[(x-z)/a] \exp[-(x-z)^2/(2a^2)]$ and integrating over x , we obtain

$$\tau_s \frac{dp_0}{dt} = \frac{\tau_s}{\tau_d} \left[\frac{\tilde{\beta}\tilde{u}_0^2}{B} \left(1 - p_0 \sqrt{\frac{2}{3}}\right) - p_0 \right] - \frac{\tau_s p_1}{2a} \frac{dz}{dt}, \tag{C.7}$$

$$\frac{\tau_s}{p_0} \frac{dp_1}{dt} = -\frac{\tau_s}{\tau_d} \left[1 + \frac{\tilde{\beta}\tilde{u}_0^2}{B} \left(\frac{2}{3}\right)^{\frac{2}{3}} \right] \frac{p_1}{p_0} + \frac{\tau_s}{a} \frac{dz}{dt}. \tag{C.8}$$

C.2 Derivation of The Perfect Tracking Solution

For perfect tracking, we have $z = z_0$. At the steady state, $d\tilde{u}_0/dt$, dp_0/dt and dp_1/dt vanish, and $dz/dt = v$. Eqs. (C.5) to (C.8) reduce to

$$\tilde{u}_0 = \frac{\tilde{u}_0^2}{\sqrt{2}B} \left(1 - p_0 \sqrt{\frac{4}{7}} \right) + \tilde{A}, \quad (\text{C.9})$$

$$\frac{v\tau_s}{a} = \frac{2\tilde{u}_0}{B} \left(\frac{2}{7} \right)^{\frac{3}{2}} p_1, \quad (\text{C.10})$$

$$p_0 = \frac{\tilde{\beta}\tilde{u}_0^2}{B} \left(1 - p_0 \sqrt{\frac{2}{3}} \right) - \frac{v\tau_d}{2a} p_1, \quad (\text{C.11})$$

$$\frac{v\tau_d}{a} p_0 = \left[1 + \frac{\tilde{\beta}\tilde{u}_0^2}{B} \left(\frac{2}{3} \right)^{\frac{3}{2}} \right] p_1. \quad (\text{C.12})$$

From Eq. (C.9), we have

$$\frac{\tilde{u}_0}{B} = \frac{\sqrt{2} \left(1 - \frac{\tilde{A}}{\tilde{u}_0} \right)}{1 - \sqrt{\frac{4}{7}} p_0}. \quad (\text{C.13})$$

Substituting this expression into Eq. (C.10) yields

$$\frac{v\tau_s}{a} = \left(\frac{4}{7} \right)^{\frac{3}{2}} p_1 \frac{1 - \frac{\tilde{A}}{\tilde{u}_0}}{1 - \sqrt{\frac{4}{7}} p_0}. \quad (\text{C.14})$$

Using Eq. (C.12) to eliminate p_1 , we obtain an equation for p_0 ,

$$\frac{v\tau_s}{a} = \left(\frac{4}{7} \right)^{\frac{3}{2}} \frac{1 - \frac{\bar{A}}{\tilde{u}_0}}{1 - \sqrt{\frac{4}{7}} p_0} \frac{v\tau_d}{a} \frac{p_0}{1 + \frac{\tilde{\beta}\tilde{u}_0^2}{B} \left(\frac{2}{3} \right)^{\frac{3}{2}}}. \quad (\text{C.15})$$

The solution for p_0 is

$$p_0 = \frac{\frac{\tau_s}{\tau_d} \left[1 + \frac{\tilde{\beta}\tilde{u}_0^2}{B} \left(\frac{2}{3} \right)^{\frac{3}{2}} \right]}{\left(\frac{4}{7} \right)^{\frac{3}{2}} \left(1 - \frac{\bar{A}}{\tilde{u}_0} \right) + \sqrt{\frac{4}{7} \frac{\tau_s}{\tau_d} \left[1 + \frac{\tilde{\beta}\tilde{u}_0^2}{B} \left(\frac{2}{3} \right)^{\frac{3}{2}} \right]}}. \quad (\text{C.16})$$

Substituting Eq. (C.16) into Eq. (C.13), we obtain the expression for \tilde{u}_0/B , given by

$$\frac{\tilde{u}_0}{B} = \sqrt{2} \left(1 - \frac{\tilde{A}}{\tilde{u}_0} \right) + \frac{7}{\sqrt{8}} \frac{\tau_s}{\tau_d} \left[1 + \frac{\tilde{\beta}\tilde{u}_0^2}{B} \left(\frac{2}{3} \right)^{\frac{3}{2}} \right]. \quad (\text{C.17})$$

Substituting Eq. (C.17) into Eq. (C.10), we obtain an expression for $v\tau_s/(ap_1)$. Substituting Eq. (C.16) into Eq. (C.11), we obtain an expression for $v\tau_s p_1/a$. The quotient and product of these two expressions yield, respectively,

$$p_1 = \sqrt{\frac{2\tau_s}{\tau_d}} \frac{\sqrt{\frac{\tilde{\beta}\tilde{u}_0^2}{B} \left(\frac{4}{7}\right)^{\frac{3}{2}} \left(1 - \frac{\tilde{A}}{\tilde{u}_0}\right)} - \frac{\tau_s}{\tau_d} \left[1 + \frac{\tilde{\beta}\tilde{u}_0^2}{B} \left(\frac{2}{3}\right)^{\frac{3}{2}}\right] \left[1 + \frac{\tilde{\beta}\tilde{u}_0^2}{B} \left(\sqrt{\frac{2}{3}} - \sqrt{\frac{4}{7}}\right)\right]}{\left(\frac{4}{7}\right)^{\frac{3}{2}} \left(1 - \frac{\tilde{A}}{\tilde{u}_0}\right) + \sqrt{\frac{4}{7}} \frac{\tau_s}{\tau_d} \left[1 + \frac{\tilde{\beta}\tilde{u}_0^2}{B} \left(\frac{2}{3}\right)^{\frac{3}{2}}\right]}, \quad (\text{C.18})$$

$$\frac{v\tau_s}{a} = \sqrt{2 \frac{\tau_s}{\tau_d} \left\{ \frac{\tilde{\beta}\tilde{u}_0^2}{B} \left(\frac{4}{7}\right)^{\frac{3}{2}} \left(1 - \frac{\tilde{A}}{\tilde{u}_0}\right) - \frac{\tau_s}{\tau_d} \left[1 + \frac{\tilde{\beta}\tilde{u}_0^2}{B} \left(\frac{2}{3}\right)^{\frac{3}{2}}\right] \left[1 + \frac{\tilde{\beta}\tilde{u}_0^2}{B} \left(\sqrt{\frac{2}{3}} - \sqrt{\frac{4}{7}}\right)\right] \right\}}. \quad (\text{C.19})$$

Equations (C.16) to (C.19) enable us to express the variables p_0 , \tilde{u}_0/B , p_1 and $v\tau_s/a$ in terms of the parameters $\tilde{\beta}\tilde{u}_0^2/B$, τ_s/τ_d and \tilde{A}/\tilde{u}_0 . Since \tilde{u}_0^2/B is the rescaled firing rate at the peak of the bump, the parameter $\tilde{\beta}\tilde{u}_0^2/B$ is the rate of neurotransmitter consumption at the bump peak after rescaling.

Real solutions exist only if the expression on the right hand side of Eq. (C.19) is real. This implies that

$$\begin{aligned} \frac{\tilde{\beta}\tilde{u}_0^2}{B} &\geq 2 \left\{ \sqrt{\frac{64}{343}} \frac{\tau_d}{\tau_s} \left(1 - \frac{\tilde{A}}{\tilde{u}_0}\right) - \sqrt{\frac{8}{27}} - \sqrt{\frac{2}{3}} + \sqrt{\frac{4}{7}} \right. \\ &\quad \left. + \sqrt{\left[\sqrt{\frac{64}{343}} \frac{\tau_d}{\tau_s} \left(1 - \frac{\tilde{A}}{\tilde{u}_0}\right) - \sqrt{\frac{8}{27}} - \sqrt{\frac{2}{3}} + \sqrt{\frac{4}{7}} \right]^2 - 4 \sqrt{\frac{8}{27}} \left(\sqrt{\frac{2}{3}} - \sqrt{\frac{4}{7}}\right)} \right\}^{-1}. \end{aligned} \quad (\text{C.20})$$

Perfect tracking in the limit of vanishing stimulus speed is obtained by equating $v\tau_s/a$ to zero. Hence the expression for $\tilde{\beta}_{\text{perfect}}\tilde{u}_0^2/B$ is given by the right hand side of Eq. (C.20). Remarkably, when \tilde{A} approaches 0, this expression becomes identical to the phase boundary separating the static and metastatic phases in the intrinsic phase diagram of the neural field [24].

C.3 Deviations from Perfect Tracking

For the case that the displacement s/a is non-vanishing but small, Eqs. (C.9) to (C.12) become

$$\tilde{u}_0 = \frac{\tilde{u}_0^2}{\sqrt{2}B} \left(1 - p_0 \sqrt{\frac{4}{7}} \right) + \tilde{A}, \quad (\text{C.21})$$

$$\frac{v\tau_s}{a} = \frac{2\tilde{u}_0}{B} \left(\frac{2}{7} \right)^{\frac{3}{2}} p_1 - \frac{\tilde{A}}{\tilde{u}_0} \left(\frac{s}{a} \right), \quad (\text{C.22})$$

$$p_0 = \frac{\tilde{\beta}\tilde{u}_0^2}{B} \left(1 - p_0 \sqrt{\frac{2}{3}} \right) - \frac{v\tau_d}{2a} p_1, \quad (\text{C.23})$$

$$\frac{v\tau_d}{a} p_0 = \left[1 + \frac{\tilde{\beta}\tilde{u}_0^2}{B} \left(\frac{2}{3} \right)^{\frac{3}{2}} \right] p_1. \quad (\text{C.24})$$

Since τ_s only appears in Eq. (C.22), we can recover the equations (C.9) to (C.12) if we substitute τ_s by $\tau_s \left[1 + \left(\tilde{A}/\tilde{u}_0 \right) (s/(v\tau_s)) \right]$. Hence the solution is given by

$$\frac{\tilde{u}_0}{B} = \sqrt{2} \left(1 - \frac{\tilde{A}}{\tilde{u}_0} \right) + \frac{7}{\sqrt{8}} \frac{\tau_s}{\tau_d} \left[1 + \frac{\tilde{\beta}\tilde{u}_0^2}{B} \left(\frac{2}{3} \right)^{\frac{3}{2}} \right] \left(1 + \frac{\tilde{A}}{\tilde{u}_0} \frac{s}{v\tau_s} \right), \quad (\text{C.25})$$

$$p_0 = \frac{\frac{\tau_s}{\tau_d} \left[1 + \frac{\tilde{\beta}\tilde{u}_0^2}{B} \left(\frac{2}{3} \right)^{\frac{3}{2}} \right]}{\left(\frac{4}{7} \right)^{\frac{3}{2}} \left(\frac{1 - \tilde{A}/\tilde{u}_0}{1 + \tilde{A}s/(\tilde{u}_0 v\tau_s)} \right) + \sqrt{\frac{4}{7}} \frac{\tau_s}{\tau_d} \left[1 + \frac{\tilde{\beta}\tilde{u}_0^2}{B} \left(\frac{2}{3} \right)^{\frac{3}{2}} \right]}, \quad (\text{C.26})$$

$$p_1 = \sqrt{2 \frac{\tau_s}{\tau_d}} \frac{\sqrt{\frac{\tilde{\beta}\tilde{u}_0^2}{B} \left(\frac{4}{7} \right)^{\frac{3}{2}} \left(\frac{1 - \tilde{A}/\tilde{u}_0}{1 + \tilde{A}s/(\tilde{u}_0 v\tau_s)} \right)} - \frac{\tau_s}{\tau_d} \left[1 + \frac{\tilde{\beta}\tilde{u}_0^2}{B} \left(\frac{2}{3} \right)^{\frac{3}{2}} \right] \left[1 + \frac{\tilde{\beta}\tilde{u}_0^2}{B} \left(\sqrt{\frac{2}{3}} - \sqrt{\frac{4}{7}} \right) \right]}}{\left(\frac{4}{7} \right)^{\frac{3}{2}} \left(\frac{1 - \tilde{A}/\tilde{u}_0}{1 + \tilde{A}s/(\tilde{u}_0 v\tau_s)} \right) + \sqrt{\frac{4}{7}} \frac{\tau_s}{\tau_d} \left[1 + \frac{\tilde{\beta}\tilde{u}_0^2}{B} \left(\frac{2}{3} \right)^{\frac{3}{2}} \right]}, \quad (\text{C.27})$$

$$\begin{aligned} \frac{v\tau_s}{a} &= \left\{ 2 \frac{\tau_s}{\tau_d} \left\{ \frac{\tilde{\beta}\tilde{u}_0^2}{B} \left(\frac{4}{7} \right)^{\frac{3}{2}} \left(\frac{1 - \tilde{A}/\tilde{u}_0}{1 + \tilde{A}s/(\tilde{u}_0 v\tau_s)} \right) \right. \right. \\ &\quad \left. \left. - \frac{\tau_s}{\tau_d} \left[1 + \frac{\tilde{\beta}\tilde{u}_0^2}{B} \left(\frac{2}{3} \right)^{\frac{3}{2}} \right] \left[1 + \frac{\tilde{\beta}\tilde{u}_0^2}{B} \left(\sqrt{\frac{2}{3}} - \sqrt{\frac{4}{7}} \right) \right] \right\} \right\}^{\frac{1}{2}}. \end{aligned} \quad (\text{C.28})$$

We can invert Eq. (C.28) to yield an expression for s/a , which reads

$$\frac{s}{a} = -\frac{\tilde{u}_0}{\tilde{A}} \frac{v\tau_s}{a} \left\{ 1 - \frac{2\frac{\tau_s}{\tau_d} \frac{\tilde{\beta}\tilde{u}_0^2}{B} \left(\frac{4}{7}\right)^{\frac{3}{2}} \left(1 - \frac{\tilde{A}}{\tilde{u}_0}\right)}{\left(\frac{v\tau_s}{a}\right)^2 + 2\left(\frac{\tau_s}{\tau_d}\right)^2 \left[1 + \frac{\tilde{\beta}\tilde{u}_0^2}{B} \left(\frac{2}{3}\right)^{\frac{3}{2}}\right] \left[1 + \frac{\tilde{\beta}\tilde{u}_0^2}{B} \left(\sqrt{\frac{2}{3}} - \sqrt{\frac{4}{7}}\right)\right]} \right\}. \quad (\text{C.29})$$

When $v\tau_s/a \ll 1$, we can approximate Eq. (C.29) by the series expansion

$$\begin{aligned} \frac{s}{a} \approx & -\frac{\tilde{u}_0}{\tilde{A}} \frac{v\tau_s}{a} \left\{ 1 - \frac{2\frac{\tau_s}{\tau_d} \frac{\tilde{\beta}\tilde{u}_0^2}{B} \left(\frac{4}{7}\right)^{\frac{3}{2}} \left(1 - \frac{\tilde{A}}{\tilde{u}_0}\right)}{2\left(\frac{\tau_s}{\tau_d}\right)^2 \left[1 + \frac{\tilde{\beta}\tilde{u}_0^2}{B} \left(\frac{2}{3}\right)^{\frac{3}{2}}\right] \left[1 + \frac{\tilde{\beta}\tilde{u}_0^2}{B} \left(\sqrt{\frac{2}{3}} - \sqrt{\frac{4}{7}}\right)\right]} \right. \\ & \left. + \frac{2\frac{\tau_s}{\tau_d} \frac{\tilde{\beta}\tilde{u}_0^2}{B} \left(\frac{4}{7}\right)^{3/2} \left(1 - \frac{\tilde{A}}{\tilde{u}_0}\right)}{\left\{2\left(\frac{\tau_s}{\tau_d}\right)^2 \left[1 + \frac{\tilde{\beta}\tilde{u}_0^2}{B} \left(\frac{2}{3}\right)^{3/2}\right] \left[1 + \frac{\tilde{\beta}\tilde{u}_0^2}{B} \left(\sqrt{\frac{2}{3}} - \sqrt{\frac{4}{7}}\right)\right]\right\}^2} \left(\frac{v\tau_s}{a}\right)^2 \right\}. \end{aligned} \quad (\text{C.30})$$

For the case of perfect tracking in the limit of vanishing stimulus speed, the lowest order term in Eq. (C.30) vanishes, and we have

$$\frac{s}{a} \approx -\frac{\tilde{u}_0}{2\tilde{A}} \frac{\tau_s}{\tau_d} \left[1 + \frac{\tilde{\beta}\tilde{u}_0^2}{B} \left(\frac{2}{3}\right)^{\frac{3}{2}}\right]^{-1} \left[1 + \frac{\tilde{\beta}\tilde{u}_0^2}{B} \left(\sqrt{\frac{2}{3}} - \sqrt{\frac{4}{7}}\right)\right]^{-1} \left(\frac{v\tau_s}{a}\right)^3. \quad (\text{C.31})$$

Hence we arrive at

$$\frac{s}{a} = -\frac{C}{2} \frac{\tilde{u}_0}{\tilde{A}} \frac{\tau_s}{\tau_d} \left(\frac{v\tau_d}{a}\right)^3 \quad (\text{C.32})$$

with

$$C = \left[1 + \frac{\tilde{\beta}\tilde{u}_0^2}{B} \left(\frac{2}{3}\right)^{\frac{3}{2}}\right]^{-1} \left[1 + \frac{\tilde{\beta}\tilde{u}_0^2}{B} \left(\sqrt{\frac{2}{3}} - \sqrt{\frac{4}{7}}\right)\right]^{-1}, \quad (\text{C.33})$$

which is less than 1. In latter stages of the information pathway where the stimulus signal has been filtered, weaker signals are considered untrackable. Hence we assume that \tilde{u}_0/\tilde{A} is not very large. Then Eq. (C.32) implies that for velocity ranges up to $v\tau_d/a \approx 1$, the lag of the bump is effectively zero in a velocity range proportional to $(\tau_d/\tau_s)^{1/3} \gg 1$.

When $\tilde{\beta} > \tilde{\beta}_{\text{perfect}}$, we are interested in analyzing the anticipatory time $\tau_{\text{ant}} = s/v$ in the limit of vanishing stimulus speed. From Eq. (C.29), we obtain

$$\frac{\tau_{\text{ant}}}{\tau_s} = \frac{\tilde{u}_0}{\tilde{A}} \left\{ \frac{2\frac{\tau_s}{\tau_d} \frac{\tilde{\beta}\tilde{u}_0^2}{B} \left(\frac{4}{7}\right)^{\frac{3}{2}} \left(1 - \frac{\tilde{A}}{\tilde{u}_0}\right)}{\left(\frac{v\tau_s}{a}\right)^2 + 2\left(\frac{\tau_s}{\tau_d}\right)^2 \left[1 + \frac{\tilde{\beta}\tilde{u}_0^2}{B} \left(\frac{2}{3}\right)^{\frac{3}{2}}\right] \left[1 + \frac{\tilde{\beta}\tilde{u}_0^2}{B} \left(\sqrt{\frac{2}{3}} - \sqrt{\frac{4}{7}}\right)\right]} - 1 \right\}. \quad (\text{C.34})$$

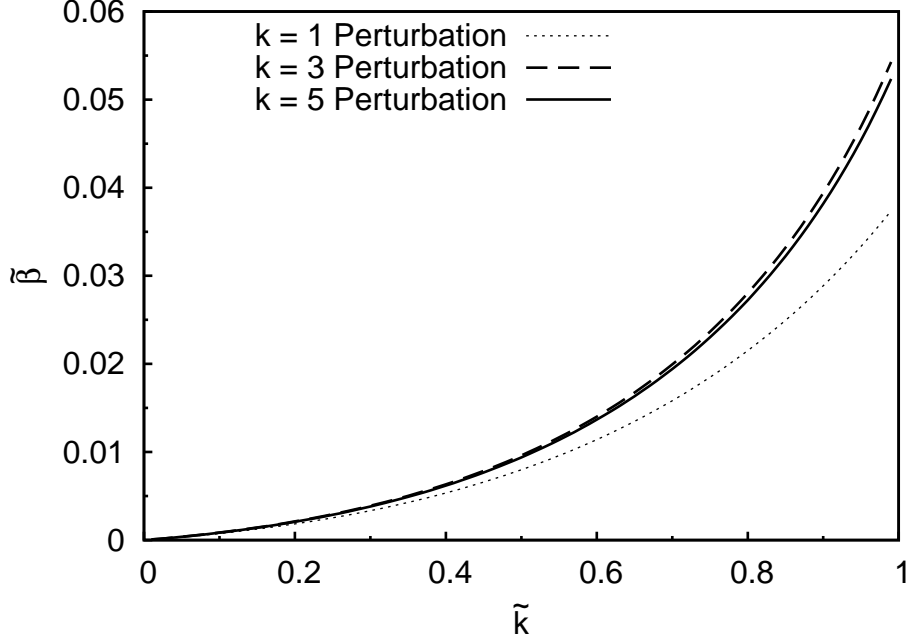


Figure C.1: Comparison of the contours of constant anticipatory time $10\tau_s$ between numerical solutions and the 1st order perturbation at $\tilde{A} = 1$.

To calculate the contours of constant anticipatory time, it is expedient to invert the relation (C.34) to obtain

$$1 - \frac{\tilde{A}}{\tilde{u}_0} = \frac{\left(\frac{\tau_{\text{ant}}}{\tau_d} + \frac{\tau_s}{\tau_d}\right) \left[1 + \frac{\tilde{\beta}\tilde{u}_0^2}{B} \left(\frac{2}{3}\right)^{\frac{3}{2}}\right] \left[1 + \frac{\tilde{\beta}\tilde{u}_0^2}{B} \left(\sqrt{\frac{2}{3}} - \sqrt{\frac{4}{7}}\right)\right]}{\frac{\tilde{\beta}\tilde{u}_0^2}{B} \left(\frac{4}{7}\right)^{\frac{3}{2}} + \frac{\tau_{\text{ant}}}{\tau_d} \left[1 + \frac{\tilde{\beta}\tilde{u}_0^2}{B} \left(\frac{2}{3}\right)^{\frac{3}{2}}\right] \left[1 + \frac{\tilde{\beta}\tilde{u}_0^2}{B} \left(\sqrt{\frac{2}{3}} - \sqrt{\frac{4}{7}}\right)\right]}. \quad (\text{C.35})$$

Hence for given values of \tilde{A} , τ_{ant}/τ_d and a range of the parameter $\tilde{\beta}\tilde{u}_0^2/B$, we can first calculate $1 - \tilde{A}/\tilde{u}_0$, then \tilde{u}_0 from $1 - \tilde{A}/\tilde{u}_0$, then \tilde{u}_0/B from Eq. (C.25). The corresponding \tilde{k} and $\tilde{\beta}$ can then be obtained from these parameters algebraically. As shown in Fig. C.1, comparison with numerical results indicates that the 1st order perturbation captures the trend that τ_{ant} increases with $\tilde{\beta}$. The predictions are rather accurate near the phase boundary, although deviations increase with increasing anticipatory time, probably due to the increasing significance of higher order distortions when the stimulus speed is high. More accurate predictions done with 11th order perturbation are shown in Figure 5.8.

Appendix D

Tracking Weak Moving Stimuli at the Natural Velocity

In the limit of strong stimulus amplitudes, we expect \tilde{u}_0 to be large. We can see that B , given by

$$B \equiv 1 + \frac{1}{8}\tilde{k}\tilde{u}_0^2, \quad (\text{D.1})$$

scales as \tilde{u}_0^2 , and from Eq. (C.9) we should have $\tilde{A} \approx \tilde{u}_0$. Using Eq. (C.29),

$$\frac{s}{a} \approx -\frac{v\tau_s}{a}. \quad (\text{D.2})$$

That is, the delay time in the limit of strong stimulus amplitude is τ_s , agreeing with the prediction of the 11th order perturbation.

To study natural tracking when the stimulus is weak, let us consider the steady state equations (C.21)-(C.24) when the stimulus speed differs from the natural speed by δv . Let the intrinsic network state at the natural velocity v be described by the variables \tilde{u}_0 , p_0 and p_1 . The presence of the weak stimulus causes the variables \tilde{u}_0 , p_0 and p_1 to deviate by $\delta\tilde{u}_0$, δp_0 and δp_1 respectively. Expanding Eqs. (C.21) to (C.24),

$$\begin{pmatrix} \frac{2-B}{B} & -\frac{\tilde{u}_0}{B}\sqrt{\frac{2}{7}} & 0 & 0 \\ \frac{v\tau_s}{a}\frac{2-B}{B} & 0 & \frac{v\tau_s}{a} & -\frac{\tau_s}{\tau_d} \\ \frac{2\tilde{u}_0^2}{B^2}\left(1-p_0\sqrt{\frac{2}{3}}\right) & -\left(1+\frac{\tilde{\beta}\tilde{u}_0^2}{B}\sqrt{\frac{2}{3}}\right) & -\frac{v\tau_d}{2a}p_1 & -\frac{p_1}{2} \\ \frac{2\tilde{\beta}\tilde{u}_0^2}{B^2}\left(\frac{2}{3}\right)^{3/2}p_1 & -\frac{v\tau_d}{a} & \frac{v\tau_d}{a}p_0 & -p_0 \end{pmatrix} \begin{pmatrix} \frac{\delta\tilde{u}_0}{\tilde{u}_0} \\ \delta p_0 \\ \delta p_1 \\ \frac{\tau_s\delta v}{a} \end{pmatrix} = \begin{pmatrix} -\frac{\tilde{A}}{\tilde{u}_0} \\ \frac{\tilde{A}}{\tilde{u}_0}\frac{s}{a} \\ 0 \\ 0 \end{pmatrix} \quad (\text{D.3})$$

Let the matrix in Eq. (D.3) to be M . Then,

$$\frac{\tau_s\delta v}{a} = M_{41}^{-1} \left(-\frac{\tilde{A}}{\tilde{u}_0} \right) + M_{42}^{-1} \left(-\frac{\tilde{A}}{\tilde{u}_0} \frac{s}{a} \right), \quad (\text{D.4})$$

where M_{ij}^{-1} is the elements of the inverse of the matrix M . The relevant cofactors are

$$c_{14} = \begin{vmatrix} \frac{v\tau_s}{a} \frac{2-B}{B} & 0 & \frac{v\tau_s}{a} \\ \frac{2\tilde{\beta}\tilde{u}_0^2}{B^2} \left(1 - p_0 \sqrt{\frac{2}{3}}\right) & -\left(1 + \frac{\tilde{\beta}\tilde{u}_0^2}{B} \sqrt{\frac{2}{3}}\right) & -\frac{v\tau_d}{2a} p_1 \\ \frac{2\tilde{\beta}\tilde{u}_0^2}{B^2} \left(\frac{2}{3}\right)^{\frac{3}{2}} p_1 & -\frac{v\tau_d}{a} & \frac{v\tau_d}{a} p_0 \end{vmatrix} \\ = -\frac{v\tau_s}{a} \frac{\tilde{\beta}\tilde{u}_0^2}{B^2} \left[\left(\frac{2}{3}\right)^{\frac{3}{2}} p_1 + \left(4 - 4p_0 \sqrt{\frac{2}{3}} - B\right) \frac{v\tau_d}{a} \right] \quad (\text{D.5})$$

$$c_{24} = \begin{vmatrix} \frac{2-B}{B} & -\frac{\tilde{u}_0}{B} \sqrt{\frac{2}{7}} & 0 \\ \frac{2\tilde{\beta}\tilde{u}_0^2}{B^2} \left(1 - p_0 \sqrt{\frac{2}{3}}\right) & -\left(1 + \frac{\tilde{\beta}\tilde{u}_0^2}{B} \sqrt{\frac{2}{3}}\right) & -\frac{v\tau_d}{2a} p_1 \\ \frac{2\tilde{\beta}\tilde{u}_0^2}{B^2} \left(\frac{2}{3}\right)^{\frac{3}{2}} p_1 & -\frac{v\tau_d}{a} & \frac{v\tau_d}{a} p_0 \end{vmatrix} \\ = \frac{v\tau_d}{a} \frac{\tilde{\beta}\tilde{u}_0^2}{B^2} \left\{ \frac{2\tilde{u}_0}{B} \sqrt{\frac{2}{7}} \left[\left(1 - p_0 \sqrt{\frac{2}{3}}\right) p_0 + \left(\frac{2}{3}\right)^{\frac{3}{2}} \frac{p_1^2}{2} \right] - 2 + B \right\}. \quad (\text{D.6})$$

For tracking at the natural velocity, $\tau_s \delta v/a = 0$,

$$0 = -c_{14} \left(-\frac{\tilde{A}}{\tilde{u}_0}\right) + c_{24} \left(\frac{\tilde{A}}{\tilde{u}_0} \frac{s}{a}\right). \quad (\text{D.7})$$

As a result, we have

$$\frac{s}{a} = -\frac{\tau_s}{\tau_d} \frac{\left(\frac{2}{3}\right)^{\frac{3}{2}} p_1 + \left(4 - 4p_0 \sqrt{\frac{2}{3}} - B\right) \frac{v\tau_d}{a}}{2 - B - \frac{2\tilde{u}_0}{B} \sqrt{\frac{2}{7}} \left[\left(1 - p_0 \sqrt{\frac{2}{3}}\right) p_0 + \left(\frac{2}{3}\right)^{\frac{3}{2}} \frac{p_1^2}{2} \right]}, \quad (\text{D.8})$$

where the variables p_1 , p_0 and B can be obtained from the Appendix C in the method section by putting $\tilde{A} = 0$.

Figure D.1(a) shows the natural tracking curves for various values of \tilde{k} . By measuring the slope, the delay time is $0.8\tau_s$ for $\tilde{k} = 0.3$, and decreases with increasing \tilde{k} . Figures D.1(b) and D.1(c) show that the curves of the displacement and the anticipatory time versus the stimulus speed are confluent at the natural tracking point at $\tilde{k} = 0.3$ for values of \tilde{A} one-tenth those in Fig. 5.8. Furthermore, the natural tracking points effectively lie on the curve predicted by Eq. (D.8). We remark that the coincidence of these points with the strong \tilde{A} limit in Eq. (D.2) is obviously poorer. Note, however, that the natural tracking points in the 1st order perturbation are located at $v\tau_d/a = 1.8$ and 2.9 for $\tilde{\beta} = 0.005$ and 0.01 respectively, compared with $v\tau_d/a = 1.2$ and 2.2 in Fig. 5.9. The discrepancy is probably due to the negligence of higher order distortions in the 1st order perturbation, which are expected to be significant when the stimulus speed is high.

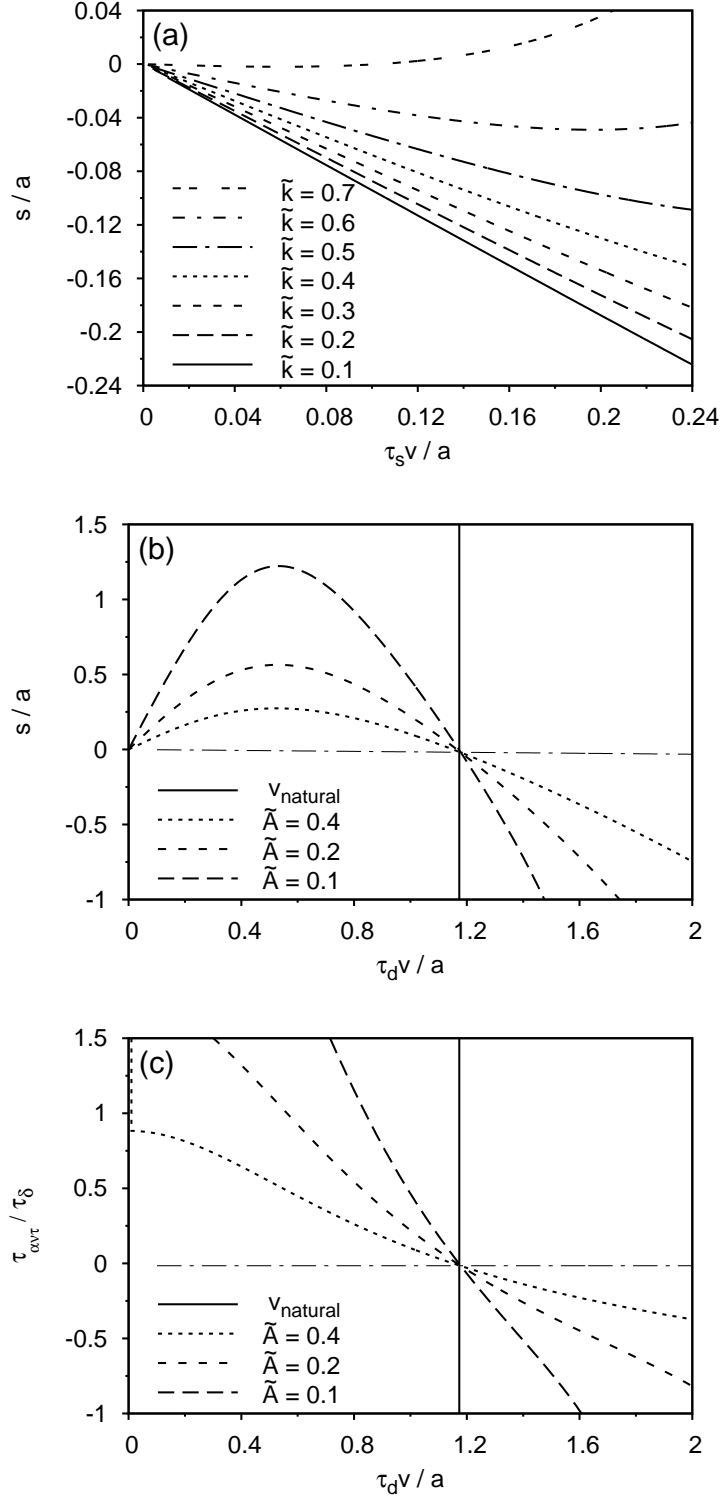


Figure D.1: (a) The natural tracking curves for various values of \tilde{k} . (b) The dependence of the displacement on the stimulus speed at $\tilde{k} = 0.3$ and $\tilde{\beta} = 0.005$. Solid line: natural speed of the system. Dot-dashed line: prediction by Eq. (D.8). (c) The dependence of the anticipatory time on the stimulus speed at $\tilde{k} = 0.3$ and $\tilde{\beta} = 0.005$. Solid line: natural speed of the system. Dot-dashed line: prediction by Eq. (D.8).

List of Publications

Journal Papers

1. C. C. Alan Fung, He Wang, Kin Lam, K. Y. Michael Wong and Si Wu, "Resolution enhancement in neural networks with dynamical synapses", *Frontiers in Computational Neuroscience* **7**, 73 (2013).
2. C. C. Alan Fung, K. Y. Michael Wong, He Wang and Si Wu, "Dynamical synapses enhance neural information processing: Gracefulness, accuracy, and mobility", *Neural Computation* **24**(5), pp. 1147–1185 (2012).
3. C. C. Alan Fung, K. Y. Michael Wong and Si Wu, "A moving bump in a continuous manifold: A comprehensive study of the tracking dynamics of continuous attractor neural networks", *Neural Computation* **22**(3) pp. 752–792 (2010).
4. C. C. Alan Fung, K. Y. Michael Wong and Si Wu, "Dynamics of neural networks with continuous attractors", *Europhysics Letters* **84**, pp. 18002 (2008).

Conference Proceedings

1. C. C. Alan Fung, K. Y. Michael Wong and Si Wu, "Dynamical Synapses Enhance Mobility, Memory and Decoding", in *Advances in Cognitive Neurodynamics (III)*, pp. 131–137 (Springer, 2013).
2. C. C. Alan Fung, K. Y. Michael Wong and Si Wu, "Delay Compensation with Dynamical Synapses", in P. Bartlett and F.C.N. Pereira and C.J.C. Burges and L. Bottou and K.Q. Weinberger, ed., *Advances in Neural Information Processing Systems* **25**, pp. 1097–1105 (2012).
3. C. C. Alan Fung, K. Y. Michael Wong, He Wang and Si Wu, "Attractor Dynamics with Synaptic Depression", in J. Lafferty and C. K. I. Williams and J. Shawe-Taylor and R.S. Zemel and A. Culotta, ed., *Advances in Neural Information Processing Systems* **23**, pp. 640–648 (2010).

4. C. C. Alan Fung, K. Y. Michael Wong and Si Wu, "Tracking dynamics of two-dimensional continuous attractor neural networks", *Journal of Physics: Conference Series* **197**, pp. 012017 (2009).
5. C. C. Alan Fung, K. Y. Michael Wong and Si Wu, "Tracking Changing Stimuli in Continuous Attractor Neural Networks", in D. Koller and D. Schuurmans and Y. Bengio and L. Bottou, ed., *Advances in Neural Information Processing Systems* **21**, pp. 481–488 (2009).

Bibliography

- [1] L. Abbott, “Lapicque’s introduction of the integrate-and-fire model neuron (1907),” *Brain Research Bulletin*, vol. 50, no. 5 - 6, pp. 303–304, 1999.
- [2] M. Tsodyks, K. Pawelzik, and H. Markram, “Neural networks with dynamic synapses,” *Neural Computation*, vol. 10, no. 4, pp. 821–835, 1998.
- [3] L. I. Zhang, H. W. Tao, C. E. Holt, W. A. Harris, and M.-m. Poo, “A critical window for cooperation and competition among developing retinotectal synapses,” *Nature*, vol. 395, pp. 37–44, 1998.
- [4] J. J. Hopfield, “Neural networks and physical systems with emergent collective computational abilities,” *Proceedings of the National Academy of Sciences of the United States of America*, vol. 79, pp. 2554–2558, Apr. 1982.
- [5] D. O. Hebb, *The Organization of Behavior: A Neuropsychological Theory*. New York: Wiley, new edition ed., June 1949.
- [6] A. Samsonovich and B. L. McNaughton, “Path integration and cognitive mapping in a continuous attractor neural network model.,” *The Journal of Neuroscience*, vol. 17, pp. 5900–5920, Aug. 1997.
- [7] R. Ben-Yishai, R. L. Bar-Or, and H. Sompolinsky, “Theory of orientation tuning in visual cortex.,” *Proceedings of the National Academy of Sciences of the United States of America*, vol. 92, pp. 3844–3848, Apr. 1995.
- [8] T. D. Albright, “Direction and orientation selectivity of neurons in visual area MT of the macaque.,” *Journal of Neurophysiology*, vol. 52, pp. 1106–1130, Dec. 1984.
- [9] J. G. Daugman, “Uncertainty relation for resolution in space, spatial frequency, and orientation optimized by two-dimensional visual cortical filters,” *Journal of the Optical Society of America A: Optics, Image Science & Vision*, vol. 2, pp. 1160–1169, July 1985.
- [10] K. Zhang, “Representation of spatial orientation by the intrinsic dynamics of the head-direction cell ensemble: a theory,” *The Journal of Neuroscience*, vol. 16, no. 6, pp. 2112–2126, 1996.
- [11] J. O’Keefe and N. Burgess, “Geometric determinants of the place fields of hippocampal neurons,” *Nature*, vol. 381, no. 6581, pp. 425–428, 1996.
- [12] C. C. A. Fung, K. Y. M. Wong, and S. Wu, “Dynamics of neural networks with continuous attractors,” *Europhysics Letters*, vol. 84, p. 18002, 2008.
- [13] C. C. A. Fung, K. Y. M. Wong, and S. Wu, “Tracking changing stimuli in continuous attractor neural networks,” in *Advances in Neural Information Processing Systems 21* (D. Koller, D. Schuurmans, Y. Bengio, and L. Bottou, eds.), pp. 481–488, 2009.
- [14] C. C. A. Fung, K. Y. M. Wong, and S. Wu, “A moving bump in a continuous manifold: A comprehensive study of the tracking dynamics of continuous attractor neural networks,” *Neural Computation*, vol. 22, pp. 752–792, Mar. 2010.
- [15] C. C. A. Fung, *Dynamics of continuous attractor neural networks*. M. Phil. Thesis. The Hong Kong University of Science and Technology, 2010.
- [16] D. J. Heeger, “Normalization of cell responses in cat striate cortex.,” *Visual Neuroscience*, vol. 9, pp. 181–197, Aug. 1992.
- [17] J. Hao, X.-d. Wang, Y. Dan, M.-m. Poo, and X.-h. Zhang, “An arithmetic rule for spatial summation of excitatory and inhibitory inputs in pyramidal neurons,” *Proceedings of the National Academy of Sciences of the United States of America*, vol. 106, no. 51, pp. 21906–21911, 2009.
- [18] A. Reyes, E. Rubel, and W. Spain, “Membrane properties underlying the firing of neurons in the avian cochlear nucleus,” *The Journal of Neuroscience*, vol. 14, no. 9, pp. 5352–5364, 1994.

- [19] A. D. Redish, A. N. Elga, and D. S. Touretzky, "A coupled attractor model of the rodent head direction system," *Network: Computation in Neural Systems*, vol. 7, no. 4, pp. 671–685, 1996.
- [20] S.-I. Amari, "Dynamics of pattern formation in lateral-inhibition type neural fields," *Biological Cybernetics*, vol. 27, pp. 77–87, 1977.
- [21] M. Abramowitz and I. A. Stegun, *Handbook of Mathematical Functions: With Formulars, Graphs, and Mathematical Tables*, vol. 55. DoverPublications.com, 1964.
- [22] C. C. A. Fung, K. Y. M. Wong, and S. Wu, "Tracking dynamics of two-dimensional continuous attractor neural networks," *Journal of Physics: Conference Series*, vol. 197, p. 012017, 2009.
- [23] C. C. A. Fung, K. Y. M. Wong, H. Wang, and S. Wu, "Attractor dynamics with synaptic depression," in *Advances in Neural Information Processing Systems 23* (J. Lafferty, C. K. I. Williams, J. Shawe-Taylor, R. Zemel, and A. Culotta, eds.), pp. 640–648, 2010.
- [24] C. C. A. Fung, K. Y. M. Wong, H. Wang, and S. Wu, "Dynamical synapses enhance neural information processing: Gracefulness, accuracy, and mobility," *Neural Computation*, vol. 24, pp. 1147–1185, May 2012.
- [25] M. V. Tsodyks and H. Markram, "The neural code between neocortical pyramidal neurons depends on neurotransmitter release probability.,," *Proceedings of the National Academy of Sciences of the United States of America*, vol. 94, no. 2, pp. 719–723, 1997.
- [26] R. King, M. Wiest, and P. Montague, "Extracellular calcium depletion as a mechanism of short-term synaptic depression.,," *Journal of Neurophysiology*, vol. 85, no. 5, pp. 1952–1959, 2001.
- [27] L. C. York and M. C. Van Rossum, "Recurrent networks with short term synaptic depression," *Journal of Computational Neuroscience*, vol. 27, no. 3, pp. 607–620, 2009.
- [28] I. Nauhaus, L. Busse, M. Carandini, and D. L. Ringach, "Stimulus contrast modulates functional connectivity in visual cortex," *Nature Neuroscience*, vol. 12, no. 1, pp. 70–76, 2008.
- [29] W. Zhang and S. Wu, "Neural information processing with feedback modulations," *Neural Computation*, vol. 24, pp. 1695–1721, July 2012.
- [30] S. Martinez-Conde, S. L. Macknik, and D. H. Hubel, "The function of bursts of spikes during visual fixation in the awake primate lateral geniculate nucleus and primary visual cortex," *Proceedings of the National Academy of Sciences of the United States of America*, vol. 99, no. 21, pp. 13920–13925, 2002.
- [31] J. S. Taube and R. U. Muller, "Comparisons of head direction cell activity in the postsubiculum and anterior thalamus of freely moving rats," *Hippocampus*, vol. 8, no. 2, pp. 87–108, 1998.
- [32] J. P. Goodridge and D. S. Touretzky, "Modeling attractor deformation in the rodent head-direction system," *Journal of Neurophysiology*, vol. 83, no. 6, pp. 3402–3410, 2000.
- [33] R. Nijhawan and S. Wu, "Compensating time delays with neural predictions: are predictions sensory or motor?," *Philosophical Transactions of the Royal Society A: Mathematical, Physical and Engineering Sciences*, vol. 367, no. 1891, pp. 1063–1078, 2009.
- [34] S. Coombes and M. Owen, "Bumps, breathers, and waves in a neural network with spike frequency adaptation," *Physical Review Letters*, vol. 94, no. 14, p. 148102, 2005.
- [35] C. C. A. Fung, H. Wang, K. Lam, K. Y. M. Wong, and S. Wu, "Resolution enhancement in neural networks with dynamical synapses," *Frontiers in Computational Neuroscience*, vol. 7, no. 73, 2013.
- [36] M. Livingstone and D. Hubel, "Segregation of form, color, movement, and depth: anatomy, physiology, and perception," *Science*, vol. 240, no. 4853, pp. 740–749, 1988.
- [37] S. Treue, K. Hol, and H.-J. Rauber, "Seeing multiple directions of motion—physiology and psychophysics," *Nature Neuroscience*, vol. 3, no. 3, pp. 270–276, 2000.
- [38] G. Mather and B. Moulden, "A simultaneous shift in apparent direction: Further evidence for a "distribution-shift" model of direction coding," *The Quarterly Journal of Experimental Psychology*, vol. 32, no. 2, pp. 325–333, 1980.

- [39] R. S. Zemel, P. Dayan, and A. Pouget, “Probabilistic interpretation of population codes,” *Neural Computation*, vol. 10, no. 2, pp. 403–430, 1998.
- [40] M. Sahani and P. Dayan, “Doubly distributional population codes: simultaneous representation of uncertainty and multiplicity,” *Neural Computation*, vol. 15, no. 10, pp. 2255–2279, 2003.
- [41] F. Raudies, E. Mingolla, and H. Neumann, “A model of motion transparency processing with local center-surround interactions and feedback,” *Neural Computation*, vol. 23, no. 11, pp. 2868–2914, 2011.
- [42] M. van Rossum, “Modelling synaptic plasticity and memory retention,” in *StatPhysHK 2013*, (Clear Water Bay, Hong Kong), The Hong Kong University of Science and Technology, July 2013.
- [43] O. J. Braddick, K. A. Wishart, and W. Curran, “Directional performance in motion transparency,” *Vision Research*, vol. 42, no. 10, pp. 1237–1248, 2002.
- [44] N. Qian, R. A. Andersen, and E. H. Adelson, “Transparent motion perception as detection of unbalanced motion signals. i. psychophysics,” *The Journal of Neuroscience*, vol. 14, no. 12, pp. 7357–7366, 1994.
- [45] H. Wang, *Neural Field Dynamics with Short-Term Synaptic Depression*. M. Phil. Thesis. The Hong Kong University of Science and Technology, 2013.
- [46] A. Loebel and M. Tsodyks, “Computation by ensemble synchronization in recurrent networks with synaptic depression,” *Journal of Computational Neuroscience*, vol. 13, no. 2, pp. 111–124, 2002.
- [47] T. Ergenoglu, T. Demiralp, Z. Bayraktaroglu, M. Ergen, H. Beydagi, and Y. Uresin, “Alpha rhythm of the eeg modulates visual detection performance in humans,” *Cognitive Brain Research*, vol. 20, no. 3, pp. 376–383, 2004.
- [48] D. Mantini, M. G. Perrucci, C. Del Gratta, G. L. Romani, and M. Corbetta, “Electrophysiological signatures of resting state networks in the human brain,” *Proceedings of the National Academy of Sciences of the United States of America*, vol. 104, no. 32, pp. 13170–13175, 2007.
- [49] E. Simonotto, M. Riani, C. Seife, M. Roberts, J. Twitty, and F. Moss, “Visual perception of stochastic resonance,” *Physical Review Letters*, vol. 78, no. 6, pp. 1186–1189, 1997.
- [50] Z. P. Kilpatrick and P. C. Bressloff, “Spatially structured oscillations in a two-dimensional excitatory neuronal network with synaptic depression,” *Journal of Computational Neuroscience*, vol. 28, no. 2, pp. 193–209, 2010.
- [51] Y. Lu, Y. Sato, and S.-I. Amari, “Traveling bumps and their collisions in a two-dimensional neural field,” *Neural Computation*, vol. 23, no. 5, pp. 1248–1260, 2011.
- [52] D. Madison and R. Nicoll, “Control of the repetitive discharge of rat ca 1 pyramidal neurones in vitro.,” *The Journal of Physiology*, vol. 354, no. 1, pp. 319–331, 1984.
- [53] Z. P. Kilpatrick, “Short term synaptic depression improves information transfer in perceptual multistability,” *Frontiers in Computational Neuroscience*, vol. 7, no. 85, 2013.
- [54] W.-J. Yuan, O. Dimigen, W. Sommer, and C. Zhou, “A model of microsaccade-related neural responses induced by short-term depression in thalamocortical synapses,” *Frontiers in Computational Neuroscience*, vol. 7, 2013.
- [55] M. Gur and D. M. Nodderly, “Visual receptive fields of neurons in primary visual cortex (v1) move in space with the eye movements of fixation,” *Vision Research*, vol. 37, no. 3, pp. 257 – 265, 1997.
- [56] Y. Katori, Y. Otsubo, M. Okada, and K. Aihara, “Stability analysis of associative memory network composed of stochastic neurons and dynamic synapses,” *Frontiers in Computational Neuroscience*, vol. 7, no. 6, 2013.